ADVANCING PERFORMANCE-BASED DESIGN AND ASSESSMENT OF EXPOSED COLUMN BASE PLATES AND WELDED COLUMN SPLICES IN STEEL MOMENT RESISTING FRAMES

Biao Song

A dissertation submitted in partial fulfillment
of the requirements for the degree of
Doctor of Philosophy
of
University College London

Department of Civil, Environmental and Geomatic Engineering
University College London

November 11, 2021

I, Biao Song, confirm that the work presented in this dissertation is my own. Where information has been derived from other sources, I confirm that this has been indicated in the work.

Abstract

Exposed column base plate (ECBP) and welded column splice (WCS) connections are critical load-carrying structural connections and are commonly used in steel moment-resisting frames (SMRFs). However, they have received relatively lower research attention than welded beam-to-column (WBC) connections, leaving several relevant aspects of their performance and their effects on the overall seismic performance of SMRFs not well investigated.

For instance, although the current design approach for ECBP connections is relatively well-established from a mechanistic standpoint, the reliability of such designed connections (i.e., the structural performance of ECBPs at the design level) is not as well understood. Therefore, some prospective refinements to the current approach may be developed to ensure acceptable and consistent failure probabilities across the various components of the ECBP connections.

In the context of WCS connections constructed before the 1994 Northridge earthquake (i.e., pre-Northridge WCSs), their potential fracture due to earthquake shaking has been recently revealed in some research studies. However, these studies did not take advantage of recent advancements in performance-based earthquake engineering (PBEE), and made several simplifying assumptions for practical purposes. Some refinements and research tools within the PBEE framework may be required to more accurately estimate the fracture demand and capacity distributions, and the associated fragility and risk of pre-Northridge WCSs.

This doctoral dissertation attempts to address these mentioned issues in a rigorous manner. Specifically, this dissertation presents the following research studies:

1. Detailed reliability analysis of ECBPs designed as per the current design method and two modified approaches (improved from the current one) for a set of 59 design scenarios subjected to combinations of gravity, wind, and seismic

loads. This also includes the Monte Carlo sampling to characterize the uncertainty sources in the load, material properties, component geometry, and demand/capacity models for various components within the connection.

2. Refined probabilistic fracture fragility assessment of pre-Northridge WCSs, accounting for the seismic demand and fracture capacity uncertainties. Optimal ground-motion intensity measures, the effect of vertical ground accelerations, and the WCS capacity uncertainties are included to improve the fracture fragility estimation.
3. Expanded fracture fragility and risk assessment of pre-Northridge WCSs in near-fault regions to address the effect of pulse-like ground motions on the distribution/increase of WCS seismic demands. Near-source probabilistic seismic hazard analysis is conducted to facilitate the fracture risk assessment.

The findings of the first study can contribute to the better scientific knowledge of reliability-based design and assessment of ECBP connections in SMRFs, whereas the last two studies can help better understand the fracture risk of WCS connections in SMRFs, and inform the planning of retrofitting strategies.

Impact Statement

This dissertation attempts to advance some aspects of performance-based design and assessment of exposed column base plate (ECBP) and welded column splice (WCS) connections in steel moment-resisting frames (SMRFs). The outcomes of this research work have a strong, direct impact on society, economy, and academic knowledge.

The outcomes from the reliability analysis of ECBPs suggest improved design approaches to overcome some limitations in the current design guide. They can serve as the impetus for the American Institute of Steel Construction (AISC) to consider the changes to the upcoming version of AISC Design Guide One for ECBP designs. Moreover, the refined simulation-based fracture fragility and risk assessment framework implemented in this dissertation offers a more accurate solution to decision-making on the planning and design of retrofitting and mitigation strategies for pre-Northridge WCSs in SMRFs located in high seismic and near-fault regions.

Concerning the economic impact, the refined framework to characterize fracture risk of pre-Northridge WCS connections developed in this dissertation can improve the financial control and reduce costs for rehabilitation or retrofitting of SMRFs.

The achievements of each individual study in this dissertation have resulted in three published journal articles. The ongoing work after this dissertation is under review, eventually resulting in three more journal publications. Additionally, the research outcomes have been communicated through participation in several international and national conferences. Finally, this dissertation is partial outcomes of some broad research projects in collaboration with Prof Amit Kanvinde and his research group at the University of California, Davis in the US. This also promotes the academic and knowledge exchange between the UK and the US.

Below is the journal publication list of the author during his PhD, including those with different research topics other than this dissertation:

1. **Song, B.**, Galasso, C., and Kanvinde, A. (2020). "Advancing fracture fragility assessment of pre-Northridge welded column splices." *Earthquake Engineering & Structural Dynamics*, 49(2), 132–154.
2. **Song, B.**, and Galasso, C. (2020). "Directivity-Induced Pulse-Like Ground Motions and Fracture Risk of Pre-Northridge Welded Column Splices." *Journal of Earthquake Engineering* (in press).
3. **Song, B.**, Galasso, C., and Garciano, L. (2020). "Wind-uplift fragility analysis of roof sheathing for cultural heritage assets in the Philippines." *International Journal of Disaster Risk Reduction*, 51, 101753.
4. **Song, B.**, Galasso, C., and Kanvinde, A. (2021). "Reliability Analysis and Design Considerations for Exposed Column Base Plate Connections Subjected to Flexure and Axial Compression." *Journal of Structural Engineering*, 147(2), 04020328.
5. Jiang, Y., **Song, B.**, Hu, J., Liang, H., and Rao, S. (2021). "Time-dependent reliability of corroded circular steel tube structures: Characterization of statistical models for material properties." *Structures*, 33, 792–803.
6. Hassan, A. S., **Song, B.**, Galasso, C., and Kanvinde, A. (2022). "Seismic Performance of Exposed Column Base Plate Connections with Ductile Anchor Rods." *Journal of Structural Engineering* (in press).

Acknowledgments

Completing this PhD is truly a long but rewarding journey. I am deeply indebted to a great many people who kindly helped and supported me during this journey.

Firstly, I would like to express my greatest appreciation to my principal advisor, Prof Carmine Galasso, for his guidance on my PhD research. Of course, my PhD would have not been possible without his continual support, both technical and moral. I always feel that I am fortunate to work with such an exemplary advisor, showing constant patience and respect to me and my research, and always encouraging me to be an independent researcher. Also, his personality and commitment to research have tremendously influenced me. Whatever success I achieve in the future, I will owe a large part to him.

I would also express my deep and sincere gratitude to my international co-advisor, Prof Amit Kanvinde (the University of California, Davis, US), from whom I have learned immensely. I am truly impressed by his brilliance, insight, and taste to conduct research. He has pushed me to broaden my knowledge and investigate the new area, not only from reliability to mechanics, but also from finite element simulations to experiments. I am extremely grateful for his patience in guiding me throughout my PhD research.

I would like to thank my subsidiary advisors at UCL, Dr Fabio Freddi, and Prof Dina D’Ayala, for their constructive comments at the early stage of my PhD.

I am grateful to all my colleagues in the Department of Civil, Environmental and Geomatic Engineering at UCL, especially all the teammates in Prof Galasso’s research group, as well as the former and current members sharing the same research office (Room GM16, Chadwick Building) with me. I am also thankful to all my friends in Zhoushan and Shanghai (China), London and Edinburgh (UK), California (US) – just

to mention a few places. Your company during the comfortable and difficult periods of my PhD journey is truly unforgettable.

This doctoral dissertation was supported by the China Scholarship Council (CSC, grant number: 201608330227) and University College London Overseas Research Scheme (UCL-ORS) through a joint research scholarship, which is greatly appreciated.

Finally, I would like to thank my beloved parents – Honggai Pu and Guocheng Song. Thank you for everything.

Biao Song
University College London
London UK
September 2021

Contents

List of Figures

List of Tables

List of Acronyms

ACI	American Concrete Institute
AISC	American Institute of Steel Construction
AISI	American Iron and Steel Institute
APT	Arbitrary-Point-in-Time
ASCE	American Society of Civil Engineers
ASD	Allowable Stress Design
ASTM	American Society for Testing and Materials
AT	Anchor rods Tension failure
ATC	Applied Technology Council
AWC	American Wood Council
BF	Bearing Failure of grout/concrete foundation
BSSC	Building Seismic Safety Council
CC	Center-Cracked
CCDF	Complementary Cumulative Distribution Function
CDF	Cumulative Distribution Function
CEN	European Committee for Standardization
CF	Connection Failure method
CFE	Continuum Finite Element
CJP	Complete Joint Penetration
Col	Collapse of the assessed structure

CoV	Coefficient of Variation
CVN	Charpy V-Notch
DG1	Design Guide One method
DG1*	refined Design Guide One method
DM	Damage Measure
DS	Damage State
DV	Decision Variable
EC	Edge-Cracked
ECBP	Exposed Column Base Plate
EDP	Engineering Demand Parameter
EDP_C	Capacity of Engineering Demand Parameter
ELF	Equivalent Lateral Force
FEFM	Finite Element Fracture Mechanics
FEM	Finite Element Modeling
FEMA	Federal Emergency Management Agency
FM	Failure Mode
FORM	First-Order Reliability Method
GM	Ground Motion
GMM	Ground Motion Model
GMPE	Ground Motion Prediction Equation
IDA	Incremental Dynamic Analysis
IDR	Inter-story Drift Ratio
IM	Intensity Measure
ISO	International Organization for Standardization
LRFD	Load and Resistance Factor Design

LTHA	Linear Time History Analysis
M	Magnitude of earthquake
MAF	Mean Annual Frequency
MATLAB	MATrix LABoratory
MCE	Maximum Considered Earthquake
MCS	Monte Carlo Sampling/Simulation
MDoF	Multi-Degree-of-Freedom
MIDR	Maximum Inter-story Drift Ratio
MPP	Most Probable Point
MRI	Mean Recurrence Interval
MSA	Multiple-Stripe Analysis
NCol	No Collapse of the assessed structure
NEHRP	National Earthquake Hazards Reduction Program
NGA-East	Next Generation Attenuation relationships for central & Eastern North America
NGA-West	Next Generation of ground-motion Attenuation models for the Western US
NGA-West2	enhancement of Next Generation Attenuation relationships for the Western US
NLTHA	Non-Linear Time History Analysis
NS-PSHA	Near-Source Probabilistic Seismic Hazard Analysis
OpenSees	Open System for earthquake engineering simulation
OpenSHA	Open-source Seismic Hazard Analysis
OSHA	Occupational Safety and Health Administration
PBEE	Performance-Based Earthquake Engineering
PC	flexural yielding of base Plate on the Compression side

PDF	Probability Density Function
PEER	Pacific Earthquake Engineering Research
PGA	Peak Ground Acceleration
PGD	Peak Ground Displacement
PGV	Peak Ground Velocity
PJP	Partial Joint Penetration
PSDA	Probabilistic Seismic Demand Analysis
PSHA	Probabilistic Seismic Hazard Analysis
PT	flexural yielding of base Plate on the Tension side
RC	Reinforced Concrete
RSA	Response Spectrum Analysis
RV	Random Variable
SAC	the Joint Venture partners of the **S**tructural Engineers Association of California, the **A**pplied Technology Council, and the **C**onsortium of Universities for Research in Earthquake Engineering
SDC	Seismic Design Category
SEAOC	Structural Engineers Association of California
SIMBAD	Selected Input Motions for displacement-Based Assessment and Design
SMRF	Steel Moment-Resisting Frame
SORM	Second-Order Reliability Method
SRSS	Square Root Sum of Squares
SS	Strike-Slip
UF	Unequal Flange
WBC	Welded Beam-to-Column
WCS	Welded Column Splice

List of Symbols

A_1	bearing area of the base plate, as per Eq. (2.22)
A_2	effective area of the concrete foundation, as per Eq. (2.22)
A_{I}, A_{II}, A_{III}	calibrated coefficients in the fracture capacity model of Eq. (4.10)
A_{rod}	unthreaded area of each anchor rod
$A_{\mathrm{rods,all}}$	total area of anchor rods on each side of the base plate
a	fitting parameter in the power-law model of Eq. (2.9) and Eq. (4.5), i.e., ln(a) is the intercept of the fitted curve for IM-EDP relationship in log-space
a_1, a_2	fitting parameters in the power-law model of Eq. (2.9) and Eq. (4.5), with respect to IM_1 and IM_2, respectively
a_c	initial crack length of the welded column splice
B	length of the base plate
B_{I}, B_{II}	calibrated coefficients in the fracture capacity model of Eq. (4.11)
b	fitting parameter in the power-law model of Eq. (2.9) and Eq. (4.5), i.e., the slope of the fitted curve for IM-EDP relationship in log-space
b_1, b_2	fitting parameters in the power-law model of Eq. (2.9) and Eq. (4.5), with respect to IM_1 and IM_2, respectively
b_f	flange width of the W-shape column section
$C_{\mathrm{I}}, \ldots, C_{\mathrm{VI}}$	calibrated coefficients in the fracture capacity model of Eq. (4.12)
C_{AT}	capacity of anchor rods against tension failure

C_{FM}	capacity of a specific failure mode (limit state) of the exposed column base plate connection
C_{PC}	capacity of base plate against flexural yielding on the compression side
C_{PT}	capacity of base plate against flexural yielding on the tension side
D	dead load
D_{I}, D_{II}, D_{III}	calibrated coefficients in the fracture capacity model of Eq. (4.13)
D_{AT}	tensile demand of anchor rods
D_{FM}	demand of a specific failure mode (limit state) of the exposed column base plate connection
D_{PC}	flexural demand of base plate on the compression side
D_{PT}	flexural demand of base plate on the tension side
DM	variable of a considered damage measure
DV	variable of a considered decision variable
d	overall depth of the W-shape column section
d_{rod}	diameter of the anchor rod
E	earthquake load
E_{modulus}	Young's modulus of steel
EDP	variable of a considered engineering demand parameter
EDP_C	variable of the capacity of a considered engineering demand parameter
EDP_i	variable of demand associated with the i-th failure mode that may individually trigger the damage state violation when developing a fragility function
$EDP_{i,C}$	variable of capacity associated with the i-th failure mode that may individually trigger the damage state violation when developing a fragility function

e	design load eccentricity (calculated from the applied axial force and moment) for the exposed column base plate connection
e_{crit}	critical value of load eccentricity for the design of exposed column base plate connection
edp	a specific value of a considered engineering demand parameter
edp_i	EDP value corresponding to the i-th ground motion obtained through cloud-based nonlinear time history analysis
edp^j	EDP value (at an investigated IM level) corresponding to the j-th ground motion obtained through IDA- or MSA-based nonlinear time history analysis
$F_{DS}(IM)$	fragility function of a considered IM
$F_R(\cdot)$	cumulative distribution function of the resistance
F_u	ultimate (tensile) strength of steel
F_u^{rod}	ultimate (tensile) strength of anchor rod steel
F_y	yield strength of steel
$F_{y,col}$	yield strength of column steel
$F_{y,pl}$	yield strength of base plate steel
f	magnitude of a compression stress block (under base plate) developed in grout/concrete foundation
f_c'	(nominal) compression strength of concrete
f_{concrete}	actual bearing strength of concrete
$f_{\mathrm{concrete}}^{\mathrm{Eq.(2.22)}}$	bearing strength of concrete obtained as per Eq. (2.22)
$f_{\mathrm{concrete}}^{\mathrm{test}}$	bearing strength of concrete obtained from the tests
f_{grout}	crushing strength of grout
$f_{M_w,R_S,Z}(m, r, z)$	joint probability density function of earthquake moment magnitude, source-to-site distance, and site-to-source geometry
$f_{\max}$	maximum bearing stress of grout/concrete foundation

$f_{\max}^{\mathrm{DG1}}$	maximum value of a compression stress block (under base plate) that can be developed in grout/concrete foundation, determined as per the Design Guide One method
$f_Q(\cdot)$	probability density function of the load effect
$f_{\mathbf{x}}(\mathbf{x})$	joint probability density function of a set of random variables
G	limit state function
$G(A\|B)$	conditional probability that A exceeds a limit for a given value of B
$G(\mathbf{X})$	performance (limit state) function of a random variable set
G_{AT}	limit state function of anchor rods tension failure
G_{FM}	limit state function of a specific failure mode of the exposed column base plate connection
G_{PC}	limit state function of base plate flexural yielding on the compression side
G_{PT}	limit state function of base plate flexural yielding on the tension side
g	edge distance between the center of anchor rods and the edge of base plate
$g(A\|B)$	occurrence frequency of A conditioned on B
$I(\mathrm{EDP}\|\mathrm{IM}_2\|\mathrm{IM}_1)$	relative sufficiency measure of a second IM to a first IM
I_{Np}	advanced ground motion intensity measure based on $S_a(T_1)$ and spectral shape parameter, as per Eq. (4.1)
$I_{Np}[(T_i)_j, \alpha = x]$	intensity measure of I_{Np} computed based on the j-th periods group and α-value of x
IM	variable of a considered intensity measure
Index$(\cdot)$	index function (turns 1 when the argument is true and 0 otherwise)
im	a specific value of a considered intensity measure
im_C^j	IM value of the j-th ground motion when the response achieves $\mathrm{EDP}_{\mathrm{C}}$ in the IDA- or MSA-based nonlinear time history analysis

im_i	IM value corresponding to the *i*-th ground motion in the cloud-based nonlinear time history analysis
$im_{1,i}$, $im_{2,i}$	IM$_1$ value, IM$_2$ value corresponding to the *i*-th ground motion in the cloud-based nonlinear time history analysis
K_{IC}	fracture toughness, critical stress intensity factor
k	number of EDPs and their corresponding failure modes that may individually trigger the damage state violation when developing a fragility function
L	live load
L_s	distance from the epicenter to the site measured along the rupture direction
$\ln\left(S_a\left(T\right)\right)$	original ground motion model for spectral intensity prediction
$\overline{\ln\left(S_a\left(T\right)\right)}$	modified ground motion model for spectral intensity prediction, accounting for the pulse-like features in ground motions
M	applied moment/flexural load
M_p	plastic moment capacity of steel column section
M_p^{plate}	plastic moment capacity of base plate; plate bending strength
$M_{pl,comp}$	actual bending moment on the compression side of base plate due to upward bearing stress of grout/concrete foundation
$M_{pl,comp}^{\text{DG1}}$	bending moment on the compression side of base plate due to upward bearing stress of grout/concrete foundation, determined as per the Design Guide One method
$M_{pl,comp}^{\text{model}}$	bending moment on the compression side of base plate due to upward bearing stress of grout/concrete foundation, determined as per a specific model
$M_{pl,comp}^{\text{true}}$	true bending moment on the compression side of base plate due to upward bearing stress of grout/concrete foundation, obtained from the continuum finite element simulations

$M_{pl,ten}$	actual bending moment on the tension side of base plate due to downward tension force in the anchor rods
$M_{pl,ten}^{\mathrm{DG1}}$	bending moment on the tension side of base plate due to downward tension force in the anchor rods, determined as per the Design Guide One method
$M_{pl,ten}^{\mathrm{model}}$	bending moment on the tension side of base plate due to downward tension force in the anchor rods, determined as per a specific model
$M_{pl,ten}^{\mathrm{true}}$	true bending moment on the tension side of base plate due to downward tension force in the anchor rods, obtained from the continuum finite element simulations
M_w	moment magnitude of the earthquake
m	a specific value of earthquake magnitude
N	width of the base plate
N_p	ratio between geometric mean of spectral accelerations (in a range of periods) to spectral acceleration at the fundamental period of a structure
N_{rec}	number of the selected ground motion records
n_{rods}	number of anchor rods in a line on one side of the base plate
O	location and design characteristics of an assessed facility
P	applied axial load
$P(\cdot)$	probability function
$P(A\|B)$	conditional probability of *A* given *B*
P_f	probability of structural/member/component failure
$p(A\|B)$	probability density of *A* given *B*
Q	maximum load effect that a structure or its member may be exposed during its expected design lifetime
Q_{ni}	nominal (characteristic) load effect of the *i*-th load

$\mathfrak{R}$	reliability, the complement of the probability of failure
R	load-carrying capacity or resistance
R^2	coefficient of determination
R_{epi}	epicentral distance
R_{JB}	Joyner-Boore distance
R_n	nominal (characteristic) strength or resistance
R_s	source-to-site distance
R_y	ratio of expected to specified minimum yield strength of steel
r	a specific value of source-to-site distance
S_a, $S_a(T_1)$	spectral acceleration at the fundamental period of a structure
$S_a(1.5T_1)$	spectral acceleration at an elongated period (assumed = $1.5T_1$) of a structure
$S_a(T_i)$	spectral acceleration at the *i*-th period of a structure
$S_{a,avg}(T_i)$	geometric mean of spectral accelerations of a periods group
$S_a(T_V)$	spectral acceleration at the fundamental vertical period of a structure
S_{DS}	design (5% damped) spectral response acceleration parameter at short periods
s	standard deviation of the natural logarithm of a considered EDP given a specific IM
s_1, s_2	standard deviations of the natural logarithm of a considered EDP given IM_1 and IM_2, respectively
T_1	fundamental (horizontal) period of a structure
T_2, T_3, T_4	second, third, fourth (horizontal) modal period of a structure
T_i	*i*-th period of a structure
$(T_i)_1$	first periods group with two considered periods $[T_1, 1.5T_1]$

$(T_i)_2$	second periods group with three considered periods [T_2, T_1, $1.5T_1$]
$(T_i)_3$	third periods group with four considered periods [T_3, T_2, T_1, $1.5T_1$]
$(T_i)_4$	fourth periods group with five considered periods [T_4, T_3, T_2, T_1, $1.5T_1$]
$(T_i)_j$	j-th periods group considered in computing I_{Np}
T_p	pulse period of the pulse-like ground motion
T_R^{rods}	tensile strength (capacity) of anchor rods
T_{rods}	actual tension force of anchor rods developed on the tension side of the base plate
$T_{\mathrm{rods}}^{\mathrm{DG1}}$	tension force of anchor rods developed on the tension side of the base plate, determined as per the Design Guide One method
$T_{\mathrm{rods}}^{\mathrm{model}}$	tension force of anchor rods developed on the tension side of the base plate, determined as per a specific model
$T_{\mathrm{rods}}^{\mathrm{true}}$	true tension force of anchor rods developed on the tension side of the base plate, obtained from the tests or continuum finite element simulations
T_V	fundamental vertical period of a structure
t	time in years
t_f	flange thickness of the W-shape column section
t_i	a specific value of pulse period
t_{lower}	flange thickness of the lower W-shape column of the welded column splice
t_p	thickness of the base plate
t_{upper}	flange thickness of the upper W-shape column of the welded column splice
t_w	web thickness of the W-shape column section
$V_{s,30}$	averaged shear wave velocity over the top 30 m
W	wind load

$\mathbf{X}$	a set of random variables
X_n	random variable, identified by the subscript *n*
Y	required bearing length of the base plate to resist flexural loading
Y^{DG1}	length of the developed compression stress block (under base plate) in grout/concrete foundation, determined as per the Design Guide One method
Z	site-to-source geometry
Z_x	plastic modulus of the column steel section
z	a specific site-to-source geometry
α	calibrated parameter in computing I_{Np} as per Eq. (4.1)
β	reliability index
β_{EDP_C}	dispersion of the logarithmic value of $\mathrm{EDP_C}$ estimate due to the epistemic uncertainty sources in the capacity estimation
$\beta_{EDP(IM)}$	aleatory (mainly record-to-record) variability around the median demand estimation
$\beta_{EDP(IM),\mathrm{tot}}$	total dispersion of median capacity and demand estimates
β_{IM}, $\beta_{IM,\mathrm{tot}}$	dispersion (lognormal standard deviation) of the fragility function
β_T	target reliability index
γ_i	load factor of the *i*-th load/load effect
Δ	displacements of the member ends
$\lvert\Delta\lambda_{Sa}(x_i)\rvert$	mean annual frequency of a specific spectral intensity value of x_i
δ	local deformation relative to the element chord between end nodes
ε	number of logarithmic standard deviations that separate the ground-motion intensity (usually represented by spectral acceleration) from the corresponding ground-motion mean prediction (through ground motion prediction equations) in the logarithmic scale

η	crack penetration ratio between the initial crack length and the lower flange thickness of the welded column splice
θ	angle between the fault strike and the path from epicenter to the site
κ	lognormal random variable with unit median and logarithmic standard deviation of $\sigma_{\ln\kappa}$, as per Eq. (2.9)
$\lambda(\cdot)$	mean annual frequency of exceedance
λ[Fracture]	mean annual frequency of fracture in the welded column splice
$\lambda_{Sa > x}$	mean annual frequency of exceeding a spectral intensity value of x
$\lambda_{Sa = x}$	mean annual frequency of a specific spectral intensity value of x
$\lambda_{Sa = x,\text{Pulse}}$	mean annual frequency of a specific spectral intensity value of x, when only pulse-like ground motions are considered
μ	mean value of a random variable
μ_G	mean value of the limit state function
μ_{IM}	median (lognormal mean) of the fragility function
μ_Q	mean value of load effects (on a structure or its member)
μ_R	mean value of resistance (of a structure or its member)
ξ	flange thickness ratio between the upper and lower W-shape columns of the welded column splice
o	zero-mean random variable representing the variability of the natural logarithm of EDP given IM, as per Eq. (4.6)
σ	standard deviation of a random variable
σ_C	fracture stress capacity of the welded column splice
$\sigma_{C,\text{estimate}}$	estimated fracture stress capacity of the welded column splice, as per Eq. (4.8)
$\sigma_{C,\text{FEM}}$	fracture stress capacity value of the welded column splice, obtained from the finite element fracture mechanics simulations

$\sigma_{C,\text{test}}$	fracture stress capacity value of the welded column splice, obtained from the tests
$\sigma_{C,\text{true}}$	true fracture stress capacity of the welded column splice
σ_D	peak tensile stress demand of the welded column splice
σ_G	standard deviation of the limit state function
σ_Q	standard deviation of load effects (on a structure or its member)
σ_R	standard deviation of resistance (of a structure or its member)
τ	fitting parameter in estimating fracture capacity of welded column splice with different initial crack configuration, as per Eq. (4.8)
v	mean annual rate of earthquake occurrence on a fault
$\Phi(\cdot)$	standard normal cumulative distribution function
$\varphi(\cdot)$	standard normal probability density function
ϕ	resistance factor (general)
ϕ_{bearing}	resistance factor for grout/concrete bearing
ϕ_{plate}	resistance factor for base plate in bending
ϕ_{rod}	resistance factor for anchor rod fracture
Ω_0	overstrength factor for seismic design

Chapter 1

Introduction

1.1 Background and motivation

Steel moment-resisting frames (SMRFs) are a commonly used seismic force-resisting system due to their ductility and architectural versatility. The 1994 M6.7 Northridge earthquake, a seismic event that led to brittle fracture of numerous welded beam-to-column (WBC) connections, had a fundamental impact on seismic research, design, and construction practice of SMRFs (Uang and Bruneau 2018). Subsequently, the vast majority of research efforts have been focused on the performance-based design and assessment of WBC connections (responding to the unexpected fracture, e.g., Alali et al. 1995; Anderson et al. 1995; Kaufman and Fisher 1995; Maison et al. 1996), leaving other important connections, their performance in SMRFs, as well as their resulting effects on the overall seismic performance and safety of SMRFs not well investigated. This dissertation focuses on two such connections that have received relatively lower research attentions, i.e., exposed column base plate (ECBP) and welded column splice (WCS) connections. Figure 1.1 illustrates their typical details and locations in a mid-rise SMRF structure.

ECBP connections are widely used to transfer forces from the superstructure to the supporting concrete foundation. They are especially important when adopted in low- to mid-rise SMRFs, where they are designed to withstand seismic loadings (i.e., to resist flexure and shear along with axial force). Also, the mechanical behavior of ECBPs plays a critical role in the overall performance and stability (e.g., collapse) of SMRFs (e.g., Picard et al. 1987). As illustrated in Figure 1.1, an ECBP connection is a complex assembly of several components (including the column, steel base plate,

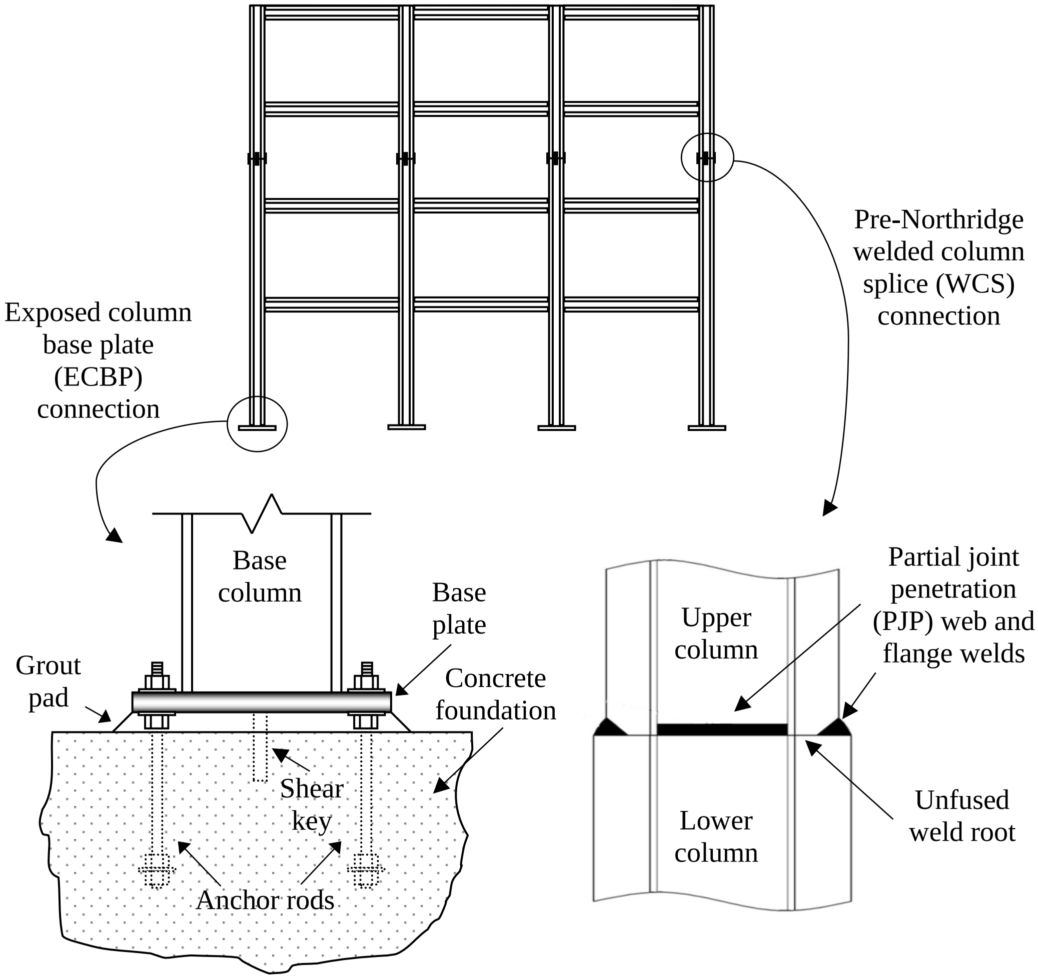

Figure 1.1: Schematic illustration of exposed column base plate (ECBP) and welded column splice (WCS) connection details and their locations in a mid-rise steel moment-resisting frame (SMRF).

anchor rods, grout pad, concrete foundation, and/or shear key). These interacting components resist the applied axial forces and moments collaboratively, i.e., through the development of bearing stresses in the grout/concrete footing (on the compression side of the connection) and the tensile forces in the anchor rods (on the tension side of the connection). In addition, shear can be resisted either through friction (between the base plate and grout/concrete foundation, if compression is sufficient), through the anchor rods, or through a shear key, if provided (Gomez et al. 2011).

The American Institute of Steel Construction's AISC Design Guide One (DG1, Fisher and Kloiber 2006) is the primary document guiding the design of ECBP connections subjected to bending moments in the presence of axial forces. From a mechanistic standpoint, it is well-established and has been accepted that it can satisfactorily estimate the internal force distribution of ECBP connections in a deterministic sense (e.g., Gomez et al. 2010; Kanvinde et al. 2013). However, from a probabilistic standpoint, the reliability of ECBPs designed as per this approach is not as well understood and received less research attention, though prior studies revealed that the DG1 method cannot provide an acceptable safety margin for some specific designed ECBPs (e.g., Aviram et al. 2010). Given the importance of ECBP connections on the system performance of SMRFs under extreme loads (i.e., they are the base connections to transfer loads from frames to foundations) and the complex nature of their load transfer mechanisms (through interactions within an assembly of components), a detailed reliability assessment to examine the safety levels of ECBPs guaranteed by the DG1 method and to further suggest some design improvements is particularly necessary.

The second connection type investigated in this dissertation is pre-Northridge WCS, which is widely used in mid- to high-rise welded SMRFs because (1) long column sections may not be readily available or may be constrained by transportation; and (2) column sizes may be transitioned over the height of SMRFs. Figure 1.1 depicts a WCS with partial joint penetration (PJP) welds (on the order of 40%–60% of the smaller connected column flange), which is a common detail for pre-Northridge WCS connections. Due to the presence of the crack-like flaw in the unfused region of the flange weld, pre-Northridge WCSs are susceptible to fracture (e.g., Bruneau and Mahin 1991; Nuttayasakul 2000). However, a large majority of WCSs were, for the most part, not checked for fracture after the Northridge earthquake, and many have not been retrofitted. This may be attributed to (1) the potential operational disruption and liability issues that may arise from such inspections; and (2) the conventional understanding that seismic demands in WCSs should be modest (especially under first-mode structural response) given their typical location in the SMRFs (i.e., near the mid-story, where the flexure is low due to double-curvature bending of columns). Nonetheless, some preliminary studies (e.g., Galasso et al. 2015; Shen et al. 2010) have indicated high seismic demands of these pre-Northridge WCSs due to, for instance, higher-mode effects.

The only study investigating the fracture fragility and risk of pre-Northridge WCS [adopting a performance-based earthquake engineering (PBEE) framework] was conducted by Galasso et al. (2015). Although this research motivated discussion on fracture risk of WCSs and awareness of their remediations in pre-Northridge steel structures (e.g., Nudel et al. 2015), it has some limitations to interpret the findings. Several simplifying (but practical) assumptions, particularly in considering the uncertainties corresponding to the seismic demands and fracture capacities of WCS were relied on to assess the WCS fracture fragility; some are discussed as follow:

- The spectral acceleration at the fundamental period of the structure $S_a(T_1)$ was adopted as the seismic intensity measure (IM). It is acknowledged that $S_a(T_1)$ can well capture the elastic response of first-mode dominated multi-degree-of-freedom (MDoF) systems for low-to-moderate fundamental periods. However, this selected IM may be questionable to accurately estimate the seismic demands of WCS in the mid- to high-rise SMRFs, which may be highly affected by higher-mode effects.
- The seismic demands of WCSs were sorely quantified from the horizontal component of ground shaking. However, it seems insufficient because such a demand (i.e., axial stress in the column flange) for WCS may be significantly amplified by the vertical ground shaking.
- A deterministic fracture capacity value [based on finite element fracture mechanics (FEFM) simulation] was employed to evaluate fracture fragility for each WCS of interest. It may be unconservative for fracture fragility evaluations because a subsequent study (Stillmaker et al. 2016) reported relatively significant uncertainty in the capacity estimation using the same FEFM approach.
- Pulse-like ground motions (GMs) were excluded from the WCS seismic demand characterization, and only far-field (non-pulse-like) earthquake records were adopted. This consideration may lower the estimated seismic demands of WCS when the SMRFs are located in the near-fault regions (which is sometimes the case), because the occurrence of pulse-like GMs near the faults has the potential to increase the axial stress in WCSs further. Thus, even though the effects of pulse-like earthquakes were mainly reported to increase global deformation demands (e.g., maximum inter-story drift ratio, MIDR) associated

with collapse fragility assessment (e.g., Champion and Liel 2012), it is still worth investigating this issue.

The issues discussed above can strongly affect the estimated pre-Northridge WCS fracture fragility and risk, compared to the findings of Galasso et al. (2015). Accurate estimation of pre-Northridge WCS fracture fragility and risk is particularly critical, because: (1) given their structural function, the fracture risk of WCS has major implications for occupant safety and thus, decisions regarding retrofit; and (2) given their location, repair/retrofit of WCS is costly and enormously disruptive to building operations. Therefore, refined performance-based assessment for pre-Northridge WCSs, utilizing some advancements recently achieved within the PBEE framework, is necessary to better understand their fracture fragility/risk and guide similar performance-based assessment exercises for SMRFs to inform, for instance, the planning and design of retrofitting strategies.

1.2 Scope and objectives

Motivated by the previous discussions, the aims of this dissertation are two-fold:

1. To advance reliability-based design of ECBP connections through re-examining the reliability of the current design approach (i.e., the structural performance of ECBPs at design level); and
2. To advance performance-based fracture fragility and risk assessment of pre-Northridge WCSs, by taking advantage of some recent state-of-the-art research tools within the PBEE methodology.

Specifically, the research objectives of the dissertation (i.e., the research topics of the following main chapters) are:

1. Perform detailed reliability analysis of the current design approach (i.e., the DG1 method) and some modified/improved alternatives for ECBPs, by using Monte Carlo sampling and a set of design scenarios from SMRFs subjected to combinations of dead, live, wind, and seismic loads. Commentary regarding the analyzed approaches and the recommending strategies that ensure consistent and acceptable reliability of designed ECBP connections are discussed;

2. Perform a refined probabilistic assessment of seismic demands and fracture capacity of pre-Northridge WCSs, through nonlinear time history analysis. Optimal ground-motion IMs, the effect of vertical GM components, and the WCS capacity uncertainties are considered to improve the fracture fragility prediction of WCSs; and
3. Investigate the fracture fragility and risk of pre-Northridge WCSs in near-fault regions, particularly addressing the effect of pulse-like GMs due to forward directivity on the distribution/increase of WCS stress demands. Fracture fragility curves are derived and combined with near-source probabilistic seismic hazard analysis to assess fracture risk.

Within this dissertation, the design and assessment of ECBP connections exclusively focus on their reliability under a combination of uniaxial bending moment and axial force (along the major axis direction of W-section columns). Shear is not considered and is assumed to be transferred separately, e.g., through a shear key (Gomez et al. 2011). Moreover, experimental observations (Gomez 2010) indicate that the presence of shear key does not cause significant changes in the moment-rotation response of ECBP connections. Biaxial bending of the base connections is also disregarded, with the implicit assumption that flexural demands in the minor-axis direction of SMRFs may be modest. However, the author recognizes that neglecting biaxial bending may be problematic, and this loading condition of ECBP connections should be explicitly examined in the near future.

When assessing the fracture fragility and risk of pre-Northridge WCSs, the primary focus of this dissertation is to characterize WCS axial stress demands from the perspective of informing the need for retrofit at a component level, and assuming the fracture of one splice as the critical event controlling retrofit decisions. As a result, fracture initiation and propagation are not simulated in the SMRF models. Nonetheless, the author recognizes the importance of the post-fracture response of WCSs and this effect on the seismic performance of SMRFs; expanded research on this aspect should be carried out to achieve more holistic development of retrofit strategies.

This dissertation is mainly the simulation-based component of some broad research projects in collaboration with researchers from the US. Therefore, it is worth noting that (1) the considered SMRFs and the adopted design methodologies in this dissertation are based on the design codes and practice in the US; and (2) this dissertation mainly presents the results of simulation-based studies, some experiments that are used to validate the analytical and numerical models in this dissertation are not reported in detail. The experiments and some parts of the numerical/analytical models used in this dissertation have been or will be published as individual research articles, the author of this dissertation has also participated (but not as the leading investigator) in the majority of those research activities.

1.3 Chapter organization

As discussed in Section 1.2, the research objectives are addressed in this dissertation's main chapters, and some have been published as stand-alone articles (as indicated at the beginning of each chapter).

Chapter 2 provides the literature review, which introduces the concepts of the probability-based limit state design approach and the performance-based earthquake engineering framework in general. These two design and assessment methodologies form the foundation of this dissertation. It then reviews the current design practice of ECBP connections and the available prior studies on the topics of reliability assessment of SMRFs considering the presence of ECBPs. This is followed by a summary of previous research that provided insight into the seismic response and/or fracture characterization of WCSs. Several research gaps relating to this dissertation are identified at the end of the chapter.

Chapter 3 first performs a detailed reliability analysis of the prevalent design approach of ECBP connections in the US (i.e., the DG1 method) by using 59 design scenarios from SMRFs subjected to combinations of dead, live, wind, and seismic loads. The analysis is conducted through Monte Carlo sampling to reflect uncertainties in the load, material properties, component geometry, as well as demand and capacity models for the various components of the connection. Results indicate that the current design approach leads to unacceptable and inconsistent failure probabilities across the various components. The possible reasons are critically discussed, and two alternative approaches are examined as prospective refinements to the current approach. For both approaches, new resistance factors are calibrated to provide consistent and acceptable safety margins across all limit states and all types of loading. Design and cost implications of these alternative approaches are also discussed.

Chapter 4 presents a refined probabilistic assessment of seismic demands and fracture capacity of pre-Northridge WCS connections in SMRFs. seismic demand assessment is performed through cloud-based nonlinear time history analysis for two case-study frames (i.e., 4- and 20-story SMRFs). Optimal ground-motion IMs for conditioning probabilistic seismic demand models in terms of global (i.e., MIDR) and local (i.e., peak tensile stress in the flange of WCSs) engineering demand parameters are first investigated from 41 spectral-shape-based IM candidates. The effects of GM vertical components on the stress demand of WCSs and their resulting fracture fragility are then estimated. This is followed by examining the effect of WCS fracture capacity uncertainties on the fracture fragility estimates. Finally, fracture fragility results for the case-study SMRFs are compared and discussed, highlighting the importance of the considered issues on the fragility estimates.

Chapter 5 mainly focuses on investigating the effect of directivity-induced pulse-like GMs on the fracture fragility and fracture risk of pre-Northridge WCSs in near-fault regions. Incremental dynamic analysis (IDA, Vamvatsikos and Cornell 2002) is performed to quantify the pulse effects on WCS stress demands explicitly. For this purpose, two case-study SMRF models are used and first subjected to a set of pulse-like GMs with varying pulse periods and then a suite of ordinary (i.e., non-pulse-like) GMs. Fracture fragility estimates for both ordinary and pulse-like earthquake records are derived from the IDA results. These are finally combined with near-source probabilistic seismic hazard analysis for a case-study scenario rupture and six representative near-fault sites to assess pre-Northridge WCS fracture risk. Findings are critically discussed.

Chapter 6 summarizes the main contributions, findings, and observations of this dissertation. Recommendations for future work are also presented.

The main chapters of this dissertation are written to be largely self-contained because they have been published as individual journal articles (indicated at the beginning of each chapter). As such, there are some repetitions in introductions and background material across chapters, to a limited extent.

Chapter 2

Literature Review

2.1 Introduction

This chapter provides a review of the existing literature related to the performance-based and probability-based design and assessment of two connection types within steel moment-resisting frames (SMRFs) – exposed column base plate (ECBPs) and welded column splices (WCSs). Section 2.2 provides an overview of the probability-based limit state approach currently adopted for codified design and assessment of new and existing structures worldwide. Available reliability techniques for load and resistance factors calibration within this approach are also summarized. Section 2.3 reviews the framework of performance-based earthquake engineering (PBEE) that is deemed an advancement to the current prescriptive approach (as discussed in Section 2.2). Several improvements (relating to this dissertation) within the PBEE framework are also discussed when necessary. Section 2.4 first introduces the current design approach for ECBPs subjected to uniaxial bending moments in the presence of axial compressions and then provides the associated reliability studies of ECBPs. Section 2.5 discusses previous research on the seismic performance of WCSs in SMRFs. Finally, Section 2.6 identifies research gaps that are addressed in the dissertation.

2.2 Probability-based limit state approach

The design of civil structures to resist demands imposed by their service requirements and by natural events (e.g., earthquake shaking and strong wind blowing) is largely guided by codes and standards. These design provisions provide a set of minimum technical requirements for safe and acceptable structural performance, a legal basis for structural engineering practice, and a bridge for technology transfer between research and practice (Ellingwood 2000). Civil structures’ failure and/or other feared damage might cause severe consequences (e.g., life and economic loss, and legal consequence) to structure occupant/user, owner, designer, and community/society. Therefore, the primary purpose of design provisions is to manage and control the performance/safety of structures to socially acceptable levels (Ellingwood 2000). Ghosn et al. (2016) has also summarized the goals that design guidelines aim to achieve: (1) assuring sufficient performance under service loads; (2) reducing localized failure probability; (3) preventing severe damage or structural collapse given natural and human-made loads and/or hazards; (4) ensuring structural durability; and (5) minimizing construction, maintenance, and other costs.

Early design codes, such as the American Institute of Steel Construction’s Manual of Steel Construction (AISC 1989), aim to fulfill design goals (as mentioned above) by applying an overall safety factor to reduce the critical failure stress down into elastic range and then, the first-order elastic structural analysis may be adequately used for the design process (Ellingwood 1994). This is the basis of the commonly called allowable stress design (ASD), and the overall safety factor is usually determined based on successful design experience and engineering judgment. Following the ASD approach, structures may be designed in a satisfactory manner concerning their serviceability and functionality. However, the degree of safety reached is usually inconsistent because ASD does not rationally consider the variability in uncertainties relating to the capacity/strength of structures or the imposed demands/effects of gravity loads and environmental hazards (Ghosn et al. 2016).

On the other hand, probability-based methods can provide a framework to assess and quantify structural safety and performance in a rational manner by explicitly considering a wide range of uncertainty sources (Ellingwood 2000). In general, uncertainty can be classified into two categories: aleatory, related to luck or chance; and epistemic, associated with human knowledge (Ayyub and McCuen 2003). Aleatory uncertainty arises from the natural randomness or inherent variability of a parameter. Epistemic uncertainty means imperfect knowledge describing and predicting physical phenomenon, property, or characteristic that affects structural performance or safety. The former type of uncertainty cannot be reduced, but the latter one can be reduced through improved knowledge, additional data, further testing, and advanced modeling (Der Kiureghian and Ditlevsen 2009).

For building design and construction practice, uncertainties are unavoidable (Ang and Tang 2006), and are at the root of the structural safety problems (Ellingwood 2000). They come from numerous sources – both the demands acting on a structural system (e.g., design loads and load factors) and from the capacity of the system (e.g., material properties) to withstand these demands (Bulleit 2008). Risk, which is defined as the probability or likelihood of an unfavorable event/hazard and its consequence in human and/or economic terms, is the natural consequence responding to uncertainties (Ellingwood 1994). In contrast to many engineering fields that are product-oriented (e.g., aerospace, and automotive engineering), civil or structural engineering is professional service-oriented, the constructed facilities are more likely one-of-a-kind and are not mass-produced. As a result, it is not easy to collect structural performance data under repeatable circumstances, leaving the prediction of structural demands and capacities highly variable (Ellingwood 2000). These structural design and assessment difficulties may be addressed by employing probabilistic modeling and statistical analysis, i.e., structural reliability theory. The implementation of reliability methods to design new structures and assess the safety/performance of existing structural systems is widely accepted in civil engineering fields. Therefore, probability-based limit state design codes, usually named load and resistance factor design (LRFD) methods, have become the mainstream of current code development (Ghosn et al. 2016).

2.2.1 Load and resistance factor design

Reliability of structure or its members is the ability of a structure/structural component to satisfy its design purposes for a specified design life (Nowak and Collins 2012). It can be usually expressed in terms of limit state function G:

$$G = R - Q \tag{2.1}$$

where, R is the load-carrying capacity or resistance, and Q is the maximum load effect that the structure or its member may be exposed to during its expected design lifetime. On the conceptual basis for structural reliability theory, both parameters R and Q of Eq. (2.1) are modeled by random variables (RVs, Ellingwood 2008). As an application of the total probability theorem, the probability of structural/member failure (P_f), or limit state exceedance (defined as $G \leq 0$), can be determined by a convolution integral (Ghosn et al. 2016):

$$P_f = \Pr(G \leq 0) = \int_0^{\infty} F_R(q)\, f_Q(q)\, dq = 1 - \Re \tag{2.2}$$

where, $F_R(\cdot)$ is cumulative distribution function (CDF) of the resistance R, $f_Q(\cdot)$ is probability density function (PDF) of the load effect Q, and $\Re$ is reliability (i.e., the complement of the probability of failure, P_f). To evaluate the safety of a (new or existing) structure, a reliability-based design guideline should explicitly follow Eq. (2.2) to calculate P_f and assure that P_f does not exceed an acceptable upper-bound value of failure probability. However, this explicit approach seems impractical for modern design codes (i.e., a prescriptive format of design rules) – (1) it requires solid knowledge of the probabilistic nature for R and Q, which are different for various limit states of structural components; and (2) it causes the problem of how to address the numerical integration with respect to the typical iterative design context (Ellingwood 2000).

In the late 1960s, research efforts were begun to transform Eq. (2.2) into a form more practical for design code development (e.g., Ang and Cornell 1974; Cornell 1969). In 1969, the AISC and the American Iron and Steel Institute (AISI) commenced a research project to develop a practical code for steel structural design considering reliability theory to treat uncertainties in R and Q of Eq. (2.1). This design approach is referred to as the LRFD method. The technical basis for LRFD was described in a collection of papers published in 1978 (Bjorhovde et al. 1978; Cooper et al. 1978; Fisher et al. 1978; Galambos and Ravindra 1978; Hansell et al. 1978; Ravindra et al. 1978; Ravindra and Galambos 1978; Yura et al. 1978). Although the LRFD method is considered semi-probabilistic, it represents the first attempt to implement a rational probabilistic approach to manage uncertainties in the context of a modern limit state design code (Ellingwood 2000). Derived from Eq. (2.1), LRFD applies separate factors on the nominal values of resistance and corresponding load effects (to reflect uncertainties in these parameters and to balance the reliability and cost of structural design) through a deterministic equation (Ghosn et al. 2016):

$$\phi R_n \geq \sum \gamma_i Q_{ni} \tag{2.3}$$

where, R_n is the nominal (characteristic) strength or resistance, ϕ is resistance factor, Q_{ni} is the nominal (characteristic) load effect of load i, and γ_i is the associated load factor. For a structural component or section-level design, the left-hand side of Eq. (2.3) is denoted the design strength and is the purview of specific material codes [e.g., AISC 360-16 (AISC 2016a) for structural steel buildings in the US]; and the right-hand side can be determined from the set of load combinations prescribed by load-design code [e.g., American Society of Civil Engineers' ASCE 7-16 (ASCE 2016) in the US]. Load and resistance factors are calibrated so that the designed structural components and connections can provide consistent levels of reliability for all the considered limit states by meeting target reliability indices, β_T (Ellingwood and Galambos 1982). The first specification in LRFD format for steel structural design in the US, including the factors suggested by Ellingwood et al. (1980), was introduced in 1986 (AISC 1986) and has been followed by several other national design codes [e.g., the American Concrete Institute's ACI 318-19 (ACI 2019) for reinforced concrete design, and the American Wood Council's National Design Specification (AWC 2018) for wood construction]. Similar probability-based approaches using load and resistance (or partial material) factors have been adopted worldwide for structural design standards [e.g., Eurocode EN 1990 (European Committee for Standardization, CEN 2002) in Europe] and for guidelines to assess existing structures [e.g., International Organization for Standardization's ISO 13822 (ISO 2010)].

2.2.2 Statistical modeling of load effects and resistance

As discussed previously, the reliability of structures, represented by limit state function G of Eq. (2.1), is necessarily expressed in probabilistic terms (i.e., RVs) as their actual values cannot be determined with certainty (Galambos 1981). According to measured laboratory and/or field data, various probabilistic models and statistical methods are available to simulate the appropriate probability distributions of RVs (Ang and Tang 2006). These statistical models provide a rational framework for consistently processing observed data and extrapolating beyond the observation range (Ellingwood 2000). As illustrated in Figure 2.1, the performance of structural components can be commonly represented by simulating the tail ends of PDFs of

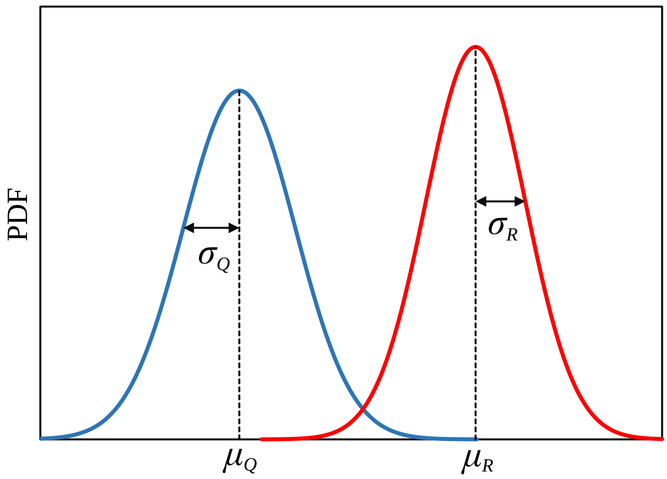

Figure 2.1: Probabilistic description of load effect Q and resistance R for reliability assessment (for simplicity, normal distribution is used for both PDFs of R and Q).

resistance (R) and load effect (Q). Following this, Thoft-Christensen and Baker (1982) suggested using the physical characteristics of each specific RV to select a probability distribution.

Generally speaking, the dead (permanent) load effect is usually modeled by a normal distribution (Ellingwood et al. 1980). The largest extreme values of live and other transient load effects that imposed on a structure over a successive reference period are typically modeled by lognormal or extreme value distributions (Ghosn et al. 2016) – Gumbel distribution (Type-I extreme value distribution) is commonly used to model the maximum values of underlying independent identically distributed load effects (e.g., live and wind loads) that are featured with an exponentially decaying tail (Ang and Tang 2006). The largest seismic load effects may be modeled by Fréchet distribution (Type-II extreme value distribution) that have a polynomial decreasing tail (Ellingwood et al. 1980) or lognormal distribution that converges to Type-II asymptotic form in the direction of the extreme values (Galambos 1978). To model the frequent (arbitrary-point-in-time, APT) values of time-varying load effects sampled at some time instant, specific distributions are considered, such as Gamma distribution for APT values of live load effects (Philpot and Rosowsky 1992). The statistical properties of individual load effect, represented by the bias coefficient (i.e., the ratio between mean to nominal design values of each RV) and the coefficient of variation (CoV, i.e., the ratio between the standard deviation of each RV to its mean value), are comprehensively documented in Ellingwood et al. (1980). Due to the scarcity of data on the extreme environmental events/hazards (e.g., wind, snow, earthquake, and flood), statistics were used to analyze them for design purposes. Early studies by Davenport (1960) and Cornell (1968), for wind and seismic hazards, respectively, began using return period (in years) to determine the extreme natural hazards. This approach is then widely adopted for LRFD design using Eq. (2.3) [e.g., ASCE 7-16 (ASCE 2016)]. The return period, also known as mean recurrence interval (MRI), is the inverse of the mean occurrence rate of the loading event for a Poisson process. The Poisson model assumption is strictly valid if (1) the occurrences of loading events are statistically independent; and (2) the probability of simultaneous occurrences is negligible. The Poisson model may be used for simplicity if specific data of natural events is limited or unavailable (Ghosn et al. 2016).

The resistance R of Eq. (2.1) is usually expressed by a mechanical model or an analytical equation that includes a set of underlying parameters (RVs) associated with the geometry and material properties of the designed member. Thoft-Christensen and Baker (1982) recommend using normal or lognormal distributions to model R if the resistance is modeled as the sum or product of independent RVs. However, given the complexity of determining R from various uncertainty sources incorporated in its definition, it may be challenging to assume a proper statistical distribution for R directly before the reliability assessment. Advanced structural reliability methods (which are briefly reviewed subsequently), such as random sampling methods that approximately aggregate R, may become a good choice. To achieve this, the statistical properties of each RV of R, which may be convenient and/or cost-less to characterize, should be provided. Several previous studies have taken efforts to identify these distributions for design code calibration. Some representative studies are reviewed as follow: (1) Ellingwood et al. (1980) summarized the resistance statistics (including material properties, geometry and dimension variation and the overall resistance modeling of typical failure modes) for reinforced and prestressed concrete, metal, masonry structures and their members; (2) Schmidt and Bartlett (2002) determined geometric and material statistics of rolled wide flange, welded wide flange and hollow shaped steel structural sections that are used in American and Canadian markets; (3) Melcher et al. (2004) statistically evaluated the material and geometrical characteristics of European hot-rolled steel I-beam profiles with different strength grades; (4) Liu et al. (2007) analyzed key statistics of American steel (of various shapes and material specifications) in terms of the ratios between actual and specified minimum yield or tensile strength; (5) Nowak and Szerszen (2003) obtained statistical parameters of compressive strength for ordinary, high-strength and lightweight concretes and listed fabrication factor (i.e., geometry-related RV) as well as professional factor (model-related RV). Additionally, mechanical models and analytical formulations also cause errors in estimating R, which is known as model uncertainties. In particular, this type of uncertainty is distinct for the analytical model developed for various limit states and failure modes, and may be statistically determined by comparing the resistance obtained in experimental or numerical tests with the corresponding values obtained from analytical equations or models.

2.2.3 Structural reliability methods for code calibration

Until the late 1960s, the classical structural reliability theory introduced was mainly theoretical and relatively simple in nature (Freudenthal et al. 1966). The most classic reliability approaches can be found in structural reliability textbooks (e.g., Ang and Tang 2006; Melchers and Beck 2018; Nowak and Collins 2012; Thoft-Christensen and Baker 1982). As discussed previously, the fundamental problem in structural reliability theory is to compute the integral of Eq. (2.2), which may be re-written as a multi-fold probability integral:

$$P_f = \Pr\left(G\left(\mathbf{X}\right) \leq 0\right) = \int_{G(x)\leq 0} f_{\mathbf{x}}\left(\mathbf{x}\right) d\mathbf{x} \tag{2.4}$$

where, $\mathbf{X} = (X_1, X_2, \ldots, X_n)$ is a set of RVs representing uncertain structural quantities (as discussed in Section 2.2.2), $f_{\mathbf{x}}(\mathbf{x})$ is the joint PDF of $\mathbf{X}$, and $G(\mathbf{X})$ is the performance function (or called limit state function). In the modern probability-based limit state design and assessment, the input variable $\mathbf{X}$ usually involves many basic independent or correlated RVs, which leads to difficulties estimating P_f strictly by classical methods. Instead, several numerical algorithms and simulation techniques have been subsequently developed for practical approximation (Madsen et al. 1986).

To avoid conceptual and practical issues (e.g., computational problems) with the use of Eq. (2.2), the notion of reliability index, β (Cornell 1969; Hasofer and Lind 1974) is introduced as an alternative measure (to P_f) of structural reliability. In its initial implementation, β is the reciprocal of the CoV of the limit state function G of Eq. (2.1), if R and Q are uncorrelated:

$$\beta = \frac{\mu_G}{\sigma_G} = \frac{\mu_R - \mu_Q}{\sqrt{\sigma_R^2 + \sigma_Q^2}} \tag{2.5}$$

where, μ and σ are the mean and standard deviation of an RV, and the subscriptions (G, R, and Q) have the same meanings as those in Eq. (2.1). Parameters of μ_R, σ_R, μ_Q, and σ_Q are given in Figure 2.1, and β is related to the overlapping area in the same figure. Moreover, suppose G follows a normal distribution (or R and Q are normally distributed RVs). In that case, the relationship between the probability of failure P_f and reliability index β can be expressed as:

$$P_f = \Phi(-\beta) \Leftrightarrow \beta = -\Phi^{-1}(P_f) \tag{2.6}$$

where, $\Phi(\cdot)$ is the standard normal CDF. Even though Eq. (2.6) holds exactly when G is normally distributed, it is commonly used to determine the approximation of reliability index for all types of distributions (Ghosn et al. 2016).

One early technique to estimate β is referred to as the first-order reliability method (FORM). As illustrated in Figure 2.2, FORM is an analytical approximation in which β is interpreted as the minimum distance between the origin and the limit state surface in standardized normal space (i.e., U-space). In general, three steps are required for FORM to make the integration of Eq. (2.4) easy to be computed: (1) To simplify the integrand $f_{\mathbf{X}}(\mathbf{x})$ by transforming the RVs (i.e., **X)** from their original random space (X-space) into U-space, using Rosenblatt transformation (Hohenbichler and Rackwitz 1981). Following this, the contours (i.e., projections of the surface of $f_{\mathbf{X}}(\mathbf{x})$ on X-space, and all the points on the contours share the same values of $f_{\mathbf{X}}(\mathbf{x})$ or the same probability density, such as the dashed circles in Figure 2.2) become more regular and symmetric; and (2) To approximate the integration boundary $G = 0$ through using the first-order Taylor expansion (linearization); (3) To search the most probable point (MPP, or named design point, i.e., the point that has the largest probability density on the performance boundary $G = 0$) in U-space by using numerical algorithms

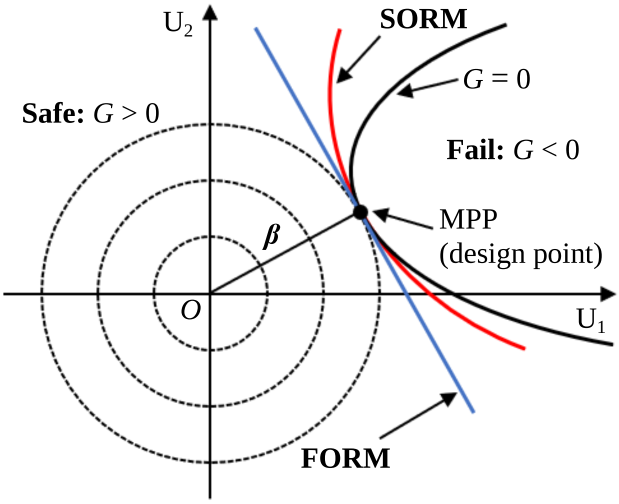

Figure 2.2: Comparison of first-order reliability method (FORM) and second-order reliability method (SORM) in standardized normal space (U-space).

(Hasofer and Lind 1974; Shinozuka 1983). Following these steps, the standardization of the RVs is done to achieve the invariance of the performance function $G(\mathbf{X})$ and the reliability index β can be calculated. Moreover, the second-order reliability method (SORM) has also been established as an attempt to improve the accuracy of FORM, in particular, when the performance function $G(\mathbf{X})$ is highly nonlinear (Fiessler et al. 1979; Tichý 1994). As its name implies, SORM approximates the performance function in U-space at the MPP using second-order Taylor expansion (Figure 2.2). The main limitation of SORM is efficient issues if it is evaluated numerically. As a result, FORM is regularly applied to develop LRFD approaches (Ghosn et al. 2016).

Due to the advances of electronic computing techniques, variations in the sampling methods are now commonly used for structural reliability assessment. The most popular approach is the plain Monte Carlo simulation (MCS, Melchers and Beck 2018). The MCS method relies on the fact that P_f can be computed by statistical averaging (Au and Wang 2014). In particular, realizations of $\mathbf{X}$ are randomly sampled from their probability distributions (as discussed previously in Section 2.2.2), and the limit state function $G(\mathbf{X})$ corresponding to each simulation can be then calculated deterministically. Finally, the probability of failure (P_f) may be evaluated through a one-by-one check of $G(\mathbf{X})$:

$$P_f = \frac{\text{Number of } G\left(\mathbf{X}\right) \leq 0}{\text{Total Number of Samples}} \tag{2.7}$$

and the corresponding reliability index β can be then determined through Eq. (2.6). When the evaluated P_f is small, MCS suffers from its inefficiency because a large sample size is required to achieve a stable estimate (Nowak and Collins 2012). This may be computationally demanding if the limit state function is complicated and/or the estimated structural reliability is high. As a consequence, several modifications have been developed to improve the sampling efficiency and reduce the computational cost, such as importance sampling (Bucher 1988; Shinozuka 1983), subset simulation (Au and Beck 2001), and response surface method (Bucher and Bourgund 1990; Faravelli 1989).

Another family of methods, known as surrogate models (Forrester et al. 2008), has been recently developed for structural reliability assessment. However, FORM and MCS are still the prevalent reliability methods accepted for developing LRFD-based design codes and standards (Ghosn et al. 2016).

As discussed after Eq. (2.3), the load and resistance factors (γ_i and ϕ) are calibrated in the way that the reliability index (β) of a designed structural component or member should achieve its acceptable or target values, i.e., target reliability index β_T (Ellingwood and Galambos 1982). In most cases, appropriate β_T values are often set based on experience with the performance of existing structures, the consequences of component failure on system performance (e.g., collapse), and the cost of construction (Ghosn and Moses 1986; Victorsson 2011). Ghosn et al. (2016) has comprehensively reviewed and summarized the target reliability levels adopted for evaluating strength limit states for various types of structural members and materials by several countries worldwide.

The load factors (γ_i) and load combinations have been designated in many design codes [e.g., ASCE 7-16 (ASCE 2016)], to represent the possible simultaneous occurrences of different loads and natural hazards. The calibration procedures and results are documented in Ellingwood et al. (1982, 1980) and Galambos et al. (1982). The load combinations follow the principle of “principal action – companion action”, and it is approximately applied based on the assumption that the maximum combined load effect during a design life may be achieved when one time-varying load is at its maximum value while the remaining transient loads are at their APT (frequent) values

(Turkstra and Madsen 1980). On the other hand, the calibration of resistance factor (ϕ) accounts for the following factors: (1) uncertainty of material properties; (2) uncertainty of member dimensions; (3) uncertainty due to model error; (4) failure modes; and (5) Importance of member (Ellingwood et al. 1980). The calibration process is also well established in the literature (e.g., Cornell 1969; Ghosn et al. 2016). It is done by (1) extracting the target reliability index of a representative set of existing structural designs that have adequate safety margin (at reasonable cost) to determine ϕ-factor; or (2) performing reliability analyses of a representative set of newly designed components based on a range of trail ϕ-factors, and finally selecting the proper value of ϕ in a way that the reliability index achieved from these new designs meets the required target level.

2.3 Performance-based earthquake engineering

After the 1994 Northridge and 1995 Kobe earthquakes in the US and Japan, the structural and earthquake engineering community realized that physical and economic damages of structures could surpass expectations by a significant amount, even though these structures were designed following available seismic codes based on traditional earthquake design philosophy. This realization, combined with the improved knowledge about earthquake occurrences, ground motions (GMs), and structural response characteristics, led to the development of PBEE concepts (Krawinkler 1999). As indicated by Ellingwood (2008), the key advantage of the PBEE framework is that it can analyze the actual performance and condition of a structure instead of merely indicating code conformance, providing the ability to design structures beyond the performance levels required by prescriptive codes (e.g., LRFD-based codes, discussed previously). Therefore, PBEE may replace LRFD as the framework to design and assess the performance of new and existing structures for seismic adequacy (Porter 2003).

The first generation of PBEE methodology in the US includes the Structural Engineers Association of California’s Vision 2000 report (SEAOC 1995), the Applied Technology Council’s ATC-32 (ATC 1996a), ATC-40 (ATC 1996b), the Federal Emergency Management Agency’s FEMA-273 [BSSC (Building Seismic Safety Council) 1997], and FEMA-356 (ASCE 2000). These documents made an important step towards realizing PBEE and defined a design and assessment framework to assure the desired system performances given various levels of seismic hazard (Günay and Mosalam 2013). Although slight differences were found from these documents, they generally expressed design criteria using a similar framework (Porter 2003). In particular, performance levels can be described by fully operational, operational, life safety, and near collapse. In contrast, hazard levels can be classified by frequent (43-year return period), occasional (72-year), rare (475-year), and very rare (949-year) events (SEAOC 1995). Moreover, the acceptable structural response indices (e.g., inter-story drifts, element deformations, and forces) corresponding to each performance level are specified for different structural/non-structural elements for various (linear/nonlinear, static/dynamic) analyses. Without minimizing the achievements of the first-generation PBEE procedures, several shortcomings were identified by researchers (e.g., Deierlein et al. 2003; Moehle and Deierlein 2004; Moehle 2003): (1) engineering demands are usually obtained from simplified analyses (e.g., linear static analysis techniques); even if nonlinear dynamic analyses are used, the performance evaluation is largely deterministic; (2) the defined relationships between calculated demands and component performance criteria are based somewhat inconsistently on relations measured in laboratory tests, calculated by analytical models, or assumed based on engineering judgments and/or current building codes; and (3) the component performance evaluation is not well tied to the global system performance.

Responding to the shortcomings widely recognized from the first-generation methodology, a more robust PBEE framework was then developed in the Pacific Earthquake Engineering Research (PEER) Center in the US. Unlike earlier PBEE, PEER PBEE methodology explicitly expresses system performance by measures such as monetary losses, downtime (period corresponding to loss of function), and casualties and rigorously assesses the structural performance in a probabilistic manner (Günay and Mosalam 2013). Several publications have summarized the PEER PBEE framework (e.g., Cornell and Krawinkler 2000; Deierlein et al. 2003; Krawinkler 1999, 2002; Krawinkler and Miranda 2004; Moehle and Deierlein 2004; Moehle 2003; Porter 2003) and various benchmark studies have been conducted (e.g., Comerio 2005; Goulet et al. 2007; Krawinkler 2005; Kunnath et al. 2006).

Referring to Figure 2.3, the PEER PBEE framework consists of four key analyses in a linear progression: hazard analysis, structural analysis, damage analysis, and loss analysis. The outcome of each analysis is characterized by the following variables: intensity measure (IM), engineering demand parameter (EDP), damage measure (DM), and decision variable (DV). Considering the inherent uncertainties involved in each analysis, these four variables are mathematically expressed in a probabilistic sense in terms of conditional probabilities, $g(A|B)$ and $p(A|B)$. The expression $g(A|B)$ refers to the occurrence frequency of A conditioned on B and $p(A|B)$ is the probability density of A given B. According to Figure 2.3, it is assumed that each analysis step can be treated as a discrete Markov process, where the conditional probabilities between parameters are independent (Moehle and Deierlein 2004). The PEER PBEE methodology combines these probabilities of the four generalized variables (i.e., IM, EDP, DM, and DV) logically and consistently using the total probability theorem, and it can be expressed by the well-known triple integral:

$$\lambda\left(DV\right)=\iiint G\left(DV\left|DM\right.\right)\left|dG\left(DM\left|EDP\right.\right)\right|\left|dG\left(EDP\left|IM\right.\right)\right|\left|d\lambda\left(IM\right)\right| \tag{2.8}$$

where, $\lambda(\cdot)$ is the mean annual frequency (MAF) of exceedance, $d\lambda(IM)$ is the differential of the MAF of exceeding the IM (which for small values is approximately equal to the annual probability of exceedance of IM), $G(A|B)$ is the complementary CDF (CCDF) or the conditional probability that A exceeds a specific limit for a given value of B, and $dG(A|B)$ is the derivative with respect to A of $G(A|B)$.

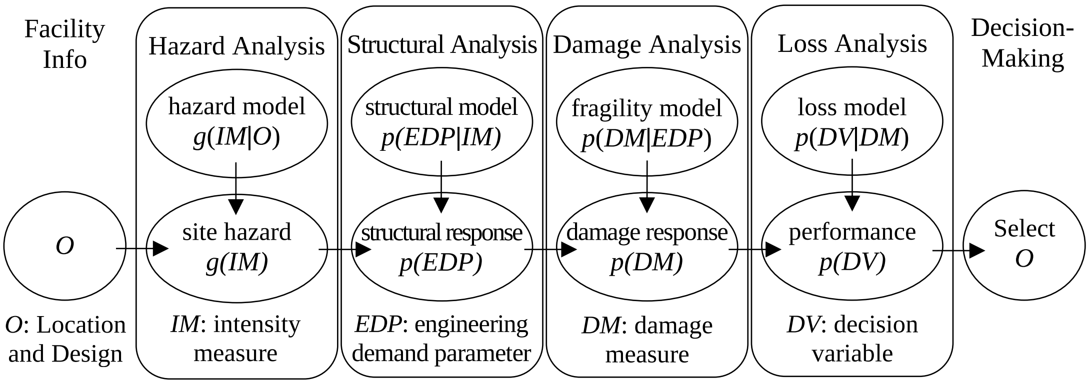

Figure 2.3: Performance-based earthquake engineering (PBEE) framework (adapted from Porter 2003 and Moehle and Deierlein 2004).

The PEER PBEE framework can be used directly for structural performance assessment or can be used as the basis for developing simplified performance metrics and criteria for performance-based design (Moehle and Deierlein 2004). Each analysis of the framework (as illustrated in Figure 2.3) is reviewed in the following subsections, except for the loss analysis as this is out of the scope of this dissertation. Moreover, several improvements of the PBEE framework, relevant to the aim of this dissertation, are also discussed.

2.3.1 Hazard analysis

Hazard analysis is conducted to describe the seismic hazard of the assessed facility, given its location and design characteristics (denoted by O in Figure 2.3), in a probabilistic manner, through a probabilistic seismic hazard analysis (PSHA) framework (for far-field ordinary GMs, e.g., McGuire 2008) or a near-source PSHA (NS-PSHA) framework (for near-fault pulse-like GMs, e.g., Chioccarelli and Iervolino 2010, 2013; Iervolino and Cornell 2008; Shahi and Baker 2011; Tothong et al. 2007). In particular, seismic environment (e.g., nearby faults, their magnitude-recurrence rates, fault mechanism, source-to-site distance, and site conditions) and structural features (e.g., fundamental period of vibration and damping ratio of the structure), and attenuation relationships (also called ground motion prediction equations, GMPEs, or ground motion models, GMMs, e.g., Power et al. 2008) are considered to determine a hazard curve, which is plotted as the variation of a selected IM (GM parameter) versus the MAF of exceedance of this IM, $\lambda(IM)$ (Bommer and Abrahamson 2006). Applications and software, such as OpenSHA (*Open-source Seismic Hazard Analysis*, Field et al. 2003) and OpenQuake (Pagani et al. 2014; Silva et al. 2014a) may be used directly for hazard analysis.

Ground-motion IM defines the salient characteristics of the earthquake hazard that affect structural response (Deierlein et al. 2003). Conventional scalar IMs, including peak ground acceleration (PGA), peak ground velocity (PGV), and spectral acceleration at the fundamental period (T_1) of a structure [$S_a(T_1)$, Shome et al. 1998], are commonly used because most of the available GMPEs used in PSHA are developed for these IMs (Günay and Mosalam 2013). Among the various GM characteristics, epsilon (ε), defined as the number of logarithmic standard deviations that separate the GM intensity (usually represented by spectral acceleration) from the corresponding GM mean prediction (through GMPEs) in the logarithmic scale, has been observed to significantly influence the structural response from its mean value at a given IM level (Baker and Cornell 2005). In fact, ε has often been considered as a proxy for spectral shape, and a better spectral-based IM should account for the effect of spectral shape in terms of higher modes and significant nonlinearity of structures (Baker and Cornell 2008b). Therefore, spectral ordinates at higher-mode periods (to consider structural higher-mode effects) or at elongated periods (to account for inelastic structural response) and their averaged (geometric mean) quantities (e.g., Baker and Cornell 2006; Eads et al. 2015; Kazantzi and Vamvatsikos 2015) are used as advanced IMs.

Moreover, several special IMs have been proposed and investigated to improve their correlations with earthquake-induced structural response/damage. These include (1) inelastic spectral displacement or acceleration (e.g., Tothong and Cornell 2006; Tothong and Luco 2007); (2) fractional-order IMs (e.g., Du et al. 2019; Shafieezadeh et al. 2012); (3) energy-related, integral-based IMs (e.g., Bradley et al. 2009; Travasarou et al. 2003); (4) non-spectral based IMs (e.g., Kiani et al. 2019); and (5) vector representations of aforementioned and other IM quantities (e.g., Baker and Cornell 2005; Kohrangi et al. 2016a; Vamvatsikos and Cornell 2005). The key criteria for selecting optimal IM that can predict seismic demand with less uncertainty were also established (Padgett et al. 2008): (1) efficiency (to minimize the record-to-record variability, e.g., Giovenale et al. 2004); (2) sufficiency (to reduce the effect of other seismological parameters on seismic response prediction, e.g., Luco and Cornell 2007); and (3) hazard computability (to conveniently determine IM through existing attenuation curves and hazard curves or maps).

In addition to determining optimal IMs, hazard analysis also involves characterizing appropriate GM input for time history analysis. An adequate number of GMs should be selected to provide meaningful statistical data in structural analysis (the next step of the PBEE framework). To be consistent with the PSHA, GM selection should be compatible with the magnitude-distance combination which dominates the seismic hazard at each given IM level (Shome et al. 1998) and be consistent with the site class of the assessed structure (Günay and Mosalam 2013). Instead of selecting

GMs for each IM level, selecting and scaling a fixed suite of GMs for various IM levels (e.g., Vamvatsikos and Cornell 2002) is also widely used for practical purposes. However, large scaling may result in unrealistic GMs and then affect the accuracy of structural analysis (Bommer and Acevedo 2004; Luco and Bazzurro 2007). Therefore, unscaled GMs may be beneficial to use whenever possible. This usually requires selecting many GMs in terms of the representative set because different GM subsets may be needed for each IM level (e.g., Jalayer et al. 2017). Various strong-motion databases, such as the SIMBAD (*Selected Input Motions for displacement-Based Assessment and Design*) database (Smerzini et al. 2014), the NGA-West (*Next Generation of ground-motion Attenuation models for Western US*) database (Chiou et al. 2008), the enhanced NGA-West2 database (Ancheta et al. 2014), and the NGA-East (*Next Generation Attenuation relationships for central & Eastern North America*) database (Goulet et al. 2021), are publicly available for GM selections.

2.3.2 Structural analysis and probabilistic seismic demand analysis

Structural analysis is conducted to estimate the structural response to different levels and features of seismic hazard in a probabilistic manner. The uncertainties from both earthquake excitations (e.g., record-to-record variability of GMs selected) and structure (e.g., geometrical and material properties, mass, damping, stiffness, and strength) are considered (Günay and Mosalam 2013). For this purpose, a computational model of the assessed structure is first developed using simulation programs, such as OpenSees (Mazzoni et al. 2009) and DRAIN-2DX (Prakash et al. 1993). Then, nonlinear time history analyses (NLTHAs) are performed using the GMs selected in hazard analysis. Various procedures of NLTHAs are commonly used: (1) Incremental dynamic analysis (IDA), where a set of GMs is repeatedly scaled to find the IM level at which each GM causes required damage of assessed structure (Vamvatsikos and Cornell 2002); (2) Multiple-stripe analysis (MSA), where analyses are conducted at a specified set of IM levels, each of which has a representative GM set (Jalayer and Cornell 2009); and (3) Cloud analysis, where a large suite of unscaled GMs corresponding to various IM values is used (Jalayer 2003). Output from these

NLTHAs is defined in terms of the selected EDPs, representing various aspects of the structural response (Bazzurro et al. 1998).

Selecting relevant EDPs depends on the performance target and the type of assessed structure (Deierlein et al. 2003). EDPs may include global parameters (e.g., floor acceleration, velocity and displacement, and inter-story drift ratio, IDR), and local parameters (e.g., member force/stress and deformation/strain). Cumulative damage terms (e.g., hysteretic energy) are also possible EDPs in some special conditions such as long-duration GMs, or GM sequences are considered (e.g., Cosenza and Manfredi 2000). To estimate different damageable components of a structure, various EDPs may be necessarily selected. Because the PEER PBEE formulation requires a single value for EDP, the maximum/peak values of the EDPs mentioned above are generally used (Günay and Mosalam 2013).

Unlike the EDPs discussed above, global collapse is treated separately in the PEER PBEE framework, given the fact that its probability does not change from one damageable group to another. Traditionally, global collapse refers to the sidesway mode of collapse and it can be captured when the dynamic analysis algorithm fails to converge in a rigorous mathematical model that considers both material and geometric nonlinearities (i.e., collapse is properly simulated, Chandramohan et al. 2015). This numerical non-convergence corresponds to an infinite increase of EDP for a small increase in IM (i.e., global dynamic instability), and is presented as a flat curve in IDA results (Vamvatsikos and Cornell 2002). In the case of using unscaled GMs or the scaling is inadequate to observe the initiation of dynamic instability accurately, global collapse may be practically determined by considering a large deterministic IDR value as a threshold. This IDR value may be obtained from a prior analysis (e.g., pushover analysis, Günay and Mosalam 2013) or arbitrarily selected (e.g., IDR = 10%, Bakalis and Vamvatsikos 2018). If the maximum IDR value exceeds the threshold, global collapse may occur.

To develop the relationships between selected IM and EDP [i.e., the conditional probabilities of $G(EDP|IM)$ of Eq. (2.8) and $p(EDP|IM)$ in Figure 2.3], data obtained from NLTHAs without global collapse are used. In the cases of IDA or MSA, a lognormal distribution is directly employed to evaluate the PDFs of EDP conditional on the values of IM (Cornell et al. 2002; Romão et al. 2011). However, cloud analysis cannot be treated in the same way, because the analysis results, in terms of the (IM, EDP) points, appear at arbitrary nonidentical IM levels in the IM-EDP space. In this case, the well-known power-law model (Cornell et al. 2002) is normally required to obtain a continuous representation of the distribution of EDP given IM for all IM levels:

$$EDP\left(IM\right)=aIM^{b}\kappa \tag{2.9}$$

where, b and $\ln(a)$ are the slope and intercept in log-space, and κ is a lognormal random variable with unit median and logarithmic standard deviation of $\sigma_{\ln\kappa}$. The latter is interpreted as a constant dispersion of EDP given IM.

Referring to Eq. (2.8), the combined uncertainties in the GM hazard and GM characteristics and variability in IM to EDP can be quantified by integration of the hazard curve, $d\lambda(IM)$, over the $G(EDP|IM)$ for the relevant range of IMs. This approach is known as the probabilistic seismic demand analysis (PSDA, Shome 1999). PSDA consists of the first two key components of PBEE (i.e., hazard and structural analyses) and the principal result is a structural demand hazard curve, i.e., MAF of exceeding a specific EDP, $\lambda(EDP)$, which is expressed as:

$$\lambda\left(EDP\right)=\int G\left(EDP\left|IM\right.\right)\left|d\lambda\left(IM\right)\right| \tag{2.10}$$

where, $\lambda(IM)$ is the ground motion hazard in terms of IM, $d\lambda(IM)$ denotes its differential, i.e., the (annual) probability of observing a particular GM intensity, and the term $G(EDP|IM)$ is the CCDF of EDP given IM, i.e., the probability of the EDP exceeding a specific limit conditioned on knowing IM value.

2.3.3 Damage analysis and fragility functions

Damage analysis is conducted to estimate physical damage of the assessed structure (at component or system levels) as a function of the structural response, considering the uncertainties in the corresponding EDP capacity (EDP_C) terms that define the damage levels and the differences in the pattern and history of the structural response (Günay and Mosalam 2013). Discrete DMs are typically defined in terms of damage levels by different $\mathrm{EDP_C}$ values (e.g., IDR = 10% for global collapse, as discussed in Section 2.3.2). These capacity values are chosen to reflect the consequences or impact on the DVs in loss analysis, such as repair efforts, disruption of function, and life safety (Deierlein et al. 2003; Moehle and Deierlein 2004). To develop the relationships between various DMs and EDPs [i.e., the conditional probabilities of $G(DM|EDP)$ of Eq. (2.8) and $p(DM|EDP)$ in Figure 2.3] and quantify the corresponding $\mathrm{EDP_C}$ values for each damage level, several approaches, including experimental testing, analysis, post-earthquake reconnaissance, and engineering judgment, are commonly adopted (Günay and Mosalam 2013; Moehle and Deierlein 2004).

Traditionally, the term $G(DM|EDP)$, i.e., the probability of DM exceeding a specified damage level conditioned on EDP, may be called component-level fragility function (e.g., Porter et al. 2006). Alternatively, within the context of this dissertation, the “fragility” term is strictly related to the fragility conditioned on IM (rather than EDP), or building-level fragility, which is widely accepted throughout structural and earthquake engineering to describe the susceptibility of a structure (or its component) to seismic excitation (Bakalis and Vamvatsikos 2018). The estimation of seismic fragility is largely based on empirical (e.g., Rossetto et al. 2014), numerical (e.g., D’Ayala et al. 2014), expert opinion data (e.g., Jaiswal et al. 2011), and their combinations. Methodologies, such as processing existing data through pure statistical methods to derive empirical fragility curves (e.g., Lallemant et al. 2015; Noh et al. 2015) and generating new data from computational static and dynamic analyses to develop analytical fragility curves (e.g., Martins and Silva 2021; Rossetto and Elnashai 2005; Shinozuka et al. 2000; Silva et al. 2014b), are commonly adopted. In particular, the second method is employed in this dissertation to develop structure-specific fragility functions, for which custom structural models have been built.

To define the structure-specific fragility, the concept of limit state (reviewed in Section 2.2.1) is required to split the continuous level of damage into discrete damage states by assigning different values as thresholds/capacities. Analogous to DVs, each damage state is associated with a distinct consequence to the operability of the assessed structure or its component (Bakalis and Vamvatsikos 2018). Combined with the PEER PBEE terms, fragility is defined as a probability function, $P(\cdot)$, of a structure’s seismic demand (i.e., an EDP as determined from numerical analysis) at a given level of IM, exceeding an associated capacity threshold (i.e., EDP_C) that indicates the violation of a damage state of interest. This violation then brings the structure into a higher damage state (if it exists). The fragility (F_{DS}) is basically a function of IM and is expressed as:

$$F_{DS}\left(IM\right)=P\left[EDP>EDP_C\left|IM\right.\right] \tag{2.11}$$

According to Eq. (2.11), the fragility curve provides the probabilities that seismic demand exceeds its capacity at all possible IM levels and can be viewed as a summary of all possible single-level safety checks into a continuous function (Bakalis and Vamvatsikos 2018). On the other hand, the LRFD approach for codified design and assessment (Section 2.2) sorely performs a single limit state check at the IM level prescribed by the code, i.e., the probability of exceedance evaluated from the LRFD approach can be considered as one point on the corresponding fragility curve.

Referring back to Eq. (2.8) of the PEER PBEE methodology, fragility function can be obtained by integrating out EDP and preserving the IM conditioning (Miranda and Aslani 2003), and Eq. (2.8) may be re-written as:

$$\lambda\left(DV\right)=\iint G\left(DV\left|DM\right.\right)\left|dG\left(DM\left|IM\right.\right)\right|\left|d\lambda\left(IM\right)\right| \tag{2.12}$$

where, $G(DM|IM)$ may be considered as fragility functions. As implied in Eq. (2.12), fragility curves can be interpreted as the intermediate product of the PBEE framework and act as a link between the hazard analysis and loss estimation (Wilkie 2020).

Ellingwood and Kinali (2009) discussed that fragility analysis is simply an approach to propagate uncertainties from IM to the limit state check of the structure. Several sources of fragility uncertainty are summarized by Bakalis and Vamvatsikos (2018): (1) Record-to-record variability in the relationship between EDP and IM, resulting from the randomness of GMs; (2) Model-related uncertainty, due to the use of imperfect or simplified models for computational efficiency reasons (e.g., Zeris et al. 2007) and the inadequate knowledge or natural randomness in the model properties (e.g., Dolsek 2009; Liel et al. 2009; Vamvatsikos and Fragiadakis 2010); (3) Method-related uncertainty, due to the use of imperfect methodology (e.g., using static analysis for tall buildings, Fragiadakis et al. 2014); and (4) EDP capacity uncertainty, estimated from experimental tests (e.g., Skoulidou and Romão 2019). In general, source (1) is purely aleatory and can be captured by the NLTHA approaches discussed in Section 2.3.2 (i.e., IDA, MSA, and cloud analysis). Source (4) is epistemic, and sources (2) and (3) are usually both aleatory and epistemic. These three uncertainty sources may cause both bias (i.e., a shift of median value) and variability (i.e., increasing dispersion) in the fragility estimation (Bakalis and Vamvatsikos 2018). Therefore, they should be avoided as much as possible.

In the case that a single EDP is employed to characterize the damage state of a structure, seismic fragility estimation can be performed based either on EDP or on IM ordinates. As illustrated in Figure 2.4(a), the probability of exceedance for any horizontal stripe (i.e., IM value is given) of IDA or MSA results can be estimated through the sum of exceeding events over the number of records (N_{rec}) used in NLTHAs, and these records are assumed equiprobable:

$$F_{DS}\left(IM\right)=\frac{\sum_{j=1}^{N_{\mathrm{rec}}}\mathrm{Index}\left(edp^{j}>EDP_{C}\left|IM\right.\right)}{N_{\mathrm{rec}}} \tag{2.13}$$

where, Index(·) is an index function that turns 1 when the argument is true and 0 otherwise, and edp^{j} is the EDP value (at the investigated IM level) corresponding to the j-th GM obtained through NLTHA, i.e., the pink points in Figure 2.4(a). This approach is called EDP-basis, given-IM, or the horizontal statistics procedure (Zareian et al. 2004). Alternatively, IM-basis, given-EDP approach is also used to estimate seismic fragility, as shown in Figure 2.4(b). In this case, the IM ordinates are used to develop the fragility curve, i.e., a single IM-based demand [represented by each horizontal line at a prescribed IM level in Figure 2.4(b)] is compared with multiple IM-based capacities along each given vertical strip [displayed as blue points in Figure 2.4(b)]:

$$F_{DS}\left(IM\right)=P\left(IM>IM_{C}\right)=\frac{\sum_{j=1}^{N_{\mathrm{rec}}}\mathrm{Index}\left(IM>im_{C}^{j}\right)}{N_{\mathrm{rec}}} \tag{2.14}$$

where, im_{C}^{j} is the corresponding IM value of the j-th GM when the response achieves $\mathrm{EDP}_{\mathrm{C}}$ in NLTHA, i.e., the blue points in Figure 2.4(b). For both approaches above,

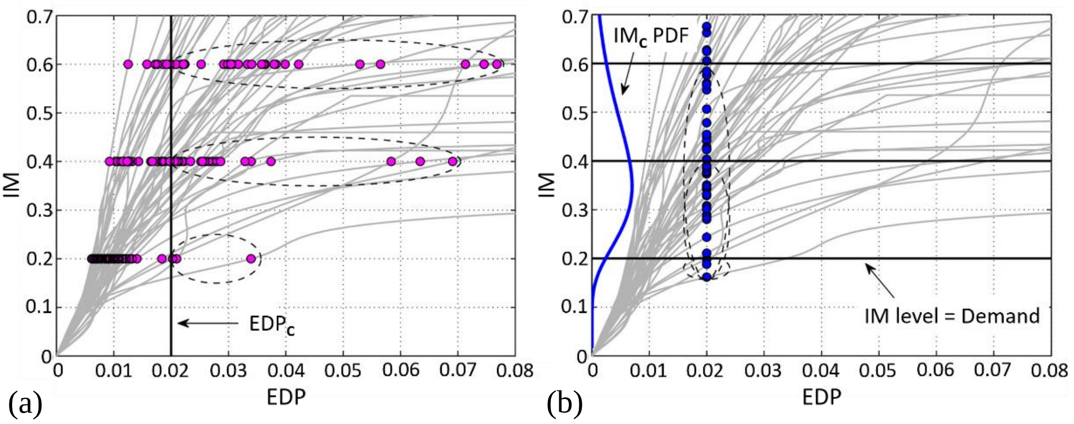

Figure 2.4: Illustrations of (a) EDP-basis approach; and (b) IM-basis approach for deterministic EDP capacity, using IDA results (adapted from Bakalis and Vamvatsikos 2018).

fragility curves may be presented by fitting a lognormal CDF to the discrete probability data points computed at all the IM levels, through either Eq. (2.13) or Eq. (2.14). The parameters of lognormal fit (i.e., the median, μ_{IM}, and the dispersion, β_{IM}), can be determined from 16%, 50%, and 84% IM percentiles, using the moment method or a maximum likelihood method (Baker 2015). The fragility results obtained from both EDP-basis and IM-basis procedures should be fully consistent (Vamvatsikos and Cornell 2004). In addition, it should be noted that these two approaches above assume a deterministic EDP$_C$ value. To incorporate the uncertain EDP$_C$ in seismic fragility derivation, Bakalis and Vamvatsikos (2018) provide the algorithms to account for the EDP$_C$ distribution effect using MCS.

As discussed in Section 2.3.2, global collapse should be treated separately to EDP estimation. This is also important to accurately evaluate seismic fragility. As a result, the total probability theorem should be used to combine the events that the damage state is violated with the mutually exclusive events of collapse (Col) and no collapse (NCol):

$$\begin{aligned} F_{DS}\left(IM\right) = P\left[EDP > EDP_C \left|NCol, IM\right.\right] \cdot \left[1 - P\left(Col\left|IM\right.\right)\right] \\ + P\left[EDP > EDP_C \left|Col, IM\right.\right] \cdot P\left(Col\left|IM\right.\right) \end{aligned} \tag{2.15}$$

where, $P(Col|IM)$ and $P(NCol|IM) = 1 - P(Col|IM)$ are the conditional probabilities of collapse and non-collapse given IM, and the term $P[EDP > EDP_C|Col, IM]$ equals 1 for any EDP value. According to Eq. (2.15), this fragility estimation depends on two groups (i.e., collapse and non-collapse) of analysis data, and may be estimated using a maximum likelihood method or a logistic regression (Baker 2015).

When seismic fragility is evaluated from cloud analysis data, the aforementioned approaches are not applicable through Eq. (2.13) and Eq. (2.14). In this case, the power-law model of Eq. (2.9) (i.e., the regression result of the IM-EDP relation) is necessary to estimate the seismic fragility. Given Eq. (2.9), the seismic fragility function of cloud analysis results may be derived from Eq. (2.11) as follow, with the lognormality assumption for both EDP demand and capacity (and thus their ratio):

$$\begin{aligned} F_{DS}\left(IM\right) &= P\left[EDP > EDP_C \left| IM\right.\right] = P\left[EDP\left(IM\right) > EDP_C\right] \\ &= P\left(\ln\left(\frac{EDP\left(IM\right)}{EDP_C}\right) > \ln 1\right) = \Phi\left(\frac{\ln EDP(IM)_{50\%} - \ln EDP_{C,50\%}}{\beta_{EDP(IM),\text{tot}}}\right) \\ &= \Phi\left(\frac{\ln\left(aIM^b\right) - \ln EDP_{C,50\%}}{\beta_{EDP(IM),\text{tot}}}\right) = \Phi\left(\frac{\ln a + b\ln IM - \ln EDP_{C,50\%}}{\beta_{EDP(IM),\text{tot}}}\right) \\ &= \Phi\left(\frac{\ln IM - \ln\left[\left(\frac{EDP_{C,50\%}}{a}\right)^{1/b}\right]}{\beta_{EDP(IM),\text{tot}}/b}\right) = \Phi\left(\frac{\ln IM - \ln IM_{C,50\%}}{\beta_{IM,\text{tot}}}\right) \end{aligned} \tag{2.16}$$

In the final output of Eq. (2.16), $IM_{C,50\%}$ is the median (usually denoted μ_{IM}, i.e., the IM level with 50% probability of exceeding the damage state) of the fragility function, and $\beta_{IM,\text{tot}}$ is the standard deviation of lnIM (also known as the dispersion of IM). Assuming that demand and capacity are uncorrelated, then $\beta_{IM,\text{tot}}$ can be expressed as follow using the square root sum of squares (SRSS) rule:

$$\beta_{IM,\text{tot}} = \frac{\beta_{EDP(IM),\text{tot}}}{b} = \frac{\sqrt{\beta^2_{EDP(IM)} + \beta^2_{EDP_C}}}{b} \tag{2.17}$$

In Eqs. (2.16) and (2.17), $\beta_{EDP(IM),\text{tot}}$ is the total associated dispersion of median capacity and demand estimates. The term β_{EDP_C} is the dispersion of lnEDP_C due to the epistemic uncertainty sources (as discussed above). It can be captured if EDP$_C$ distribution has been obtained from laboratory tests (e.g., Lignos et al. 2011;

Stillmaker et al. 2016). The FEMA P-58 (ATC 2012) approach may be used to assign β_{EDP_C} according to an assumed normal or lognormal $\mathrm{EDP_C}$ distribution when the relevant experiments are not available. Moreover, in case a deterministic $\mathrm{EDP_C}$ is employed, β_{EDP_C} may be handily assumed as zero. The term $\beta_{EDP(IM)}$ represents the aleatory variability (mainly record-to-record variability) around the median demands, and it can only be explicitly evaluated through IDA or MSA (Bakalis and Vamvatsikos 2018). In this case, when a power-law fit is performed to characterize IM-EDP relation from cloud analysis data, $\beta_{EDP(IM)}$ can be determined with the homoscedasticity assumption:

$$\beta_{EDP(IM)} = \sqrt{\frac{\sum_{i=1}^{N_{\mathrm{rec}}} \left[\ln\left(edp_i\right) - \ln\left(a \cdot im_i^b\right) \right]^2}{N_{\mathrm{rec}} - 2}} \tag{2.18}$$

where, N_{rec} is the total number of selected GMs for cloud analysis, edp_i is the EDP value corresponding to the i-th GM obtained through cloud-based NLTHA, and im_i is simply the IM value of the i-th GM.

The discussion on seismic fragility above is based on the assumption that the structural response is adequately characterized by a single EDP and its associated failure mode. However, several cases exist in which multiple EDPs may dominate the violation of a system damage state (e.g., Bakalis et al. 2017; Jalayer et al. 2007). Then, the seismic fragility may be estimated as following considering a union of possible failure modes:

$$F_{DS}\left(IM\right) = P\left[\left(EDP_1 > EDP_{1,C} \left| IM\right.\right) \cup \ldots \cup \left(EDP_k > EDP_{k,C} \left| IM\right.\right)\right] \tag{2.19}$$

where, k is the number of EDPs and their corresponding failure modes, each of which may individually trigger the damage state violation, EDP_i and $EDP_{i,C}$ ($i = 1, \ldots, k$) are the demand and capacity of each failure mode.

2.4 Reliability-based design of ECBP connections

ECBPs are common column-base connections used in low- to mid-rise SMRFs to transfer forces from the entire structure to the supporting foundation. The mechanical behavior of ECBPs plays an important role in the overall performance and stability of the structure (e.g., Picard et al. 1987). In particular, they may be relied on to withstand intensive seismic loads in SMRFs (Gomez 2010). ECBP connections are susceptible to several load conditions, including axial compression, axial uplift, shear, flexure, and combined loadings. This dissertation mainly focuses on the design and assessment of ECBPs under one of the dominant combinations in reality – moment and axial force. Even though shear is also important, it is not considered and is assumed to be transferred independently, e.g., through a shear key (e.g., Gomez et al. 2011).

Previous experimental studies have been conducted to investigate the component behavior and response of ECBPs subjected to axial loading (e.g., DeWolf 1978; Hawkins 1968), flexural loading (e.g., LaFraugh and Magura 1966; Melchers 1992; Targowski et al. 1993), and their combinations (e.g., DeWolf and Sarisley 1980; Gomez et al. 2010; Hon and Melchers 1988; Kanvinde et al. 2015; Petrone et al. 2016; Picard and Beaulieu 1985; Takamatsu and Tamai 2005; Thambiratnam and Paramasivam 1986). Effects of ECBP behavior on the seismic response of steel frames were also tested (e.g., Kurata et al. 2005; Lignos et al. 2013).

Several analytical and finite element modeling (FEM) investigations of ECBPs loaded in combined axial and flexural loadings were carried out to characterize the mechanical behavior. These include the bearing stress characterization between base plate and concrete foundation (e.g., Drake and Elkin 1999), strength characterization of base connection (e.g., Kanvinde et al. 2013; Penserini and Colson 1989), bending and yielding behavior estimation of base plates (e.g., Targowski et al. 1993; Thambiratnam and Krishnamurthy 1989), initial (rotational) stiffness and moment-rotation response modeling (e.g., Cui et al. 2019; Dumas et al. 2006; Galambos 1960; Kanvinde et al. 2012; Latour and Rizzano 2019; Trautner and Hutchinson 2018; Wald et al. 2008; Wald and Jaspart 1998), among others. Moreover, Greek researchers have developed a series of rigorous, closed-form analytical solutions to characterize ECBP behavior (e.g., Ermopoulos and Michaltsos 1998; Ermopoulos and Stamatopoulos 1996a; b; Stamatopoulos and Ermopoulos 1997). However, these procedures are complex, highly iterative, and ill-suited for practical structural design and analysis (Dumas et al. 2006).

Detailed reviews of ECBP connections can be found in Grauvilardell et al. (2005) and Hensman and Nethercot (2000). These experimental and analytical studies provide background and form the foundation to conduct reliability analysis for ECBPs (one of the objectives of this dissertation). The following subsections present a review associated with the current state of design and reliability assessment of ECBP connections.

2.4.1 Current design practice

Several design methods for ECBP connections subjected to combinations of axial forces and moments are available in the literature, e.g., the first edition of AISC Design Guide One (DeWolf and Bicker 1990), the Astaneh-Asl et al. (1992) method, the Drake and Elkin (1999) method, the Fahmy (2000) method, the Wald component method (Wald 2000), and the currently used AISC Design Guide One (DG1, Fisher and Kloiber 2006). These methods were developed based on different assumptions for ASD or LRFD approaches, and on bearing stress distribution, effective bearing area (due to plate bending), and interactions between the components of the ECBP connections (Aviram and Stojadinovic 2006). Among them, the DG1 method (Fisher and Kloiber 2006), which is an application of the LRFD methodology, is widely accepted and implemented in the US engineering practice. Figure 2.5 illustrates the key assumptions of the DG1 method. Note that the superscript (i.e., DG1) of some symbols in the figure indicates the design method used to determine the internal forces and moments in the ECBP connections. Because this method is well-documented in the design guide itself, it is only briefly summarized here.

Referring to Figure 2.5, the axial compression (P) and moment (M) combination is resisted by (1) a compression stress block of constant magnitude (= f), if the axial force is high relative to moment, i.e., a low-eccentricity condition; or (2) a compression stress block (of magnitude = $f_{\max}^{\mathrm{DG1}}$) supplemented by tension ($T_{\mathrm{rods}}^{\mathrm{DG1}}$) that develops in the anchor rods as the base plate uplifts when the axial compression is low compared to the moment, i.e., a high-eccentricity condition. The process for design involves the following steps.

Firstly, determine whether the condition is low- or high-eccentricity. For this, the critical value of load eccentricity (e_{crit}) is determined as:

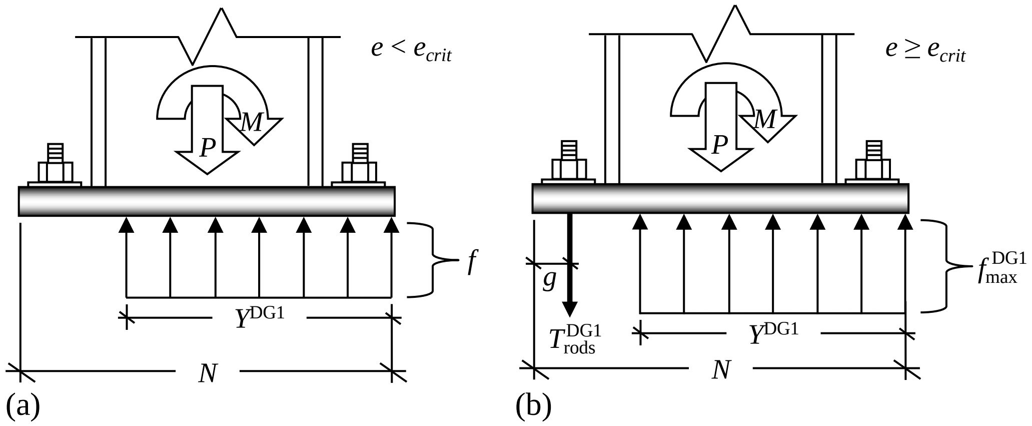

Figure 2.5: Internal stress distributions used in the DG1 method: (a) low-eccentricity; and (b) high-eccentricity conditions.

$$e_{crit} = \frac{N}{2} - \frac{P}{2 \cdot B \cdot f_{max}^{DG1}} \tag{2.20}$$

where, the terms B and N are the length and width of the base plate. The preceding equation assumes that the bearing side of the connection develops a rectangular stress block with a constant magnitude f_{max}^{DG1}, determined as:

$$f_{max}^{DG1} = \phi_{bearaing} \times \min\left(f_{grout}, f_{concrete} \right) \tag{2.21}$$

where, the $\phi_{bearing}$-factor is taken as 0.65, f_{grout} is the crushing strength of the grout, and $f_{concrete}$ is estimated as in the subsequent equation, accounting for the effects of concrete confinement (if the footing is larger than the base plate):

$$f_{concrete} = 0.85 \cdot f_c' \cdot \sqrt{\frac{A_2}{A_1}} \leq 1.7 \cdot f_c' \tag{2.22}$$

where, f_c' is the compression strength of the concrete, A_1 is the bearing area of the plate, and A_2 is the effective area of the concrete (typically the plan area of the footing). The grout pad is usually not confined similarly because it is above the concrete surface. Thus, a similar adjustment is not required for the grout strength (f_{grout}).

For the low-eccentricity condition, i.e., the design load eccentricity e (= M/P) < e_{crit}, the magnitude of the upward bearing stresses f, as well as the stress block length Y^{DG1} [Figure 2.5(a)], may be readily calculated through force and moment equilibrium.

If a suitable equilibrium solution cannot be found with $f < f_{\max}^{\mathrm{DG1}}$ and $Y^{\mathrm{DG1}} < N$, then the base plate plan dimensions must be resized; the concrete/grout bearing failure check is applied implicitly in this manner. This design check is denoted as BF [Figure 2.6(a)]. For this design condition, the only other possible mode of failure is flexural yielding of the base plate on the compression side due to bearing stresses; this is calculated by assuming that the toe of the base plate bends upwards as a cantilever flap, with a yield line parallel to the edge of the column compression flange. This design check is denoted as PC [Figure 2.6(b)]. Specifically, failure is assumed to occur if the cantilever moment (denoted $M_{pl,comp}^{\mathrm{DG1}}$) over the yield line exceeds the reliable capacity of the base plate, i.e., $\phi_{\mathrm{plate}} \times M_p^{\mathrm{plate}}$, and $\phi_{\mathrm{plate}} = 0.9$. The term M_p^{plate} refers to the plastic moment capacity of the base plate, and is expressed as:

$$M_p^{\mathrm{plate}} = F_{y,pl} \cdot B \cdot \frac{t_p^2}{4} \tag{2.23}$$

where, $F_{y,pl}$ is the yield strength of base plate steel, and t_p is the thickness of base plate.

if $e \geq e_{crit}$, i.e., the high-eccentricity condition [Figure 2.5(b)], then the stress in the bearing zone is assumed to reach its maximum value (i.e., $f_{\max}^{\mathrm{DG1}}$), such that the two remaining unknowns, i.e., the stress block length Y^{DG1} and the tension forces in the anchor rods $T_{\mathrm{rods}}^{\mathrm{DG1}}$ may be calculated from force and moment equilibrium, as per the following equations:

$$Y^{\mathrm{DG1}} = (N-g) - \sqrt{(N-g)^2 - \frac{2 \cdot \left[M + P \cdot \left(\frac{N}{2} - g \right) \right]}{f_{\max}^{\mathrm{DG1}} \cdot B}} \tag{2.24}$$

$$T_{\mathrm{rods}}^{\mathrm{DG1}} = f_{\max}^{\mathrm{DG1}} \cdot B \cdot \left((N-g) - \sqrt{(N-g)^2 - \frac{2 \cdot \left[M + P \cdot \left(\frac{N}{2} - g \right) \right]}{f_{\max}^{\mathrm{DG1}} \cdot B}} \right) - P \tag{2.25}$$

This results in four possible limit states, and associated design checks. As in the low-eccentricity case, the BF design check is applied implicitly, such that failure is assumed to occur if $Y^{\mathrm{DG1}} > N - g$ [where g is the distance between the center of the

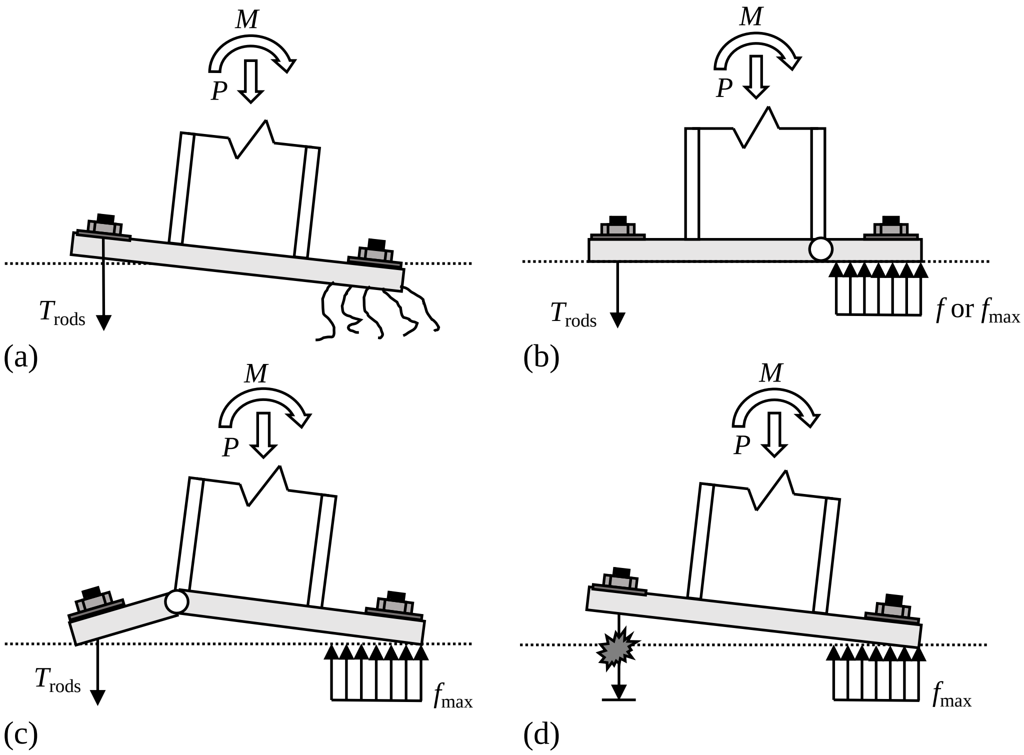

Figure 2.6: Schematic illustration of possible failure modes of ECBP connections subjected to flexure and axial forces: (a) BF – bearing failure of the grout/concrete foundation; (b) PC – plate yielding failure on the compression side; (c) PT – plate yielding failure on the tension side; and (d) AT – anchor rod tensile failure.

anchor rods to the edge of the base plate; see Figure 2.5(b)], which indicates that the bearing zone extends into the tension anchor rods (which is impossible from a compatibility standpoint). For the base plate, two limit states are possible: (1) the PC limit state due to upward bearing on the compression side, and (2) flexural yielding of the base plate on the tension side due to downward tension forces in the anchor rods. This is denoted PT [Figure 2.6(c)], and evaluated by comparing the moment in the plate due to the anchor forces $T_{\text{rods}}^{\text{DG1}}$ (denoted $M_{pl,ten}^{\text{DG1}}$) and the reliable capacity $\phi_{\text{plate}} \times M_p^{\text{plate}}$. For the PT limit state, the controlling mechanism may involve either a yield line parallel to the column flange or inclined to the plate edge, depending on the location of the anchor rods. The final limit state is the tensile failure of anchor rods themselves [denoted AT, Figure 2.6(d)], which is determined to occur if

$$\frac{T_{\text{rods}}^{\text{DG1}}}{n_{\text{rods}}} > \phi_{\text{rod}} \times 0.75 \cdot F_u^{\text{rod}} \cdot A_{\text{rod}} \tag{2.26}$$

where, n_{rods} is the number of anchor rods in a line, F_u^{rod} is the ultimate strength of the rod, A_{rod} is the unthreaded area of anchor rod, and $\phi_{\text{rod}} = 0.75$. Other anchor limit states include rod pullout or concrete blowout. These depend on the footing configuration and reinforcement, and are outside the scope of this dissertation. ACI 318 (ACI 2019) provides greater details on these limit states check.

2.4.2 Reliability analysis studies

It is noticed that previous research on the topic of reliability analysis of ECBP connections is sparse. To the author’s knowledge, only two such studies are found in the literature and they are briefly summarized in this subsection.

Aviram et al. (2010) carried out a reliability assessment for an external ECBP connection of a typical three-story SMRF located in Berkeley, California. This sample ECBP was designed as per the DG1 method, and the design loads were obtained from the median response values of a set of seven NLTHA results of the SMRF joint reactions, according to the 10% probability of exceedance in 50 years seismic hazard level (i.e., design basis earthquake level). A set of RVs was identified and a hierarchy of diverse ECBP limit states (failure modes) was formulated. Component and system reliability indices of the specific connection at four seismic hazard levels (i.e., 2, 5, 10, and 50% probabilities of exceedance in 50 years) were estimated using the FORM and SORM approximations. The results indicate that the probability of failure (P_f) of the assessed ECBP connection in a 50-year period is 2.43% (corresponding to a reliability index $\beta = 1.97$), which is relatively high for a critical structure connection. As a result, this study concludes that the DG1 method to design ECBPs is unconservative and suggests that the resistance (ϕ-) factors used in this method may be decreased.

Torres-Rodas et al. (2020) also conducted a reliability assessment of ECBP connections designed as per the DG1 method. This study established an overall limit state considering the P-M interaction to replace the conventional individual limit state checks for each component (as discussed in Section 2.4.1). ECBPs were designed for two- and four-story archetype SMRFs (considering high seismicity) and design loads were obtained according to the current seismic criteria of ASCE 7-16 (ASCE 2016). Unlike the earlier-discussed study, this reliability assessment only took into account the uncertainty in seismic demands by performing NLTHAs of 120 sets of bidirectional GMs at eight seismic hazard levels. This simplification may lead to inaccurate estimation of failure probability (and associated reliability index) of ECBPs. Nonetheless, the analysis results still show that the safety margin guaranteed by the DG1 method is, by large, unacceptable.

2.5 Seismic performance of WCS connections

Compared to other welded connections (e.g., welded beam-to-column connections) in SMRFs, research on WCS is relatively sparse. Only few studies have been conducted to examine WCS connections, typical of pre-Northridge construction. Bruneau and Mahin (1990, 1991) carried out tests for two column splice specimens – one featured partial joint penetration (PJP) welds in the flanges with 50% penetration, and the other one featured complete joint penetration (CJP) welds with weld access holes. These two specimens were constructed to replicate the erstwhile construction of WCS in the US. In each test, the spliced column was subjected to cyclic loading under a four-point bend configuration, such that each WCS was located in the region of pure bending. Two main observations of the study were that (1) the WCS with CJP welds showed its ability to sustain the applied moments larger than the cross-sectional strength of the smaller connected column; and (2) the net-section strength of the PJP welded splices (i.e., the strength of the cross-sectional area, discounting the unfused root region) was reached before the brittle fracture of the whole connections. Nuttayasakul (2000) then performed finite element fracture mechanics (FEFM) simulations of the Bruneau and Mahin (1991) tests and confirmed their findings. Results of additional parametric simulations of WCS details with PJP welds also indicate that pre-Northridge weld materials with effective throat thickness greater than 50% of flange thickness may have had sufficient toughness to develop the net-section strength of the PJP connection, even if a minimum toughness is not specified.

Gagnon and Kennedy (1989) conducted a series of 75 tensile tests on PJP welds (for steel plates) similar to those in WCSs. Behavior and ultimate tensile strength of PJP welds were characterized in this study. The fracture failure criteria established in terms of the longitudinal stress in the column flange may be borrowed for assessing the seismic performance of WCS. In addition, Hayes (1957) and Popov and Stephen (1977) have examined the response of pre-Northridge WCSs in compression.

The first study to investigate seismic demands of WCSs in SMRFs was conducted by Shen et al. (2010), which characterized the axial force, moment, and deformation demands of WCSs through NLTHA. The NLTHA was performed for mid- to high-rise (i.e., 4-, 9-, and 20-story) SMRFs subjected to a set of 20 GMs representative of the Southern California region. This study was later extended by Akbas et al. (2014) to consider additional building configurations. These simulation results indicate that the inelastic deformation of WCS is minimal, even when subjected to GM intensities significantly higher than the design level shaking. However, the axial force demands in WCSs can approach the capacity of the smaller connected column. This observation implies that the fracture of PJP welded column splice is sensitive to a peak tensile stress in the flange of the connection, and WCS may be considered as a “force-controlled” component.

Inspired by the findings above, Shaw (2013) and Shaw et al. (2015) conducted a series of five full-scale tests on a proposed detail for WCSs under reversed cyclic loading. This detail combines high-penetration PJP welds (i.e., the effective throat thickness > 80% of the flange thickness) with toughness-rated weld materials that are specified in the post-Northridge construction practice. The tests showed that all the specimens designed in this manner can achieve full moment capacity of the smaller connected column along with a high degree of inelastic deformation capacity before fracture with yielding in both the smaller and larger columns. The FEFM simulations conducted in the same studies also showed that the inelastic deformation demands of the tested specimens were modest. These findings demonstrate that the proposed WCS connection can offer satisfactory (i.e., ductile) seismic performance. Therefore, this detail may be considered as an economical alternative to the CJP welded splice, which is currently required for post-Northridge construction of SMRFs in seismic regions. Furthermore, Stillmaker et al. (2016) developed functional forms to characterize the strength (fracture capacity) of WCS with PJP weld details, considering various parameters that describe the splice configuration and weld material property. This was achieved by a fracture-mechanics-based approach, which includes (1) generalizing test data by Shaw et al. (2015) to develop FEFM simulations, and (2) formulating functions to determine WCS strength based on the FEFM results.

All the studies discussed above can help to understand the seismic response, in terms of failure modes, seismic demands, and strength capacity, of WCS connections that featured with PJP welds. Based on some of their findings, Galasso et al. (2015) conducted rigorous PSDA, fracture fragility derivation, and fracture risk assessment for both the pre-Northridge PJP splices and the proposed PJP splices [as suggested by Shaw et al. (2015)], adopting a PBEE framework. The major findings are that (1) the fracture risk of pre-Northridge WCSs featuring PJP welds is unacceptably high, indicated by relatively low expected return periods of fracture (i.e., 75 years), and (2) the tensile stress demands of proposed WCSs in the assessed high-rise (20-story) SMRF are fairly lower than the expected yield stress, even determined at the MCE (Maximum considered earthquake) hazard level. Motivated by the first finding of Galasso et al. (2015) discussed above, a subsequent PBEE-based study has been conducted to examine the influence of WCS fracture and fracture propagation on the seismic response of SMRFs (Stillmaker et al. 2017). This study simulated the post-fracture response of WCSs through a new material in computational models, which was informed by fracture-mechanics based estimates of splice strength (Stillmaker et al. 2016), and replicated post-fracture phenomena (i.e., loss of tensile capacity, as well as the subsequent gapping and closure) of WCSs. Both studies discussed in this paragraph indicate that low strengths of pre-Northridge WCSs lead to a high vulnerability to fracture. A preliminary study on the initiative to retrofit these WCSs in existing buildings has been provided by Nudel et al. (2015).

2.6 Research gaps

As introduced in Chapter 1, the focuses of this dissertation are two-fold: (1) the reliability-based design of ECBPs through re-examining the reliability of the current design method; and (2) the performance-based fracture fragility/risk assessment of pre-Northridge WCSs by taking advantage of recent advancements of PBEE research. Within the scope of the dissertation, several research gaps and limitations from previous research are identified and discussed below.

According to Section 2.4.1, the prevalent approach to design ECBP connections (through DG1) is well-established from a mechanistic standpoint. However, the reliability of ECBPs designed as per this approach is not as well understood. As discussed in Section 2.4.2, only two studies (i.e., Aviram et al. 2010; Torres-Rodas et al. 2020) have directly examined the structural reliability of ECBPs. Although both studies concur that the safety margin provided by the DG1 approach is inadequate, it is somewhat limited in their scopes. Thus, it is difficult to generalize the findings. In particular, Aviram et al. (2010) only examined one external ECBP connection, and (Torres-Rodas et al. 2020) sorely focused on the uncertainty in seismic demands. Moreover, a closer examination of the DG1 approach shows that each of the design checks outlined in Section 2.4.1 includes $f_{\max}^{\mathrm{DG1}}$ and consequently ϕ_{bearing} which is used to estimate it. The nonconservatism is readily apparent for the PC check because ϕ_{bearing} reduces the bearing stress, which acts as a load (demand) on the cantilever flap for the PC limit state. The effect of ϕ_{bearing} on the other limit states is not as direct [Eqs. (2.24) and (2.25)]. Nonetheless, it is evident that for the same reasons as for the PC check, incorporating ϕ_{bearing} within the design checks is not appropriate and is likely to result in biased or inaccurate characterizations of reliability. Finally, ϕ_{plate}- and ϕ_{rod}-factors in the independent design checks are borrowed in an ad hoc manner from other similar components, which do not consider either the accuracy of the demand estimation within the individual components or the variability within it. This is also inappropriate from the perspective of estimating reliability. In summary, a detailed reliability analysis of the DG1 approach, which accounts for a wide range of design scenarios, load combinations, and uncertainty sources, has not been conducted to date. Also, it may be necessary to eliminate the use of ϕ_{bearing}-factor in the design checks other than BF and re-calibrate ϕ_{plate}- and ϕ_{rod}-factors to ensure acceptable reliability of designed ECBP connections.

According to Section 2.5, only one study (Galasso et al. 2015) conducted a fracture fragility and risk assessment on WCSs within the PBEE framework. This study did provide important first-order estimates of fracture risk in pre-Northridge WCSs. However, it relied on some simplifying assumptions and subjectivities relating to the uncertainty characterization of stress demands and fracture capacities of WCSs, which may strongly affect the accurate estimation of fracture fragility and risk. Within the PBEE framework, several improvements can be taken to refine the assessment. As to the hazard analysis, Galasso et al. (2015) used $S_a(T_1)$ as an IM. This is somehow questionable because higher-mode effects can drive WCS stress demands in high-rise

SMRFs. It is important to select an optimal IM (as discussed in Section 2.3.1) to enable more accurate estimation. In terms of the structural analysis, all the previous studies only quantified WCS seismic demands using horizontal GMs. This is concerning because it is well known that the vertical ground shaking may contribute significantly to the axial forces and stresses (i.e., the seismic demands of WCS) in the columns of mid- to high-rise SMRFs (in which WCSs are typically used). For the fracture fragility analysis, Galasso et al. (2015) merely employed a deterministic value as the fracture capacity without considering uncertainty in this capacity. However, Stillmaker et al. (2016) indicated that the uncertainty is usually significant in WCS fracture capacity determination. Collectively, it is necessary to refine fracture fragility/risk assessment for WCS connections, rigorously considering uncertainties in estimating seismic stress demand and fracture capacity through some recent advancements in the PBEE framework (as discussed in this paragraph and also Section 2.3).

It is worth noting that all the previous simulation-based studies on the seismic demand estimation of WCSs (as reviewed in Section 2.5) primarily focused on the ordinary (non-pulse-like) GMs. Several recent earthquakes have highlighted the increased collapse risk of structures in near-fault sites (e.g., Chioccarelli and Iervolino 2010). This is mainly due to the possible occurrence of pulse-like GMs that cause higher global deformation demands in structures. However, the potential increase of stress demands that control the fracture of pre-Northridge WCSs, has not been properly evaluated in the presence of pulse-like GMs. As a result, it is also a beneficial supplement to expand the fracture fragility/risk assessment for WCS in near-fault regions to address the effects of pulse-like GMs on the distribution of WCS stress demands. The state-of-the-art NS-PSHA models within the PBEE framework may be adopted.

This dissertation aims to address these presented research gaps in the following chapters.

Chapter 3

Reliability Analysis and Design Considerations for Exposed Column Base Plate Connections

Adapted from **Song, B.**, Galasso, C., and Kanvinde, A. (2021). "Reliability Analysis and Design Considerations for Exposed Column Base Plate Connections Subjected to Flexure and Axial Compression." *Journal of Structural Engineering*, 147(2), 04020328.

3.1 Introduction

Exposed column base plate (ECBP) connections are widely used in low- to mid-rise steel moment-resisting frames (SMRFs) to transfer forces from the entire structure through the first-story column into the concrete footing. Figure 3.1 schematically illustrates an ECBP connection detail commonly used in the US, and featured in design guidelines including the American Institute of Steel Construction's AISC Design Guide One (Fisher and Kloiber 2006), the Seismic Design Manual (AISC 2018), the AISC Specification (AISC 2016a), and the Seismic Provisions (AISC 2016b). Referring to the figure, the axial force and moment are transferred through a combination of upward bearing stresses (in the grout or supporting concrete) on the compression side of the connection, and downward tensile forces (in the anchor rods) on the tension side of the connection. Shear may be transferred either through friction (if sufficient compression is present), through the anchor rods, or through a shear key, if provided (Gomez et al. 2011). In the US, Design Guide One (abbreviated DG1

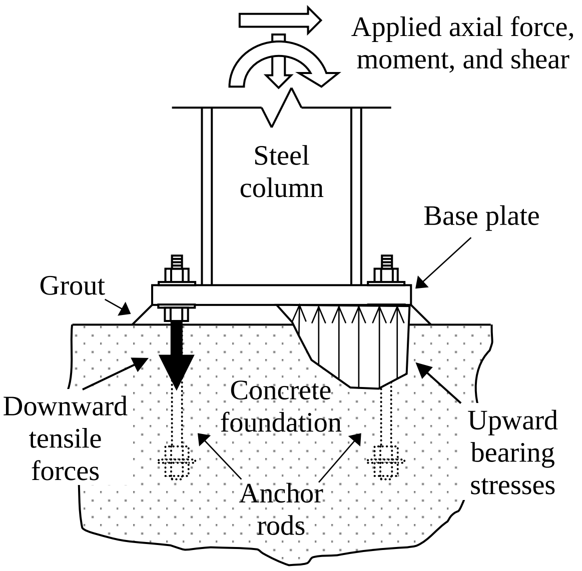

Figure 3.1: Schematic illustration of an exposed column base plate (ECBP) connection and force transfer mechanisms.

henceforth) is the primary document guiding the design of ECBP connections under combinations of axial compression, flexure, and shear. The DG1 utilizes the internal stress distributions proposed by Drake and Elkin (1999). Connections that utilize similar details and force transfer mechanisms are used in other regions as well, e.g., Wald (2000) for Europe, and Cui et al. (2009) for Japan. Consequently, they have been studied extensively in various contexts. Ermopoulos and Stamatopoulos (1996a) developed closed-form analytical solutions to characterize internal force distributions, and work by Gomez et al. (2010) and Kanvinde et al. (2013) has examined the efficacy of the DG1 method through experiments and finite element simulations, respectively. Other relevant work in the area includes Lee et al. (2008a; b) and Wald (2000) to examine various geometrical configurations and issues such as weld fracture, which may occur under earthquake-type cyclic loading (e.g., see Fahmy 2000; Myers et al. 2009). More recently, the focus has shifted to the seismic performance of these connections to investigate their possible use as dissipative fuses (e.g., Falborski et al. 2020; Trautner et al. 2016).

These studies concur that the Drake and Elkin (1999) approach (which underlies the de facto design method in the US through DG1) is effective from a mechanistic standpoint, i.e., it is able to satisfactorily characterize the internal force distribution within ECBP connections in a deterministic sense (Gomez et al. 2010; Kanvinde et al.

2013). However, a closer examination of the method (and associated literature) from a probabilistic standpoint (e.g., Aviram et al. 2010) reveals inconsistencies (in the failure probabilities across the various components of the connections) that must be addressed to ensure that ECBP connections meet target reliability (i.e., provide acceptable probabilities of failure/safety levels). These issues emerge because the approach treats the ECBP connection as a collection of components, each designed separately, without considering their collective effect on the connection failure. Specifically, the approach determines an internal force distribution (i.e., forces in the anchor rods, and bending moments in the base plate) based on an assumed bearing stress distribution in the concrete/grout, and then applies design checks independently to each of these components (i.e., the anchor rods and base plate) by comparing these estimated forces/moments to their capacities, modified by resistance (i.e., ϕ-) factors. This is problematic for numerous reasons:

- Connection failure is controlled by the interactions of these components. Research by Gomez et al. (2010) and Kanvinde et al. (2015) has indicated that flexural yielding of the base plate on the compression side of the connection does not result in connection failure, unless also accompanied either by yielding of the anchor rods, or by flexural yielding of the base plate on the tension side. Applying design checks independently to these components disregards this effect, resulting in undue conservatism.
- From the perspective of system reliability, applying the design checks independently is inappropriate, because the probability of failing one design check may not necessarily correspond to failure of the entire connection.
- The assumed bearing stress in the concrete (used for determination of the internal force distribution) includes a ϕ_{bearing}-factor (see Section 2.4.1) to incorporate the uncertainty in this stress. While this is suitable for design of the concrete footing itself (to provide a conservative estimate of bearing stress), it cannot be justified for the design of the other components (i.e., base plate and anchor rods). This is because the bearing stress effectively acts as a demand on these other components through overall equilibrium of the connection, such as that a lower estimate of bearing stress may, in fact, be unconservative.

- Finally, the ϕ_{plate}- and ϕ_{rod}-factors in the independent design checks for the anchor rods and base plates (see Section 2.4.1) are borrowed in an ad hoc manner from other similar components, and are not based on reliability analysis. Specifically, the design checks consider only the uncertainty in capacities of the components and disregard both the uncertainty as well as bias in the estimated forces and moments in these components.

Other researchers have also noted that the DG1 approach does not incorporate reliability analysis. Torres-Rodas et al. (2020) performed reliability analysis for the DG1 approach, with a primary focus on uncertainty in seismic demands. Their analysis addresses the overall response of the connection, and does not consider the interaction of various components. Nonetheless, the results indicate that the reliability provided by the DG1 approach is unacceptable. In summary: (1) while well-intentioned, the DG1 approach fails to effectively incorporate system reliability as well as overall connection response, and (2) given the complex and sometimes counteracting nature of the effects noted previously, consistent connection reliability cannot be ensured. In response to these issues, this dissertation conducts a detailed analysis of the current DG1 approach for the design of ECBP connections, with the following objectives:

1. To examine the level of connection reliability (conventionally quantified by the reliability index β) provided by ECBP connections designed as per the DG1 approach, with a focus on its consistency across various design scenarios as well as component failure modes;
2. To identify deficiencies in the DG1 approach and examine possible enhancements that are based on considering system response, and eliminating the use of ϕ-factors that do not comport with physics; and
3. Based on these analyses, to suggest prospective design strategies that ensure acceptable and consistent performance/reliability, while also incorporating overall connection behavior.

A detailed review of the DG1 approach has been provided in Section 2.4.1 and is not repeated here. This chapter begins with a summary of the methodology used for reliability analysis. A set of 59 design scenarios (SMRF columns for which ECBP connections must be designed) that represent various combinations of gravity, wind, and seismic loading are then described. For each of these scenarios, ECBP connections are designed using existing as well as proposed approaches, and reliability analyses are conducted using Monte Carlo simulations modeling several sources of uncertainty. The chapter concludes by providing commentary regarding the analyzed approaches and suggesting strategies that ensure consistent reliability.

3.2 Methodology for reliability assessment of ECBP connections

This section describes the process of evaluating the reliability of ECBP connections for which the nominal configuration (e.g., geometry, material properties), as well as the design loadings are known. Once this process is established for a given connection, it may be used to test alternative strategies resulting in specific designs. The main steps involved in this process (Figure 3.2) are:

- Developing a set of representative and realistic loading scenarios, in terms of the applied moment (M) and axial forces (P) combinations at column bases for which ECBP connections are to be designed.
- Designing the ECBP connections as per the appropriate design method (DG1 or prospective), sometimes resulting in multiple configurations, each of which satisfies all design checks.
- Identifying sources of uncertainty in each designed configuration. For each configuration, formulating limit state functions associated with each failure mode, i.e., BF (bearing failure of the grout/concrete foundation), PC (plate failure on the compression side), PT (plate failure on the tension side), and AT (anchor rod failure on the tension side), see Section 2.4.1 and Figure 2.6 for details.
- Performing Monte Carlo sampling that utilizes the statistical distributions of input random variables (RVs) to assess the probability of failure (P_f) and reliability indices (β) of each designed configuration.

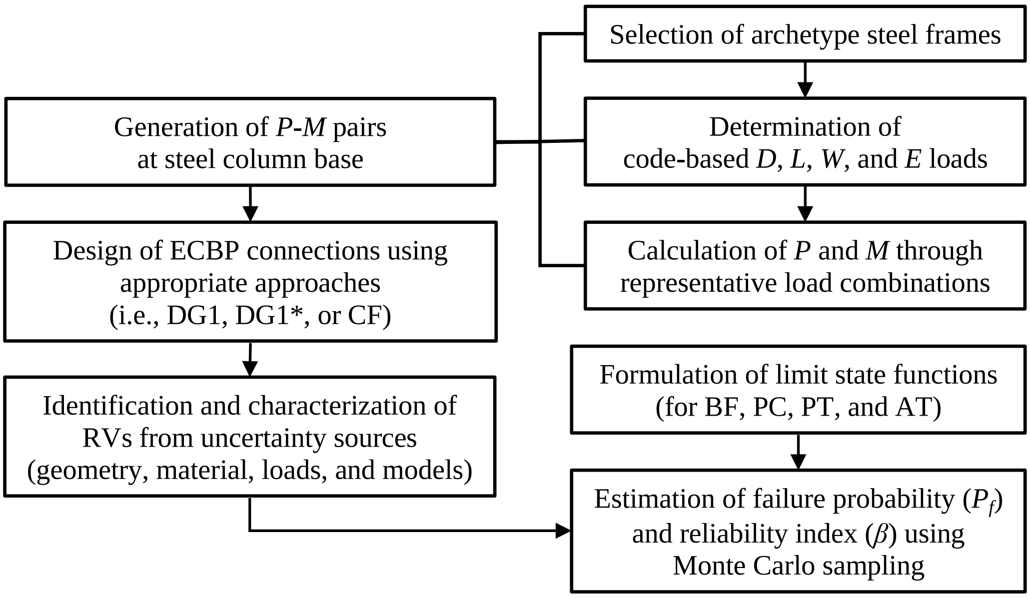

Figure 3.2: Flowchart of the methodology for reliability assessment of ECBP connections designed as per current and prospective approaches.

3.2.1 Generation of representative design cases

The design condition for ECBP connections is defined by a combination of moment (M) and axial force (P); shear is not considered in this dissertation and is assumed to be transferred independently, e.g., through a shear key (see Gomez et al. 2011). To ensure realism in these P-M load pairs, these are not arbitrarily generated, but derived from four archetype steel moment frames (each consisting of four stories and three bays). These designs, based on ASCE 7-05 (ASCE 2006) and AISC 341-05 (AISC 2005), are selected from an archetype set of special steel moment frames developed by the National Earthquake Hazards Reduction Program (NEHRP 2010); only key details are provided here. Table 3.1 summarizes the member properties, whereas Figure 3.3 illustrates the dimensions and floorplans. The key differences between the frames are the level of seismicity for which they are designed (also indicated in Table 3.1, in accordance with Seismic Design Category, SDC, i.e., SDC-D_{max} or SDC-D_{min}) and the method used to design them (Response Spectrum Analysis, RSA; or the Equivalent Lateral Force, ELF). Four-story frames are selected for the representative load cases, because taller frames usually warrant embedded base connections (e.g., see Grilli et al. 2017), whereas 1-2 story frames often assume ECBP connections to be pinned (e.g., see Zareian and Kanvinde 2013).

Table 3.1: Member sizes for 4-story archetype frames selected to generate *P*-*M* pairs for ECBP connection design

Story	RSA SDC-D$_{\text{max}}$ frame			RSA SDC-D$_{\text{min}}$ frame			ELF SDC-D$_{\text{max}}$ frame			ELF SDC-D$_{\text{min}}$ frame		
	Beam	Exterior column	Interior column	Beam	Exterior column	Interior column	Beam	Exterior column	Interior column	Beam	Exterior column	Interior column
1	W21×73	W24×103	W24×103	W16×57	W14×74	W14×82	W24×103	W24×103	W24×131	W18×71	W18×86	W18×97
2	W21×73	W24×103	W24×103	W18×60	W14×74	W14×82	W24×103	W24×103	W24×131	W18×86	W18×86	W18×97
3	W21×57	W24×62	W24×62	W18×60	W14×48	W14×74	W24×76	W24×76	W24×84	W18×71	W18×65	W18×86
4	W21×57	W24×62	W24×62	W16×57	W14×48	W14×74	W24×76	W24×76	W24×84	W18×71	W18×65	W18×86

Note: RSA = Response Spectrum Analysis; ELF = Equivalent Lateral Force; SDC = Seismic Design Category.

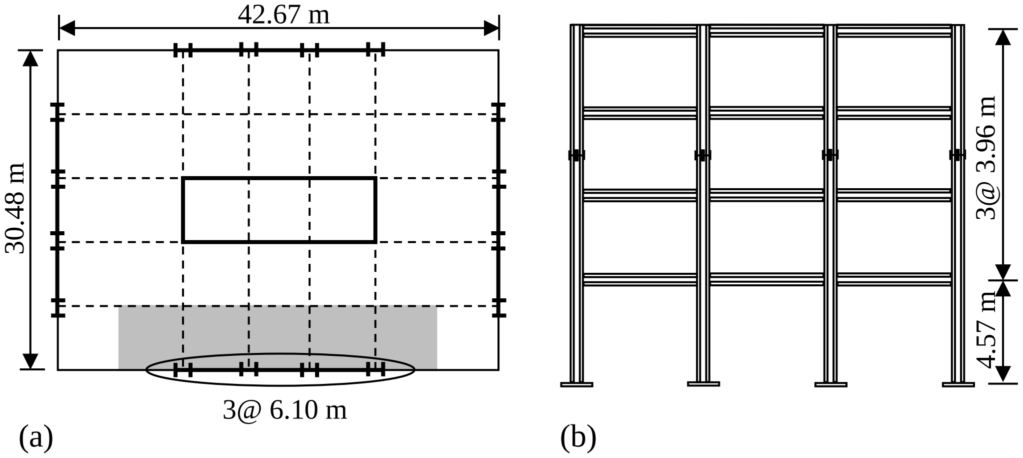

Figure 3.3: Schematic illustration of 4-story archetype frames: (a) plan configuration; and (b) elevation view.

For each frame, Dead (*D*), Live (*L*), and Earthquake (*E*) loads are determined from the applicable code used in the frame design, i.e., ASCE 7-05 (ASCE 2006). Wind (*W*) load was not considered in the original frame design (because the seismic load combinations govern the design for the considered locations) and is determined as per ASCE 7-16 (ASCE 2016). Corresponding *P* and *M* values at each of the column base locations in each building are recovered, and subsequently used to generate *P-M* pairs based on the load combinations indicated in Table 3.2. These load combinations include those prescribed by ASCE 7-16, as well as others that are informed by recent research and other standard practices. For example, Torres-Rodas et al. (2018) indicate that the minimum (rather than maximum) compressive axial force in the column may control the design of some ECBP connections, because lower compression increases tension in the rods. The load factor $-\Omega_0 E$ (in which Ω_0 represents the overstrength seismic load) reflects the overturning effect that minimizes axial compression. The factor $1.1R_yM_p$ in some of the seismic load cases reflects a capacity design [AISC 341-16 (AISC 2016b)], which is often specified in high-seismic zones to induce a plastic hinge in the attached column, rather than in the connection. Referring to Table 3.2, the exterior and interior base connections within each frame are designed separately. This results in the generation of five *P-M* pairs for which each ECBP connection must be designed: two pairs of seismic and two pairs of wind load combinations, considering maximum or minimum *P* associated with its *M*, in addition to a *P-M* pair derived from the gravity load combination.

Table 3.2: Representative *P-M* matrix for ECBP connection design

Design case no.	Frame	Base column	Site location[a]	Design load combination[b]		Base plate dimension	
				P	*M*	*N* (mm)	*B* (mm)
1	RSA SDC-D$_{max}$	Exterior (W24×103)	LA	$1.2D + 0.5L - \Omega_0E$	$1.1R_yM_p$	965	558
2				$1.2D + 0.5L + \Omega_0E$	$1.1R_yM_p$		
3				$1.2D + 0.5L - W$	$1.2D + 0.5L - W$		
4				$1.2D + 0.5L + W$	$1.2D + 0.5L + W$		
5				$1.2D + 1.6L$	$1.2D + 1.6L$		
6 – 9			Sac	Same to cases 1 – 4[c]	Same to cases 1 – 4[c]		
10 – 14		Interior (W24×103)	LA[d]	Same to cases 1 – 5	Same to cases 1 – 5	965	558
15 – 19	RSA SDC-D$_{min}$	Exterior (W14×74)	LA	Same to cases 1 – 14	Same to cases 1 – 14	711	610
20 – 23			Sac				
24 – 28		Interior (W14×82)	LA			711	610
29 – 33	ELF SDC-D$_{max}$	Exterior (W24×103)	LA	Same to cases 1 – 14	Same to cases 1 – 14	965	558
34 – 37			Sac				
38 – 42		Interior (W24×131)	LA			965	660
43 – 47	ELF SDC-D$_{min}$	Exterior (W18×86)	LA	Same to cases 1 – 14	Same to cases 1 – 14	813	610
48 – 51			Sac				
52 – 56		Interior (W18×97)	LA			813	610
57 (SEAOC)[e]	–	W14×211	–	$(0.9\text{-}0.2S_{DS})D + \Omega_0E$[e]	$(0.9\text{-}0.2S_{DS})D + \Omega_0E$[e]	813	711
58 (DG1)[f]	–	W12×96	–	$1.2D + 1.6L$	$1.2D + 1.6L$	483	483
59 (DG1)[f]	–		–			508	508

[a] Two locations in California are selected to reflect different design seismic hazard levels: (1) LA = Los Angeles (high seismicity); (2) Sac = Sacramento (medium seismicity).

[b] The code specified *D*, *L*, *W*, and *E* loads are obtained from linear elastic analyses of archetype frames modeled in SAP2000.

[c] The *P-M* pairs determined from gravity load combination for same base column at two locations are identical, therefore, only case 5 is considered.

[d] For interior column base, the seismic and wind loadings at two sites are similar, therefore, only the relatively larger values achieved from LA (owing high seismic hazard condition and higher basic wind speed) are considered to develop design cases.

[e] This case is employed from the design manual of Structural Engineers Association of California (SEAOC). This design example adopts different governing (seismic) load combinations, where, S_{DS} (= 1) is the assumed design (5% damped) spectral response acceleration parameter at short periods.

[f] These two cases are employed from the DG1 – case 58 is designed for low-eccentricity condition, while case 59 is designed for high-eccentricity condition.

Once the *P*-*M* pairs are generated as per the preceding description, the ECBP connections may be designed as per any approach (e.g., the DG1 approach or the prospective approaches) with the following additional information and material specifications that are representative of standard practice: (1) nominal concrete compressive strength f_c' = 27.58 MPa (4 ksi), and f_{grout} = 58.61 MPa (8.5 ksi); (2) concrete confinement factor (i.e., $\sqrt{A_2/A_1}$) assumed to be equal to its maximum value of 2.0; (3) ASTM A992 ($F_{y,col}$ = 345 MPa; ASTM 2020) steel used for all the beams and columns; (4) base plate material specified as A572 (Grade 50, $F_{y,pl}$ = 345 MPa; ASTM 2018a); (5) anchor rod material selected from two available grades of ASTM F1554 (ASTM 2018b) steel, i.e., Grade 55 (F_u = 517 MPa), Grade 105 (F_u = 862 MPa); (5) a minimum of four anchor rods (with diameters d_{rod} in the range of 19.05–63.5 mm) provided as per Occupational Safety and Health Administration requirements (OSHA 2001), and 76.2 mm (3 in.) edge distances (g) used for all anchor holes following standard practice; (6) base plate thicknesses (t_p) varied in 3.18 mm (1/8 in.) increments up to 31.75-mm (1.25-in) thickness and in 6.35-mm (0.25-in.) above this; and (7) in-plane dimensions of base plate (N and B) varied in 50.8-mm (2-in.) increments, and assumed to be identical for different design approaches. In addition, three examples available in the design manuals [i.e., two from DG1 and one from the design manual of Structural Engineers Association of California, SEAOC (2015)] are also analyzed in this dissertation, because these represent the only published guidance for ECBP connection design. Note that the base plate material (A36, $F_{y,pl}$ = 248 MPa; ASTM 2019a), anchor rod material (ASTM F1554 Grade 36, F_u = 400 MPa) used in these DG1 examples are representative of erstwhile construction practice, and are different from those used in this dissertation. The details of all the 59 *P*-*M* cases (for design) are further summarized in Table 3.2.

3.2.2 Characterization of uncertainty

Using the preceding considerations, and the appropriate set of design checks (DG1 or the ones proposed later in this chapter), ECBP connections may be designed. This results in the selection of the following design variables: (1) geometric parameters: overall depth (d), flange width (b_f), flange thickness (t_f) and web thickness (t_w) of base column section (W-shape), length (N), width (B) and thickness (t_p) of base plate, diameter (d_{rod}) of anchor rods, and edge distance (g) of anchor holes; and (2) material parameters: concrete compressive strength (f_c'), grout strength (f_{grout}), yield strength of base column ($F_{y,col}$) and base plate ($F_{y,pl}$) steels, as well as the tensile (ultimate) strength of anchor rods (F_u). Once this has been accomplished, the reliability assessment of each designed ECBP connection requires the characterization of uncertainty arising from four sources: (1) geometry of each component; (2) material properties; (3) applied loads on the connection; and (4) mechanical models used to characterize the demand and capacity of each component. Table 3.3 summarizes the uncertainties used for Monte Carlo sampling (discussed later). These are represented as RVs with statistical distributions that reflect the bias coefficient (i.e., the ratio between the mean value of each RV to its nominal value as specified in the design cases mentioned previously), and the coefficient of variation (CoV, defined as the ratio between the standard deviation of each RV to its mean value). All these RVs are considered statistically independent. However, it is recognized that correlations could exist among different RVs, for instance, between model-related RVs and RVs from the rest three uncertainty sources. Because the mechanical models used in this dissertation (discussed subsequently) may be less accurate (i.e., resulting in higher uncertainties) for lower eccentricity cases (Gomez et al. 2010; Kanvinde et al. 2013), and the eccentricity determination incorporates geometry-, material-, and load-related RVs (see Section 2.4.1 for details).

3.2.2.1 Component geometry

Uncertainty in component geometry is attributable to the construction or fabrication processes, tolerances, and the resulting quality (Nowak and Szerszen 2003). The dimensional statistics of the W-shape column sections are collected from Schmidt and Bartlett (2002); these include the overall depth (d), flange width (b_f), flange thickness (t_f), and web thickness (t_w). Note that these are relevant for calculating $1.1R_yM_p$ (for capacity design) as well as for determining edge distances/cantilever lengths for plate flexure limit states. According to Aviram et al. (2010), the standard deviations of base plate dimensions (i.e., length N, width B, and thickness t_p) and anchor rod diameter (d_{rod}) are established based on their tolerances specified in ASTM A6-19 (ASTM 2019b) and ASTM F1554-18 (ASTM 2018b), respectively. The tolerance (standard deviation) of edge distance (g) is defined as per AISC 303-16 (AISC 2016c). The bias

Table 3.3: Summary of RVs for reliability analysis of ECBP connections

Category	Variable	Bias	CoV (%)	Distribution
Geometry	Overall depth of base column section, d	0.999	0.2	Normal
	Flange width of base column section, b_f	0.998	0.4	Normal
	Flange thickness of base column section, t_f	1.04	2.5	Normal
	Web thickness of base column section, t_w	1.04	2.5	Normal
	Base plate length, N	1.0	2.5	Normal
	Base plate width, B	1.0	4	Normal
	Base plate thickness, t_p	1.0	3	Normal
	Anchor rod diameter, d_{rod}	1.0	8.5	Normal
	Edge distance, g	1.0	5	Normal
Material	Concrete compressive strength, f_c’	1.235	14.5	Normal
	Grout compressive strength, f_{grout}	1.0	13	Normal
	Ratio of expected to specified minimum yield strength of W-shape column steel (ASTM A992), R_y (nominal = 1.1)	1.0	5	Normal
	Yield strength of base plate steel, $F_{y,pl}$			
	ASTM A36	1.39	7	Normal
	ASTM A572 Grade 50	1.16	7	Normal
	Tensile (ultimate) strength of anchor rod steel, F_u			
	ASTM F1554 Grade 36	1.19	16	Lognormal
	ASTM F1554 Grade 55	1.13	12	Lognormal
	ASTM F1554 Grade 105	1.1	9	Lognormal
Load	Dead load, D	1.05	10	Normal
	Live load, L	1.0	25	Gumbel
	Wind load, W	0.78	37	Gumbel
	Earthquake load, E	1.0	60	Lognormal
Model	Error in characterization of concrete bearing stress, $f_{\text{concrete}}^{\text{test}} / f_{\text{concrete}}^{\text{Eq.(2.22)}}$	1.07	16	Normal
	Error in characterization of flexural demand of base plate on the compression side, $M_{pl,comp}^{\text{true}} / M_{pl,comp}^{\text{model}}$			
	DG1 model	0.88	19	Normal
	DG1* and CF models	0.74	20	Normal
	Error in characterization of flexural demand of base plate on the tension side, $M_{pl,ten}^{\text{true}} / M_{pl,ten}^{\text{model}}$			
	DG1 model	0.99	12	Normal
	DG1* and CF models	1.1	14	Normal
	Error in characterization of tension demand in anchor rods, $T_{\text{rods}}^{\text{true}} / T_{\text{rods}}^{\text{model}}$			
	DG1 model	0.99	12	Normal
	DG1* and CF models	1.1	14	Normal

factors are assumed equal to 1.0 to represent the average quality of construction or fabrication. Moreover, the normal distribution is assumed for these dimensional RVs with a relatively small CoV (i.e., < 10%), as expected for geometry-related RVs (Aviram et al. 2010).

3.2.2.2 Material properties

The statistical properties of concrete compression strength for nominal f_c' = 27.58 MPa (4 ksi) are comprehensively documented in Nowak and Szerszen (2003), in which 116 concrete samples obtained from different concrete industrial sources in the US were assessed. According to testing by Gomez (2010), the compressive strength of grout (f_{grout}) is 58.61 MPa with a CoV of 13%. Statistics of structural steel used for the column and base plate were assembled from a detailed survey by Liu et al. (2007). These properties include the yield strength ($F_{y,pl}$) of base plate materials (both ASTM A572 Grade 50 and ASTM A36 steels), and the yield stress ($F_{y,col}$) of the A992 steel used for the base columns. Statistical distributions for the anchor rod tensile strength (F_u) of ASTM F1554 steels are characterized based on the approach of Aviram et al. (2010) and the tolerances given in ASTM F1554-18 (ASTM 2018b). Table 3.3 summarizes the distributions as well as the statistical parameters for all material properties.

3.2.2.3 Applied loads

Combinations of Dead (D), Live (L), Earthquake (E), and Wind (W) loads are considered to determine the axial (P) and flexural (M) forces acting on the ECBP connections. The RV describing the dead load is usually assumed as normally distributed and Ellingwood et al. (1980) suggests a bias of 1.05 and a CoV of 10%. For the RVs to describe live load and wind load, a Gumbel-type distribution is selected (Ellingwood et al. 1980), and their bias and CoV values are summarized in Table 3.3. For the earthquake load, a lognormal distribution with a bias of 1.0 is assumed, based on the calibration by Fayaz and Zareian (2019) using linear time history analysis. The assumed bias is also close to the value suggested by Ellingwood et al. (1980) for a site in Los Angeles, California. It is also worth noting that Torres-Rodas et al. (2018) performed nonlinear time history analyses to characterize demands in ECBP connections in a 4-story steel moment frame (similar to one of the selected frames in this dissertation). Their findings indicate bias values of 1.17 and 1.02 for the determination of axial force (for interior and exterior column bases, respectively) subjected to the seismic load combination (i.e., $P = 1.2D + 0.5L + \Omega_0 E$). A CoV of 60% is arbitrarily assumed here for the distribution of the maximum earthquake load effects over a service period of 50 years. It is worth highlighting that an explicit/advanced calibration of the earthquake-induced demands (and their distributions) for each case-study connection and the consequent seismic reliability assessment would require performing nonlinear time history analyses using hazard-consistent ground motions (for a given target site) and integrating the obtained structural demands with a site-specific hazard curve, as done for instance in Torres-Rodas et al. (2020) [or similarly in Fayaz and Zareian (2019) by using linear time history analysis]. This is outside the scope of this dissertation. The simplified approach used here is deemed appropriate to compare and discuss different design strategies for ECBP connection as proposed in this chapter. Note that for the cases that involve capacity-design for calculation of the moment (i.e., $M = 1.1R_y M_p$, nominally, where $M_p = F_{y,col} Z_x$ where Z_x is the plastic modulus of the section), the uncertainty in geometry and material properties (outlined in the previous subsections) is used to simulate uncertainty in $1.1R_y F_{y,col} Z_x$. Referring to Table 3.3, the bias factor as well as the distribution for $F_{y,col}$ include the R_y effect (i.e., the difference between specified and true yield stress), based on Liu et al. (2007).

3.2.2.4 Mechanical models

Model uncertainties, often known as professional uncertainties, connote the error in demand or capacity estimates determined through models or equations. In general, these may be determined by comparing the demand or capacity obtained in experimental or numerical tests with the corresponding values obtained via analytical formulations or simplified models. On the capacity side, the expressions for plate bending strength (i.e., $M_p^{\text{plate}} = F_{y,pl} \cdot t_p^2 / 4$) as well as the anchor rod strength (i.e., $T_R^{rods} = n_{\text{rods}} \cdot 0.75 \cdot F_u^{\text{rod}} \cdot A_{\text{rod}}$) are derived from basic mechanics and are considered straightforward; consequently, errors in their estimations are assumed to be negligible and not considered in this dissertation. The bearing stress of the concrete/grout ($f_{\max}$) includes the factor $0.85\sqrt{A_2/A_1}$ [to reflect the confining effect of the concrete footing; refer to Eq. (2.22)], and may be expressed in the following manner:

$$f_{\max} = \min\left(f_{\text{grout}}, \frac{f_{\text{concrete}}^{\text{test}}}{f_{\text{concrete}}^{\text{Eq.(2.22)}}} \times \left(0.85 \times f_c' \times \sqrt{\frac{A_2}{A_1}} \right) \right) \tag{3.1}$$

Expressing the bearing stress of concrete in this manner allows for the incorporation of model uncertainty through the term $f_{\text{concrete}}^{\text{test}} / f_{\text{concrete}}^{\text{Eq.(2.22)}}$ in Eq. (2.22), which may be simulated as an RV. Comparison of experimental data by Hawkins (1968), for $f_{\text{concrete}}^{\text{test}}$, to the solutions obtained by Eq. (2.22) ($f_{\text{concrete}}^{\text{Eq.(2.22)}}$) is used to determine the parameters for the distribution of error in bearing stress calculation (see Table 3.3). On the demand side, the primary modeling uncertainties are in the estimations of bending moments on the compression side and tension side of base plate (denoted as $M_{pl,comp}$ and $M_{pl,ten}$, respectively), as well as tension forces in the anchor rods (T_{rods}). These uncertainties arise from the simplifying assumptions of the strength characterization method itself (i.e., the rectangular stress block, and arising internal force distribution). For the tensile force demands in the anchor rods, experimental data from Gomez et al. (2010) as well as Kanvinde et al. (2015) are informative because these feature direct measurement of anchor rod forces through strain gauges or load cells. These findings are supplemented by continuum finite element (CFE) simulations by Kanvinde et al. (2013). Based on these results, the model uncertainty in the estimated anchor rod forces may be represented through an RV ($T_{\text{rods}}^{\text{true}} / T_{\text{rods}}^{\text{model}}$; see Table 3.3):

$$T_{\text{rods}} = \left(\frac{T_{\text{rods}}^{\text{true}}}{T_{\text{rods}}^{\text{model}}} \right) \cdot T_{\text{rods}}^{\text{model}} \tag{3.2}$$

The two other quantities, i.e., $M_{pl,comp}$ and $M_{pl,ten}$, are challenging to measure experimentally. consequently, their CFE-based estimates [from Kanvinde et al. (2013)] are used to characterize model uncertainty in them through the RVs, $M_{pl,comp}^{\text{true}} / M_{pl,comp}^{\text{model}}$ and $M_{pl,ten}^{\text{true}} / M_{pl,ten}^{\text{model}}$ (whose distributions are also summarized in Table 3.3). These may be expressed as:

$$M_{pl,comp} = \left(\frac{M_{pl,comp}^{\text{true}}}{M_{pl,comp}^{\text{model}}} \right) \cdot M_{pl,comp}^{\text{model}} \tag{3.3}$$

$$M_{pl,ten} = \left(\frac{M_{pl,ten}^{\text{true}}}{M_{pl,ten}^{\text{model}}} \right) \cdot M_{pl,ten}^{\text{model}} \tag{3.4}$$

Note that in the preceding equations, the superscript “model” is used to denote a model generically and may be used for the DG1 model or those suggested herein; these result in distinct distributions, each determined by comparing estimates from the corresponding model to the CFE or test results (indicated by the superscript “true”).

3.2.3 Formulation of limit states

As discussed in the previous Section 2.4.1, four failure modes of ECBP connections subjected to combined flexural and axial loadings have been identified: (1) bearing failure in the footing (BF); (2) flexural yielding of base plate on the compression side (PC); (3) flexural yielding of base plate on the tension side (PT); and (4) anchor rod tensile failure (AT). For each of these, conditions that lead to failure may be expressed as limit state functions (G_{FM}) defined as the difference between the capacity (C_{FM}) and counterpart demand (D_{FM}), and the subscript “FM” represents a possible failure mode (i.e., BF, PC, PT, AT):

$$G_{\mathrm{FM}} = C_{\mathrm{FM}} - D_{\mathrm{FM}} \tag{3.5}$$

Failure of each component occurs when demand exceeds capacity, i.e., $G_{\mathrm{FM}} \leq 0$. Following this, the limit state functions of three of the four individual failure modes (i.e., PC, PT, and AT) may be formulated as:

$$G_{\mathrm{PC}} = C_{\mathrm{PC}} - D_{\mathrm{PC}} = M_p^{\mathrm{plate}} - M_{pl,comp} \tag{3.6}$$

$$G_{\mathrm{PT}} = C_{\mathrm{PT}} - D_{\mathrm{PT}} = M_p^{\mathrm{plate}} - M_{pl,ten} \tag{3.7}$$

$$G_{\mathrm{AT}} = C_{\mathrm{AT}} - D_{\mathrm{AT}} = T_R^{\mathrm{rods}} - T_{\mathrm{rods}} \tag{3.8}$$

All the terms in Eqs. (3.6)–(3.8) are discussed previously, in Section 3.2.2.4. For the BF failure mode, the limit state function cannot be formulated in a single equation because failure is assumed to occur when the bearing stress f and bearing width Y required to resist the applied P-M combination, violates either of the following conditions:

$$f < f_{\max} \tag{3.9}$$

$$Y < N - g \tag{3.10}$$

The former [Eq. (3.9)] enforces the condition that the maximum stress is limited by the bearing capacity of the grout/concrete footing, whereas the latter [Eq. (3.10)] disallows the unphysical development of a zone of compression in the foundation under the tensile anchor rods.

3.2.4 Monte Carlo sampling and reliability assessment

For each of the design cases, plain Monte Carlo sampling is used to simulate the demands (D_{FM}) and capacities (C_{FM}) of each failure mode described previously. The Monte Carlo sampling is conducted through a MATLAB (version R2017a) code developed by the authors, and used to estimate the probability of the limit state functions (G_{FM}, as formulated previously) being non-positive, i.e., the probability of failure (P_f):

$$P_f = \Pr\left(G_{\mathrm{FM}} \le 0\right) = \Pr\left(C_{\mathrm{FM}} - D_{\mathrm{FM}} \le 0\right) \tag{3.11}$$

A total of 10^8 samples (of the RV sets with statistics listed in Table 3.3) are randomly generated, and the P_f of each failure mode is estimated through a one-by-one check of G_{FM} in each simulation:

$$P_f = \frac{\text{Number of } G_{\mathrm{FM}} \le 0}{\text{Total Number of Samples}\left(=10^8\right)} \tag{3.12}$$

Then, a commonly-used measure of reliability, known as the reliability index β (Cornell 1969), is adopted to evaluate the results. If G_{FM} follows a normal distribution, β is related to P_f via the standard normal cumulative distribution function $\Phi(\cdot)$:

$$P_f = \Phi\left(-\beta\right) \Leftrightarrow \beta = -\Phi^{-1}\left(P_f\right) \tag{3.13}$$

Even though G_{FM} does not have a normal distribution, it is common practice to convert the failure probabilities to β through Eq. (3.13) as an indicator of reliability; the approximation associated with this conversion is usually very low (Iervolino and Galasso 2012). For each simulation, a total of 10^8 samples are used; this sample size of Monte Carlo simulation is able to achieve stable estimates of a $P_f = 3.17 \times 10^{-5}$

(corresponding to a target reliability index, $\beta_T = 4.0$) with a CoV of 2% or less (Nowak and Collins 2012).

Acceptable or target β_T values for a given component usually depend on the consequences of component failure on system performance, because the ultimate goal is to limit the annual probability of system collapse to a tolerable level (Victorsson 2011). However, tuning the probability of failure of each component within a system to achieve a target annual probability of system failure is typically infeasible due to the multitude of variables and uncertainties involved in the process. As a result, the load and resistance factor design (LRFD) approach (also used in the DG1) sets lower target probabilities of failure for connections (whose failure is assumed to be catastrophic) compared to members. Specifically, the target probability of connection failure is set 2.5 orders of magnitude lower than member failure. This is reflected in the target reliability indices of 4.5 and 3.0 for connections and members (under dead and live loadings), respectively (AISC 1986). Similarly, $\beta_T = 4.1$ (for dead plus live plus wind loading, i.e., wind load combination) and 3.6 (for dead plus live plus earthquake loading, i.e., seismic load combination) are recommended for connection design. Following this rationale, these target β_T values (4.5 for gravity, 4.1 for gravity and wind, and 3.6 for gravity and seismic) are adopted in this dissertation.

This reliability assessment process is first applied to the designs generated by the ECBP connections designed as per the DG1 approach; this is the topic of the next section. Based on the results of this reliability assessment, refinements to the approach are proposed, and the reliability assessment process is reapplied to connections designed with these refinements.

3.3 Reliability analysis of ECBPs designed as per current practice

The methodology discussed in the previous section is applied to analyze the structural reliability of 59 ECBP connections designed as per current practice, i.e., the DG1 method. For all these connections, a β value (reflecting the probability of failure) is computed for each of the four failure modes. These β values are represented as histograms in Figure 3.4. Specifically, Figure 3.4 shows the median β value (with error

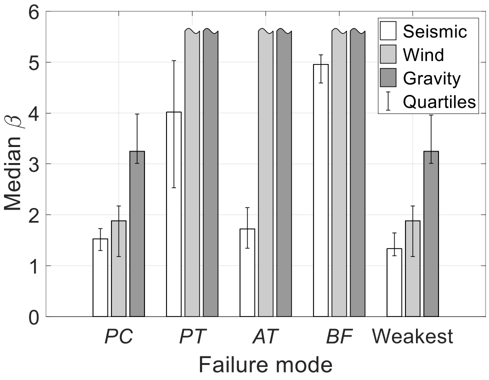

Figure 3.4: Median reliability index (β) values (with respect to different failure modes and load combinations) of ECBPs designed as per the DG1 method.

bars representing lower and upper quartiles, i.e., the 25th and 75th percentiles) for various subsets of data to examine reliability with respect to different failure modes and under different loadings. The histograms in Figure 3.4 are grouped into sets, each corresponding to a failure mode (i.e., BF, PC, PT, and AT). Within each set, the three bars correspond to different loading combinations, i.e., gravity only, gravity plus wind loading, and gravity plus earthquake loading. Referring to Figure 3.4, the following observations may be made:

- The median β value for the PC limit state (i.e., flexural yielding of the plate on the compression side) is the lowest compared to the other failure modes, indicating the highest probability of failure. The range of these β values (1.1–2.3, with a median of 1.5) corresponding to the seismic load combinations (designed mainly for high-eccentricity conditions) is unacceptable relative to conventional expectations of reliability for connections (that require a β value of 3.6), as outlined earlier. This nonconservatism is not surprising, considering the use of the ϕ_{bearing}-factor (discussed earlier) within the bearing stress block, which artificially decreases the flexural demand on the base plate on the compression side of the connection. While this is problematic from a reliability standpoint, experimental research by Gomez et al. (2010) and Kanvinde et al. (2015) indicates that exceeding this limit state (i.e., base plate yielding on the compression side) may not result in loss of strength, owing to the high ductility associated with this mechanism. A total of 15 experiments in these studies indicate that the connection continues to gain strength even after the PC limit state, reaching its capacity only when a limit state on the tension side (i.e., either PT or AT limit state) is also attained. Based on this information, the Seismic Provisions [AISC 341-16 (AISC 2016b), Commentary] suggest that the ultimate strength of the ECBP connection be calculated upon attainment of yielding on both the tension and compression sides of the base plate.

- For the PT and BF limit states, satisfactory reliability (median $\beta > 4.0$) is achieved across all loading cases. In fact, in many of these cases, the histograms are shown as incomplete because no failure was observed in the 10^8 RV realizations for the Monte Carlo sampling.
- For the AT limit state, the reliability for the design cases corresponding to seismic load is unacceptable (median β value of 1.7), while it is acceptable for the other loading cases.
- Figure 3.4 also indicates a reliability index corresponding to connection failure, which corresponds to the weakest failure mode (i.e., the lowest β value obtained among the BF, PC, PT, and AT limit states) in each of the design cases; this is shown as a separate group of histograms. Referring to these, the β values for most of the load cases (46 out of 59 cases) are identical to those for the PC limit states. A closer examination of the data indicates that for these design cases, the PC limit state has the lowest reliability, while the AT and PT limit states (corresponding to seismic design cases) are observed as the weakest failure mode for the 11 and two exceptions, respectively.
- For all limit states, it is noted that the β value associated with the seismic load cases is significantly lower than that associated with the other (gravity and wind) load cases, and also unacceptable relative to the values outlined previously for PC and AT limit states (with median β of 1.5 and 1.7, respectively).

In summary, the reliabilities attained for ECBP connections designed as per the DG1 approach are inconsistent across various limit states as well as loadings. For a few of these limit states and loading cases, the reliability estimates are clearly unacceptable.

3.4 Alternative design approaches

The above discussion motivates alternative design approaches that mitigate the problems of the DG1 approach. It is evident that the use of the ϕ_{bearing}-factor in the determination of plate bending moments and anchor rod forces is problematic from both a mechanistic and a reliability standpoint. Further, it is noted that PC limit state is the most critical in terms of reliability, although exceedance of this limit state does not result in overall failure of the connection, as suggested by AISC 341-16 (AISC 2016b). Following these observations, two alternative design approaches are considered:

- The first approach (termed DG1*) is identical to the DG1 approach, except for the omission of the ϕ_{bearing}-factor in the determination of the anchor rod tension as well as the plate flexural stresses. All limit states, i.e., BF, PC, PT, and AT, are checked in design.
- The second approach (termed CF, i.e., connection failure) is similar to DG1*, i.e., the ϕ_{bearing}-factor is not considered. However, only the PT and AT limit states are checked, assuming that overall failure of the connection does not occur until at least one of these is attained.

In each of these approaches, the plan dimensions of the base plate are designed as per DG1, i.e., using ϕ_{bearing} = 0.65 to check the BF limit state (Table 3.2), as discussed earlier; therefore, the results of the BF check are identical to those in the previous sections. It is emphasized here that the use of ϕ_{bearing} = 0.65 is problematic only when the bearing stress is being considered a demand or loading on the remainder of the base connection. Using both approaches, ECBP connections are redesigned for each of the loading cases summarized previously in Table 3.2 (and also used for generation of designs for the reliability analysis of the DG1 approach). Within each of these approaches, a range of trial ϕ-factors are used to size both the plate (using ϕ_{plate} = 0.9, 0.8, 0.7, 0.6, 0.5, and 0.4) and the rods (using ϕ_{rod} = 0.75, 0.65, 0.55, 0.45, and 0.35). This enables effective selection of ϕ-factors that provide adequate safety for all limit states and loading scenarios. The resulting design configurations (i.e., base plate and anchor rod sizes) may then be subjected to reliability analysis in a manner similar to that conducted for the DG1 approach. Specifically, the Monte Carlo sampling follows exactly the same procedure as earlier (for DG1), with uncertainties characterized through the RVs and their distributions summarized in Table 3.3. The key results of these simulations are the probabilities of failure, expressed in terms of equivalent β factors for various limit states and design cases.

Figures 3.5(a)–(e) plot the β values versus the corresponding ϕ-factors for the DG1* approach. The clusters of β for each value of ϕ-factor represent the different ECBP designs that all satisfy the design checks; the graph line connects the median β

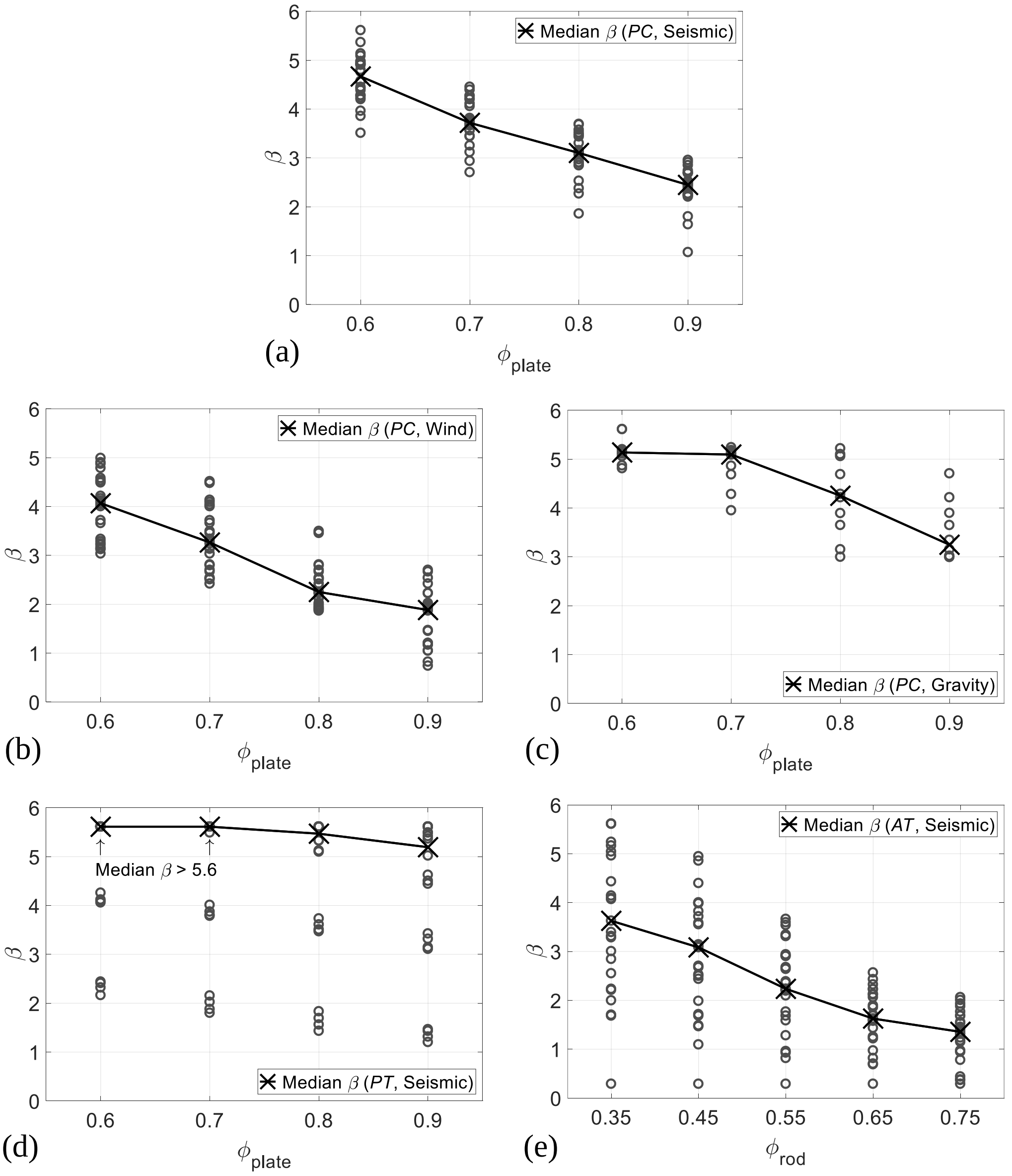

Figure 3.5: Reliability index (β) plotted against trail ϕ-factors for the DG1* approach: β versus ϕ_{plate} for PC check considering (a) seismic, (b) wind, and (c) gravity load cases, respectively; (d) β versus ϕ_{plate} for PT check; and (e) β versus ϕ_{rod} for AT check, both only considering seismic load cases.

values of these clusters. Referring to these figures, the BF limit state is not included in these graphs because only a single ϕ_{bearing}-factor (i.e., 0.65) is used for sizing the footprint (i.e., plan dimensions) of the base plate. Further, the tension side limit states (PT and AT) are not included for the gravity and wind loading cases (once designed for low-eccentricity conditions), because for these cases, the demands are much lower relative to capacities for all selected values of ϕ_{plate} and ϕ_{rod} (resulting in β values greater than 4.9 in all cases), thereby making their selection inconsequential. Referring to Figures 3.5(a)–(e) for the remaining limit states, the following observations may be made:

- For the base plate, the PC limit state controls (in a vast majority of cases) over the PT limit state for the seismic loading cases, and is the only possible plate limit state for wind and gravity (that are designed for low-eccentricity conditions). Thus, focusing on the PC limit states across the three load cases (seismic, gravity, and wind) provides insights into suitable ϕ_{plate}-factors. Specifically, it is noted that: (1) the current estimate of $\phi_{\text{plate}} = 0.9$ used in DG1 results in unacceptable median β values in the range of 1.9–3.2 for the three load cases, and (2) the value of $\phi_{\text{plate}} = 0.6$ results in acceptable (median) β values, in the range of 4.1–5.1.
- For the AT limit state (which is shown only for the seismic load cases), a similar trend is observed, such that the current value (i.e., $\phi_{\text{rod}} = 0.75$) results in β values in the range of 0.3–2.1 (unacceptable), whereas a value of $\phi_{\text{rod}} = 0.35$ results in more acceptable values of β (with median = 3.6).

Because the suitable ϕ values for both the base plate and the anchor rods are significantly lower than those commonly used, this observation bears some explanation. Specifically, the current values of ϕ_{plate} and ϕ_{rod} are directly adopted from the AISC Specification (AISC 2016a) for plate bending and axial tension in threaded rods. In turn, these values are calibrated based on reliability analysis in which demands (i.e., dead and/or live loads) with their associated distributions, are applied directly to the components. In contrast, for the ECBP connections, the demands (with similar distributions) are applied at the connection level rather than the component level. This distinction is important, because the component forces (e.g., $M_{pl,comp}$, $M_{pl,ten}$, or T_{rods})

are related to the connection demands (i.e., *P*-*M* pairs) in a highly nonlinear manner. Thus, the uncertainties in the component demands are greatly amplified relative to those at the connection level. A lower ϕ-factor (applied to the capacity) is necessary to compensate for this effect, and produce an acceptable level of safety. Based on observations of Figures 3.5(a)–(e), $\phi_{\text{plate}} = 0.6$ and $\phi_{\text{rod}} = 0.35$ are recommended as prospective ϕ-factors for use with the DG1* approach. Figure 3.6 shows histograms similar to those presented for the DG1 reliability analysis for these ϕ-factors as applied to the DG1* method; these histograms illustrate expected β values for all limit states and load combinations. As expected, the histograms suggest that using the DG1* approach with these ϕ-factors results in acceptable values of reliability across all limit states, and for all loadings.

Figures 3.7(a)–(b) show the β versus ϕ plots for the CF approach (i.e., for connections designed only based on the PT and AT limit states). The PT and AT limit states are relevant only for the seismic cases, because only these cases result in the high-eccentricity condition. The observations from Figures 3.7(a)–(b) are qualitatively similar to those noted previously for the DG1* approach. Specifically, the current values of $\phi_{\text{plate}} = 0.9$, and $\phi_{\text{rod}} = 0.75$ result in grossly unacceptable levels of reliability for both the PT and AT limit states. Based on the trends shown in these figures, the values of $\phi_{\text{plate}} = 0.4$ and $\phi_{\text{rod}} = 0.35$ are suggested for use with the CF approach. Figure 3.8 shows the resulting β values for the three limit states (note that the PC limit state is omitted from the CF analysis). Referring to the figure, it is evident that these ϕ-factors, used within the CF approach, result in acceptable values of β ($> \beta_T = 3.6$) across all limit states. It is interesting to observe that the $\phi_{\text{plate}} = 0.4$ required to produce

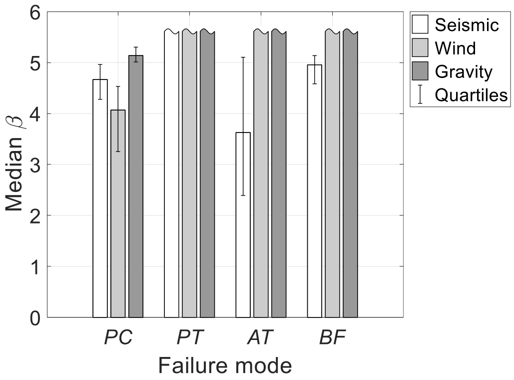

Figure 3.6: Median reliability index (β) values (with respect to different failure modes and load combinations) of ECBPs designed as per the DG1* method.

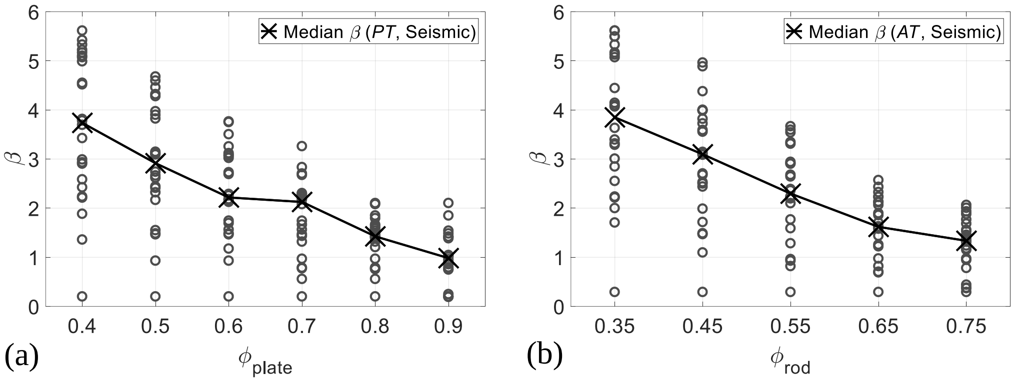

Figure 3.7: Reliability index (β) plotted against trial ϕ-factors for the CF approach: (a) β versus ϕ_{plate} for PT limit state check; and (b) β versus ϕ_{rod} for AT limit state check, both for seismic load cases.

acceptable β values for the CF approach is lower than the corresponding ϕ_{plate} (= 0.6) for the DG1* approach, suggesting that the CF approach will result in a thicker base plate. However, this is not true, because the PC limit state, which is disregarded in the CF approach (but included in the DG1* approach), in fact results in significantly thicker base plates in a large majority of cases.

To examine the implications for design more generally, Figures 3.9(a)–(f) compare the plate thickness (t_p) as well as the anchor rod sizes generated by all three methods (i.e., DG1, DG1*, and CF) for each of the design cases. As mentioned previously, the CF method is only applied to the design cases for high-eccentricity conditions (i.e., the seismic cases in this dissertation). As a result, only the design results of these high-eccentricity cases are presented in Figures 3.9(c)-(f) for the comparisons between the DG1/DG1* and CF methods. The first column of the figures

Figure 3.8: Median reliability index (β) values (with respect to different failure modes and seismic load combinations) of ECBPs designed as per the CF methods.

[i.e., Figures 3.9(a), (c), and (e)] illustrate the plate thicknesses (in all cases, ASTM A572 Grade 50 plate was specified), while the second column [Figures 3.9(b), (d), and (f)] illustrate the anchor rod areas ($A_{\text{rods,all}}$). For the latter, ASTM F1554 Grade 55 steel was used in most cases except when congestion of anchor rods necessitated the use of a higher grade (i.e., Grade 105) for reducing the number/size of rods. The figures only report the rod area ($A_{\text{rods,all}}$). Referring to these figures, the following observations may be made:

- Figures 3.9(a) and (b) compare the DG1 and DG1* approaches. The primary observation is that the DG1* approach results in thicker base plates as well larger anchor rods as compared to the DG1 approach. This is not surprising because the DG1 approach (owing to its use of the ϕ_{bearing}-factor in the equations to determine plate flexure and rod tension) unconservatively mischaracterizes the demands in these components. On average, the thickness of the plate as determined by DG1* is 1.28 times the thickness determined by DG1, whereas the rod area is 1.84 times the rod area determined by DG1 (for seismic design cases only).
- Figures 3.9(c) and (d) compare the DG1 and CF approaches. The CF approach results in similar plate thicknesses as compared to the DG1 approach; this is not surprising, because the CF approach does not consider the PC limit state that controls in a majority of the design cases. On the other hand, the CF approach results in significantly larger anchor rod areas compared to DG1. This is similar to the comparison between DG1 and DG1*, and may be attributed to: (1) the absence of the ϕ_{bearing}-factor in the CF approach, when estimating forces and moments in the anchor rods and the base plate, and (2) recalibration of the lower ϕ_{rod}-factor (= 0.35) in the CF approach to achieve acceptable reliability.
- Figures 3.9(e) and (f) compare the two prospective approaches, i.e., DG1* and CF. These result in exactly the same anchor rod sizes, because the basis for estimation of anchor rod forces (i.e., no ϕ_{bearing} in the equations) as well as ϕ_{rod} (= 0.35) are identical between the two approaches. On the other hand, the base plate thicknesses as determined by the CF approach are on average 25% lower than those determined by the DG1* approach.

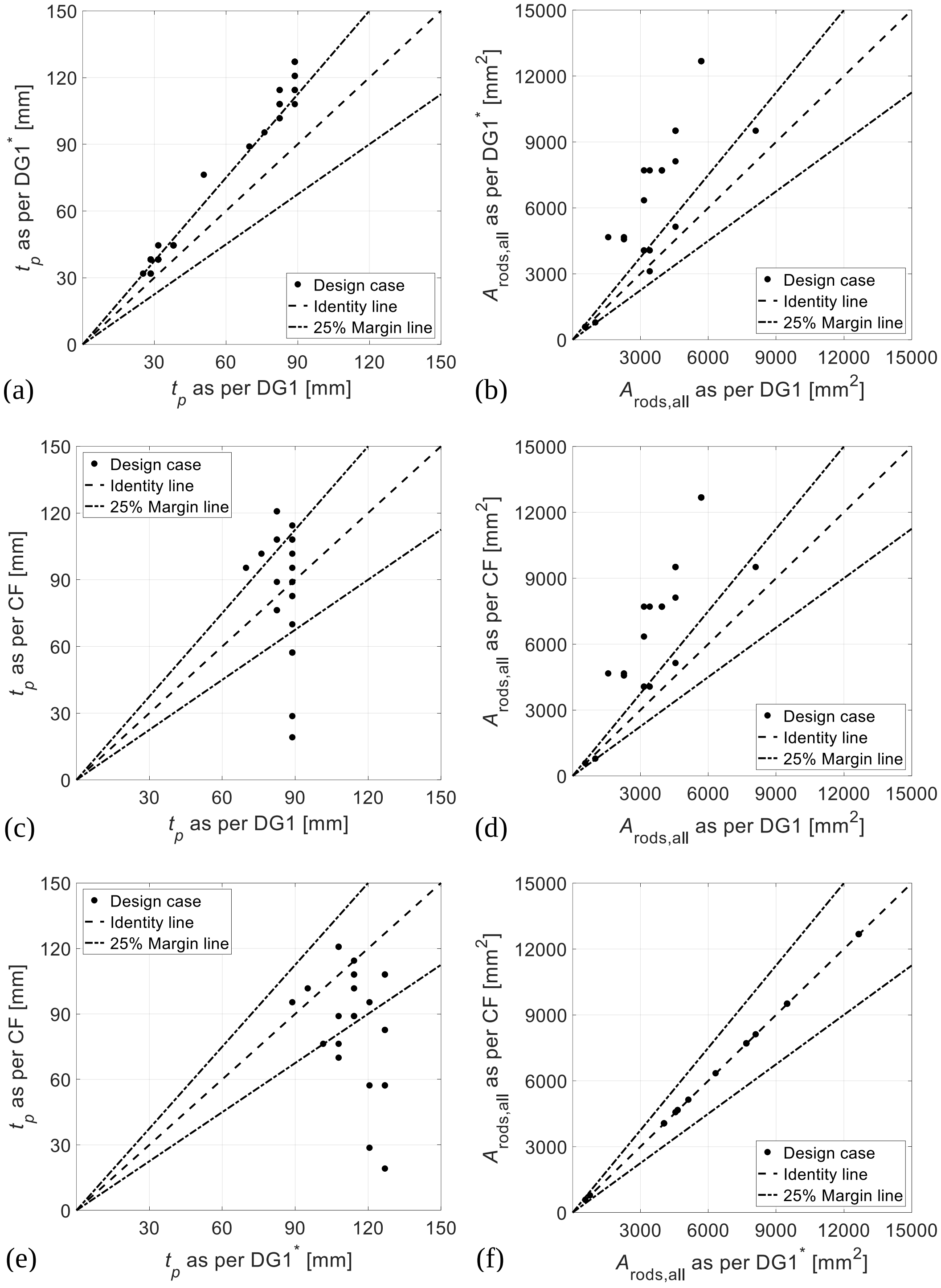

Figure 3.9: Comparisons of (a) plate thickness (t_p) and (b) total anchor rod area ($A_{\text{rods,all}}$) for all the 59 ECBP cases designed as per the DG1 and DG1* method (top panel); comparisons of (c) t_p and (d) $A_{\text{rods,all}}$ for the seismic (high-eccentricity) ECBP cases designed as per the DG1 and CF methods (middle panel); and comparisons of (e) t_p and (f) $A_{\text{rods,all}}$ for the seismic (high-eccentricity) ECBP cases designed as per the DG1* and CF methods (bottom panel).

Based on the reliability analysis outlined earlier, both prospective approaches provide acceptable and consistent levels of reliability across all limit states and loading cases, as compared to the DG1 approach, which does not. Of these, the DG1* approach is likely to increase the cost of the ECBP connections, because it requires, on average, thicker base plates as well as larger anchor rods. On the other hand, the CF approach results in thinner base plates but larger anchor rods. Nonetheless, it does admit the possibility of base plate yielding on the compression side of the connection. Suitable approaches for design may be selected or developed based on these observations.

3.5 Summary

ECBP connections are commonly constructed in SMRFs across the US and beyond. Methods to estimate the strength of these connections and design them are well-documented in scientific literature, as well as in design guidelines – primarily, the American Institute of Steel Construction's Design Guide One (DG1, from Fisher and Kloiber 2006). While mechanistic aspects of the strength models have been studied extensively, the reliability provided by ECBP connections designed as per these approaches has received relatively less attention. Motivated by this, a detailed reliability analysis of the DG1 approach is conducted. The results indicate that the DG1 approach results in unacceptable and inconsistent probabilities of failure of the connection, which is largely controlled by flexural failure of the base plate on the compression side of the connection. This is attributed to the ϕ_{bearing}-factor, which artificially reduces the flexural demands on the base plate. Further, it is noted that: (1) the probabilities of failure are inconsistent across the four limit states, and (2) the seismic load cases result in lower reliability for all limit states as compared to the gravity and wind cases. In response to these problems identified in the DG1 approach, two alternative design methods are suggested. Both eliminate the ϕ_{bearing}-factor in the bearing stress used for calculating flexural stresses in the base plate, whereas one considers overall connection failure, rather than the failure of individual components within it. Both these approaches provide adequate reliability.

While the dissertation suggests significant improvements to the current method for designing ECBP connections, it has several limitations that must be considered in its interpretation and application. First, the models used in this dissertation inherit all the limitations of the internal force distributions implied by the DG1 approach that may be inaccurate for high-eccentricity cases with relatively low flexure demands (Gomez et al. 2010; Kanvinde et al. 2013). Further, the DG1 approach is also inapplicable to ECBP connections subjected to biaxial bending or if the connection is overtopped with a slab on grade (Hanks and Richards 2019), as is sometimes the case. For biaxial bending, studies suggest using an empirical interaction equation to interpolate for angles of resultant moment that are not aligned with the major or minor axes (e.g., see Choi and Ohi 2005; Fasaee et al. 2018; Lee et al. 2008a; b). Second, the dissertation considers a limited number of SMRF configurations and these may bias the design cases (in terms of size, and configuration) relative to ECBP connections that differ significantly, e.g., those found in mezzanine columns (Kanvinde et al. 2015), or storage racks (Petrone et al. 2016). Third, the distributions of random variables to define various forms of uncertainty are based on limited data/engineering judgment (in some cases) and are considered uncorrelated. Notwithstanding these limitations, the chapter presents a critical analysis of current and prospective design approaches that may be used to more effectively design ECBP connections.

Chapter 4

Fracture Fragility Assessment of Pre-Northridge Welded Column Splices Considering Seismic Demand and Capacity Uncertainties

Adapted from **Song, B.**, Galasso, C., and Kanvinde, A. (2020). "Advancing fracture fragility assessment of pre-Northridge welded column splices." *Earthquake Engineering & Structural Dynamics*, 49(2), 132–154.

4.1 Introduction and motivations

Steel moment-resisting frames (SMRFs) are a popular load-resisting system on the West Coast of the US and in other seismically active regions. This is mainly due to their architectural versatility and ductility features. Over the last two decades, the design and detailing practice for SMRFs have undergone tremendous changes. In large part, these changes are the results of extensive experimental and analytical/numerical research studies – notably the US Federal Emergency Management Agency (FEMA)-funded SAC Steel Project (e.g., Alali et al. 1995; Anderson et al. 1995; Kaufman and Fisher 1995; Maison et al. 1996). These studies were conducted in response to brittle fractures observed in welded beam-to-column (WBC) connections in SMRFs during the 1994 M6.7 Northridge earthquake (Gupta and Krawinkler 1999). These various studies revealed that numerous factors were responsible for the observed fractures, including: (1) the use of low-toughness weld and base materials; (2) poor detailing and construction practices such as improper access holes, left-in-place backing bars, and runoff tabs that created notch conditions and prevented visual inspection; and (3) connection design factors such as inadequate participation of the web resulting in higher stresses in the flanges. As a result, recommendations from these studies [now codified in the American Institute of Steel Construction's AISC 341-16 (AISC 2016b)] mandate improved material toughness and detailing requirements for all new welded steel connections within SMRFs in addition to guidelines for the retrofit of vulnerable pre-Northridge connections [FEMA 354 (SAC Joint Venture 2000)]. In pre-Northridge frames, application of these retrofit strategies has largely been focused on WBC connections, given that: (1) fractures were observed exclusively within these connections after the Northridge earthquake; and (2) their location, adjacent to the beam plastic hinge, is particularly critical. On the other hand, a large majority of welded column splice (WCS) connections were, for the most part, not checked for fracture after the Northridge earthquake, and many have not been retrofitted. This may be attributed to the potential operational disruption and liability issues that may arise from such inspections. Nonetheless, several studies including those by researchers (e.g., Galasso et al. 2015) and practitioners (e.g., Nudel et al. 2015) indicate a very high likelihood of such fractures, such that WCS retrofit is a priority for numerous pre-Northridge buildings. Figure 4.1 illustrates the location and details of a typical pre-Northridge WCS and also shows a post-test photograph of a fractured splice. These connections are common in mid- to high-rise SMRFs due to transportation limitations on column height and to facilitate transitioning of column sizes through the height of a structure.

Referring to Figure 4.1, pre-Northridge WCS connections typically feature partial joint penetration (PJP) welds with low flange weld penetrations (effective weld throat) in the range of 40–60% of the thinner connected flange thickness, producing a crack-like flaw at the root of PJP welds. This flaw is perpendicular to the longitudinal tensile stress in the flanges when the column is under axial tension or flexure during seismic events; therefore, it is detrimental from the standpoint of fracture capacity (Stillmaker et al. 2016). Additionally, the typical weld filler materials of pre-Northridge WCS connections are characterized by Charpy V-Notch (CVN) energy values between 6.8–13.6 J (Chi et al. 2000). These CVN values are significantly lower

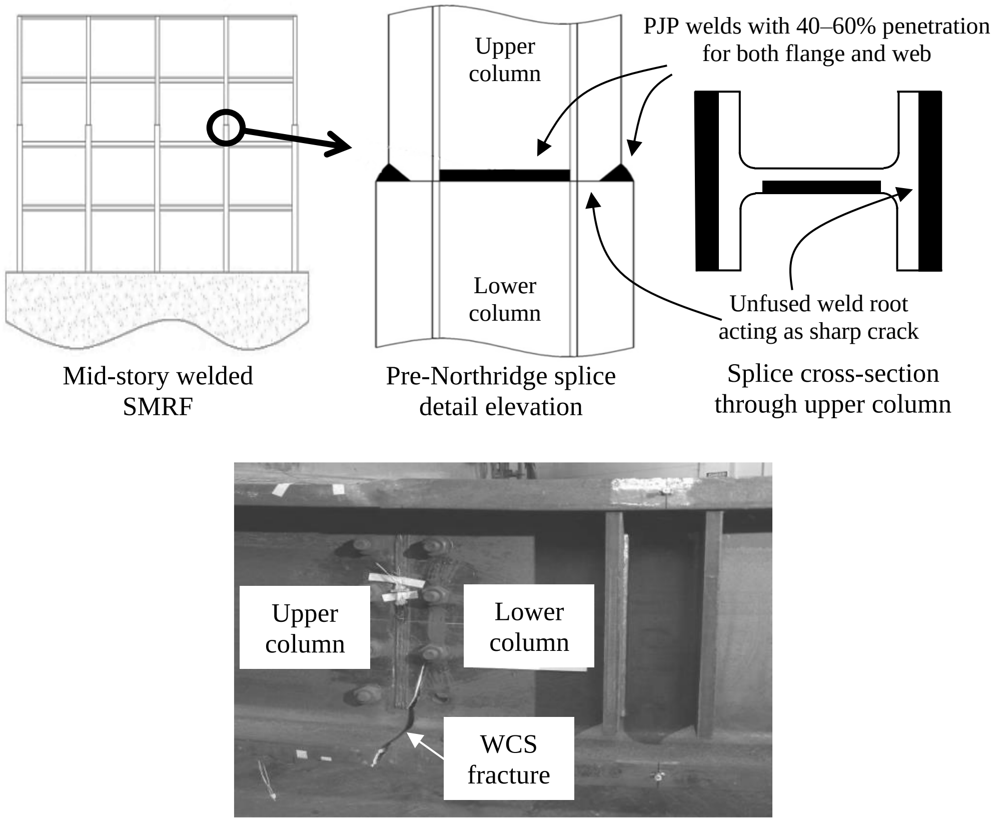

Figure 4.1: Example of welded column splices (WCSs) with partial joint penetration (PJP) welds in pre-Northridge steel moment-resisting frames (SMRFs) and the post-fracture photograph of WCS.

than the CVN toughness value (i.e., 27 J at −18°C) mandated by AISC 341-16 (AISC 2016b), resulting in significantly lower fracture capacity of such connections. This observation has also been confirmed by experimental studies on WCSs prior to the Northridge earthquake (e.g., Bruneau and Mahin 1991) and subsequent finite element fracture mechanics (FEFM) simulations based upon these tests (Nuttayasakul 2000), as well as recent FEFM simulations by Stillmaker et al. (2016). Based on these studies, pre-Northridge WCSs are expected to fracture at flange stresses in the range of 103–172 MPa, much lower than the expected flange yielding strength (i.e., 400 MPa) as specified by the current seismic provision [i.e., AISC 341-16 (AISC 2016b)].

Conventionally, seismic demands in WCSs are estimated to be modest under first-mode building response, since the typical location of WCSs as required by design standards [i.e., AISC 341-16 (AISC 2016b)] is near the mid-story, where the bending moment is low due to double-curvature bending of columns. Significant axial forces and moment demands are nonetheless possible at these locations, as noted in recent nonlinear time history analysis (NLTHA) simulations (Shaw et al. 2015; Shen et al. 2010). This trend is pronounced in high-rise frames, where the temporal peak of tensile stresses in the column flanges of WCSs is comparable to the yield stress of the flange. This is attributable to the participation of higher dynamic modes (which causes single-curvature bending of columns) and overturning (which results in tension of columns).

Galasso et al. (2015) recently conducted a rigorous probabilistic seismic demand analysis (PSDA), fracture fragility [i.e., likelihood of fracture experienced by WCSs over a range of ground motion (GM) hazard intensities] derivation, and fracture risk assessment of WCSs, adopting a performance-based earthquake engineering (PBEE) framework. Findings from this study indicate that high longitudinal stress demands coupled with low fracture capacities in pre-Northridge WCSs result in unacceptably high fracture risk. This is especially true in pre-Northridge SMRFs with WCSs featuring PJP welds with crack-like flaws, resulting in relatively low expected return periods of fracture, on the order of 75 years. This is clearly unacceptable, considering current acceptance criteria for building performance [i.e., ASCE (American Society of Civil Engineers) 7-16 (ASCE 2016)].

The approach used in Galasso et al. (2015) relied on some simplifying, practical assumptions, particularly in accounting for the uncertainties related to stress demands and fracture capacities of WCSs. Thus, while these results provide an important first-order estimate of fracture risk in existing buildings, they do not take advantage of recent advancements of PBEE research, as it pertains to explicit quantification of uncertainties, both aleatory and epistemic, impacting the assessment of seismic performance (e.g., Bradley 2013) and, specifically, of WCS fracture fragility. For instance, the previous studies rely on the (pseudo-) spectral acceleration at the fundamental period of the structure $S_a(T_1)$ as the sole GM intensity measure (IM). This is questionable for several reasons, including that it is agnostic to higher-mode effects, which clearly drive WCS stress demands, particularly in high-rise structures. Thus, it is important to select an IM enabling more accurate estimation of seismic demands by (1) minimizing the record-to-record variability (efficiency); (2) reducing the effect of (other) seismological parameters (sufficiency); and (3) offering hazard computability such that it may be conveniently determined through existing ground motion models (GMMs) and hazard curves or maps.

Also, all previous studies quantifying WCS seismic demands [including Galasso et al. (2015)], do not consider the effect of vertical ground shaking on stress demands in WCSs of mid- to high-rise SMRFs. This is concerning because it is well known that the vertical component of seismic motions may contribute significantly to the seismic demands imposed on structures. Post-earthquake reconnaissance has confirmed that building damage occurring during the Kalamata, Greece (1986), the Northridge, California (1994), the Kobe, Japan (1995), and the L'Aquila, Italy (2009) earthquakes, among others, could be attributed to intense vertical shaking (e.g., Bozorgnia et al. 1998; Papazoglou and Elnashai 1996; Di Sarno et al. 2011).

Finally, Galasso et al. (2015) considered a deterministic value of the fracture capacity (denoted as σ_C) for each splice of interest based on FEFM simulations, without considering uncertainty in these capacities which are often significant. Collectively, these simplifying assumptions and subjectivities have the potential to strongly affect the estimated WCS fracture fragility and risk. Accurate estimation of fracture fragility and risk is particularly critical, since: (1) given their structural function, the fracture risk of WCS connections has major implications for occupant safety and thus, decisions regarding retrofit; and (2) given their location, repair/retrofit of WCS connections is costly and enormously disruptive to building operations. Within this context, this dissertation aims to refine simulation-based fracture fragility assessment for WCS connections, utilizing state-of-the-art research tools, advancing some of them, and putting them into a coherent and harmonized overall approach that is practical to implement. Specifically, the objectives are:

1. To investigate and select the optimal IMs for conditioning probabilistic seismic demand models in terms of global (i.e., maximum inter-story drift ratio, MIDR) and local (i.e., peak tensile stress in the flange of WCSs, σ_D) engineering demand parameters (EDPs) of SMRFs. Particularly, this dissertation aims to investigate the effect of higher modes on σ_D through more sophisticated IMs accounting for spectral shape over a range of periods. The resulting optimal IMs are incorporated in the fracture fragility assessment framework proposed in this chapter;

2. To investigate the effect of the GM vertical component on σ_D and resulting fracture fragility; and
3. To incorporate the uncertainty in the fracture capacity of WCSs (σ_C) into the fracture fragility assessment, through a FEFM-based approach recently developed by Stillmaker et al. (2016)and detailed uncertainty characterization.

The chapter begins by introducing the key factors potentially impacting the uncertainty in seismic demands to WCSs (Section 4.2). This is followed by the introduction of case studies, wherein two SMRF models are investigated through NLTHA (Section 4.3). Section 4.4 focuses on the FEFM-based determination and uncertainty characterization of WCS fracture capacity. Section 4.5 synthesizes these results, providing a critical examination of the fracture fragility, considering these various factors. Finally, Section 4.6 summarizes the findings of this chapter.

4.2 Seismic demand modeling

Two key issues affecting seismic demand uncertainty (in terms of global and local EDPs, i.e., MIDR and σ_D) of WCSs are reviewed and discussed in this section. They are (1) ground-motion IM 'optimization'; and (2) inclusion of GM vertical component for performance-based seismic demand assessment of WCSs.

4.2.1 Selection of optimal IMs for predicting global and local EDPs

A fundamental issue in the framework of PBEE is the choice of optimal ground-motion IMs for conditioning probabilistic seismic demand models. Ground-motion IMs are parameters synthetically describing the intensity of GMs in terms of their effects (e.g., damage potential and loss) on structures. IMs play an important role in PBEE and GM selection procedures, because they link the seismic hazard at a given site and seismic demand analysis for a given structure, thus facilitating probability-based seismic risk assessment. The selection of a single (or a vector of) 'right' IM(s) for building-specific fragility (and vulnerability) characterization has been the subject of a very fertile body of research for at least twenty years. In fact, it is widely accepted that seismic structural performance prediction based on conventional (scalar) GM parameters is subjected to a great deal of variability, which in turn requires greater computational effort to obtain seismic demand estimates with a reasonable level of confidence. A comprehensive overview of this previous research is not within the scope of this chapter, but some key issues related to optimal IM selection are briefly reviewed here.

Generally, optimal IMs should be able to capture as many as possible GM properties (e.g., amplitude, frequency content) that could substantially impact both elastic and inelastic seismic demands (e.g., Freddi et al. 2017). In this dissertation, only those IMs defined based on elastic spectral ordinates and associated structural dynamic characteristics (i.e., modal and elongated periods) are considered[1] and compared by the following criteria: (1) efficiency; (2) sufficiency/relative sufficiency; and (3) hazard computability. The general overview of the selection criteria for optimal IMs can be found in Baker and Cornell (2005), Luco and Cornell (2007), Padgett et al. (2008), among others.

The selection of optimal IMs for predicting global and local EDPs of SMRFs carried out in this chapter is based on (1) the use of a large dataset of (unscaled) recorded earthquake GMs; (2) numerical analyses performed on highly detailed and advanced numerical models; and (3) systematic statistical analysis of the results. These aspects are introduced in the following subsections.

4.2.1.1 Considered IMs

Conventional IMs, including the peak ground quantities (i.e., peak ground acceleration, PGA; peak ground velocity, PGV; and peak ground displacement, PGD) and $S_a(T_1)$, for 5% damping, are the most commonly used IMs. In general, PGA and $S_a(T_1)$ poorly predict demand parameters of mid- to high-rise moment-resisting frames, although the latter IM can sufficiently capture the elastic behavior of first-mode dominated multi-degree-of-freedom (MDoF) systems, especially in the case of low-to-moderate fundamental periods. However, the behavior of highly nonlinear structures or structures dominated by higher-mode periods (less than T_1 – in cases where higher-mode effects are significant, e.g., high-rise structures) is not very well captured by

---

[1] Integral (e.g., duration-related) IMs, e.g., the Arias intensity or significant ground motion duration, are not considered here. In fact, they are usually considered related more to the cyclic energy dissipation rather than to the peak structural response. SMRFs are less sensitive to such a cyclic energy dissipation.

utilizing $S_a(T_1)$ due to the lack of information on the spectral shape (in the range of periods of interest) provided by this IM. Therefore, it is essential to implement advanced IMs accounting for multiple periods and/or consider nonlinear demand-dependent structural parameters. Eads et al. (2015, 2016), Kazantzi and Vamvatsikos (2015), and Kohrangi et al. (2016a) among others have investigated the adequacy of numerous advanced scalar IMs that consider the aforementioned parameters.

Specifically, this chapter investigates an advanced scalar IM option, I_{Np}, which is based on $S_a(T_1)$ and a parameter proxy for the spectral shape (N_p), expressed as:

$$I_{Np} = S_a\left(T_1\right) \cdot N_p{}^{\alpha} \tag{4.1}$$

It was first introduced by Bojórquez and Iervolino (2011), as an improvement of the geometric mean of several spectral acceleration values at different periods, $S_{a,avg}(T_i)$, first proposed by Baker and Cornell (2006):

$$S_{a,avg}\left(T_i\right) = \left(\prod_{i=1}^{n} S_a\left(T_i\right)\right)^{1/n} \tag{4.2}$$

In Eq. (4.1), N_p is defined as:

$$N_p = \frac{S_{a,avg}\left(T_i\right)}{S_a\left(T_1\right)} \tag{4.3}$$

The value for the exponential parameter of N_p in Eq. (4.1), α, must be calibrated during the optimal IM selection process. Bojórquez and Iervolino (2011) provided some recommendations of the α-value for case-study structures (e.g., SMRFs); recently, Minas and Galasso (2019) have calibrated the α-parameter for simplified fragility analysis of mid-rise reinforced concrete (RC) case-study frames, representative of different vulnerability classes (Pre-, Low- and Special-code designs), providing a critical discussion on the possible outcomes of the calibration for the α-parameter.

In this dissertation, ten different values of α, ranging from 0.1 to 1 with 0.1 increments, are tested to determine the optimal α-value. Also, it is worth noting that $S_a(T_1)$ and $S_{a,avg}(T_i)$ correspond to specific cases of I_{Np} when α is equal to 0 and 1, respectively.

It is understood that, for some structures, the contribution to the response from higher modes can be significant. Very often, though, the response is mainly dominated by the first few modes. To account for various structural dynamic features of the considered case-study structures, the second, third, and fourth modal periods (denoted as T_2, T_3, and T_4) and an 'elongated' period [conventionally assumed equal to $1.5T_1$, according to Kohrangi et al. (2016b)] are also specified, together with the structure fundamental period (T_1). This results in different 'periods groups' $(T_i)_j$ considered in the definition of I_{Np}, as follows:

1. Two periods, defined as $(T_i)_1 = [T_1, 1.5T_1]$;
2. Three periods, defined as $(T_i)_2 = [T_2, T_1, 1.5T_1]$;
3. Four periods, defined as $(T_i)_3 = [T_3, T_2, T_1, 1.5T_1]$; and
4. Five periods, defined as $(T_i)_4 = [T_4, T_3, T_2, T_1, 1.5T_1]$.

In total, 41 IMs [i.e., $S_a(T_1)$ plus a combination of four periods groups and 10 considered values of the α-parameter] are considered and investigated in this dissertation.

4.2.1.2 IM efficiency

Efficiency is the most commonly used quantitative criterion for the selection of optimal IMs; this criterion quantifies the variability of demand estimates for different values of a given IM (e.g., Padgett et al. 2008). Specifically, more efficient IMs result in a reduced dispersion of the median EDP estimates conditional to a given IM. Thus, fewer analysis runs are needed to narrow down the confidence intervals for those estimates. The most efficient IM, best predicting a given EDP, is the one providing the largest value of the coefficient of determination, R^2, among those considered or, equivalently, as in this dissertation, the one with the smallest value of the standard deviation, s, of (the natural logarithm of) the considered EDP given the IM.

4.2.1.3 IM sufficiency and relative sufficiency

Different approaches exist for the assessment of IM sufficiency. In particular, Padgett et al. (2008), among others, define sufficiency as a criterion characterizing the level of IM statistical independence conditional to specific earthquake characteristics, such as source-to-site distance (R_s) and magnitude (M_w). According to this approach, sufficiency is quantified based on the residual dependence on R_s and M_w obtained through regression analysis. Therefore, the demand estimates obtained from sufficient IMs are not correlated (or poorly correlated) with the GM parameters R_s and M_w. However, hypothesis testing results on that correlation (and the corresponding p-value analysis) mainly provide a binary evaluation of the IM (i.e., sufficient or insufficient) without offering any indication concerning the level of insufficiency, when this is detected. More in general, hypothesis-testing results do not explicitly quantify the relative performance of different, sufficient or insufficient, candidate IMs.

As an alternative measure of GM sufficiency, relative sufficiency has been recently proposed by Jalayer et al. (2012). In particular, this measure investigates the relative sufficiency of a second IM, IM_2, with respect to a first one, IM_1. This measure is derived based on information theory concepts and quantifies the suitability of one intensity measure relative to another. Specifically, the relative sufficiency measure, denoted herein as $I(\mathrm{EDP}|\mathrm{IM}_2|\mathrm{IM}_1)$, is equal to the average difference between the information gained (measured in terms of Shannon entropy or simply, entropy) about the performance variable/parameter (i.e., EDP) by knowing IM_2 instead of IM_1. If $I(\mathrm{EDP}|\mathrm{IM}_2|\mathrm{IM}_1)$ is positive, it means that on average IM_2 provides more information about EDP than IM_1; therefore, IM_2 is more sufficient than IM_1. Similarly, if $I(\mathrm{EDP}|\mathrm{IM}_2|\mathrm{IM}_1)$ is negative, IM_2 is less sufficient than IM_1. This measure is numerically expressed as:

$$I\left(\mathrm{EDP}\middle|\mathrm{IM}_2\middle|\mathrm{IM}_1\right) \cong \frac{1}{N_{\mathrm{rec}}} \sum_{i=1}^{N_{\mathrm{rec}}} \log_2 \frac{p\left(\mathrm{EDP} = edp_i \middle| \mathrm{IM}_2\right)}{p\left(\mathrm{EDP} = edp_i \middle| \mathrm{IM}_1\right)} \tag{4.4}$$

where, N_{rec} is the total number of selected GM records (refer to Section 4.3.2 below), edp_i is the EDP value corresponding to the i-th GM obtained through NLTHA, and $p[\mathrm{EDP} = edp_i|\mathrm{IM}]$ is the probability density function (PDF) of edp_i given the specific IM. More details on the derivation of Eq. (4.4) are provided in Jalayer et al. (2012). The relative sufficiency measure is estimated for each performed cloud analysis (described in Section 4.3.3 below) and is measured in units of bits of information [as the logarithm of Eq. (4.4) is calculated in base two]. According to Jalayer et al. (2012), the relative sufficiency measure provides a preliminary ranking of candidate IM_2 with respect to the reference IM_1. The approximation of Eq. (4.4) can be used for a fast screening of various candidate IMs.

4.2.1.4 Hazard computability

Hazard computability describes the process to obtain the earthquake hazard at a given site in terms of a considered IM. Numerous hazard maps and GMMs (or attenuation laws) exist for the most commonly used IMs, i.e., PGA and spectral ordinates at given periods (representing sometimes a restricted range of possible discrete periods), making these IMs more favorable from the hazard-computability perspective. Other IMs (such as spectral ordinates at the actual fundamental and/or elongated periods and advanced IMs) may require interpolation or supplementary information, making the computation of the hazard a more time-consuming process; however, they are still hazard computable, as shown in Minas and Galasso (2019), among others.

4.2.2 The effects of earthquake GM vertical components

This subsection summarizes some relevant previous studies assessing the effects of the GM vertical component on the seismic response of SMRFs. Given the primary interest in WCS fracture, a specific type of EDP (i.e., axial force in the columns) under vertical ground shaking has been considered in all the selected studies.

Field evidence reported by Papazoglou and Elnashai (1996) of steel building damage from three earthquakes, including Kalamata, Greece (1986), Northridge, California (1994), and Kobe, Japan (1995), reveals the possibility of column brittle tensile failure due to high axial force, attributable to strong vertical GM components.

The rest of the considered studies deal with simulation-based (i.e., numerical) investigations on the effect of the GM vertical component. For instance, Papaleontiou and Roesset (1993) have studied four 3-bay SMRFs with 4-, 10-, 16- and 20-story, respectively. These considered case-study frames were designed to represent a broad range of vertical to horizontal periods ratios. Linear time history analysis (LTHA) of these four frames was performed using the 1989 Loma Prieta record from the Capitola station (PGA values of vertical and horizontal motions are 0.52 g and 0.47 g, respectively); separate horizontal and vertical components of the seismic records, and their simultaneous action were considered without the inclusion of gravity loads. In these particular cases, the observed axial forces induced by the vertical shaking in both the interior and exterior columns, having a comparable magnitude to horizontal motion, were larger than the corresponding axial forces caused by the horizontal ground shaking only. Similar results and conclusions were drawn by other researchers. For instance, Salazar and Haldar (2000) developed a time-domain nonlinear finite element computer program to evaluate the seismic responses of SMRFs by applying the horizontal and vertical components of each earthquake GM (one record from the EI Centro earthquake of 1940 and two GMs recorded during the 1994 Northridge earthquake) simultaneously; similarly, Macrae et al. (2000) carried out inelastic NLTHAs of nine 2-dimensional SMRFs using a suite of GM records with different characteristics to estimate the effect of vertical component of ground shaking. More recently, a low-rise code-compliant SMRF was designed by Di Sarno (2012) and was subjected to combined horizontal and vertical earthquake loading of seven records from the 2011 Christchurch (New Zealand) earthquakes, characterized by a large ratio between vertical and horizontal PGAs. Both LTHA and NLTHA were performed and the previous observations on the structural response (specified as axial forces) in steel columns were confirmed by the author.

In general, all these studies observed greater axial stresses in columns caused by strong vertical shaking and highlighted that the increase of axial stress could exceed by far the compression force due to gravity load.

4.3 Case-study frame modeling, record selection, and cloud analysis

The first step of this chapter consists in performing NLTHA of case-study structures, then estimating the probability distributions of the considered EDPs (i.e., MIDR and σ_D) conditional on each considered IM. Such conditional probability distributions can be obtained through various types of NLTHA procedures (Jalayer and Cornell 2009). Particularly, the one employed here is cloud analysis (Jalayer 2003). For illustrative proposes, two case-study SMRF computational models (both featuring WCSs) are developed and assessed through different sets of unscaled (real) GMs with the aim of addressing the issues described in Section 4.2.

4.3.1 Case-study frame models

In this dissertation, two generic frames (i.e., 4-story and 20-story), schematically illustrated in Figure 4.2, are considered. Both frames are similar to the frames used by Shen et al. (2010), Shaw et al. (2015), and afterward by Galasso et al. (2015), for seismic demand characterization of WCSs. These structures are adapted from those examined in the SAC steel project (Gupta and Krawinkler 1999) in terms of the geometry (i.e., same floor plans and elevations) and design, with the difference that the 3-story SAC model building is replaced by a 4-story building to accommodate the WCS (which is uncommon for buildings with less than three stories). The design of this 4-story building has been rechecked. The considered frames are assumed to be designed for seismicity (and typical gravity loading for office occupancy) consistent with the Los Angeles area, California, assuming firm soil conditions (i.e., NEHRP – National Earthquake Hazards Reduction Program – Site Class D).

Based on these assumptions, the case-study frames are designed as per ASCE 7-05 (ASCE 2006) and AISC 341-10 (AISC 2010). The first four horizontal modal periods (denoted as T_1, T_2, T_3, and T_4) and the fundamental vertical period (denoted as

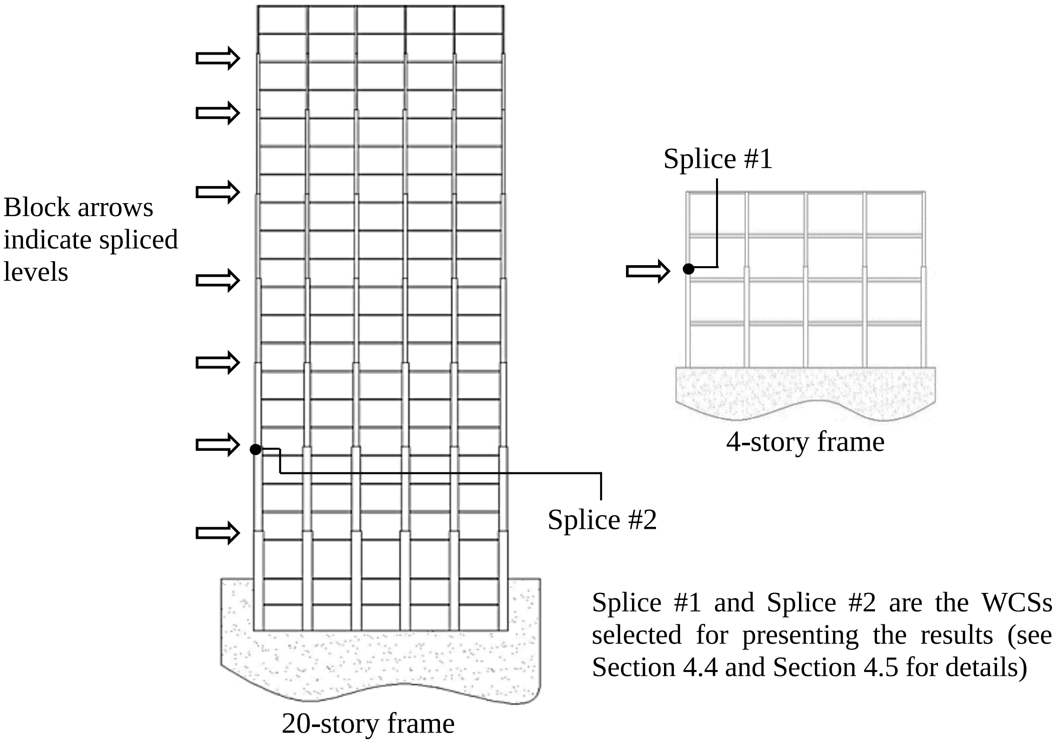

Figure 4.2: Schematic illustration of 4- and 20-story case-study SMRF models, and the locations of two representative WCSs.

T_V) calculated from elastic modal analysis for the 4- and 20-story frames are listed in Table 4.1. Greater details related to the building design (e.g., design assumptions, loading conditions, and frame member size specifications) can be found in Shaw (2013) and Shaw et al. (2015).

It is important to acknowledge here that, despite being designed as per codes and standards developed after the Northridge earthquake, the stress demands in the splices are consistent with those in pre-Northridge frames. As reported by Gupta and Krawinkler (1999) based on extensive time history simulations, the main difference between the pre- and post-Northridge frames arises mainly in the local moment distribution in the beam and column connections. This is due to detailing factors such as the introduction of reduced beam sections or flange reinforcements. In fact, the time history simulations suggested that the global response and member force demands are virtually identical between pre- and post-Northridge frames designed for the same conditions. As a result, it is assumed that the splice demands used in this dissertation (to follow) are fair representations of those in pre-Northridge frames.

The splice locations in each considered frame are also indicated in Figure 4.2 using block arrows. In each spliced level, WCSs are located 1.2 m from the top surfaces of the lower story beams, which is the minimum distance requirement as per AISC 341-10 (AISC 2010) to reflect the least conservative scenario of the design standard. OpenSees (Mazzoni et al. 2009) is used to develop highly detailed nonlinear models and simulate both frames.

In these two models, force-based fiber sections are created for all beams and columns, with the purpose to simulate axial force-moment interaction and to spread plasticity through the whole length of each structural member. The fiber sections also provide a direct examination of the tensile stress at various locations within the cross-section. Reduced beam sections are also modeled as fiber elements to control the

Table 4.1: First four horizontal modal periods and fundamental vertical period for the 4- and 20-story frames [s]

Frame story	T_1	T_2	T_3	T_4	T_V
4-story	0.94	0.28	0.15	0.09	0.09
20-story	2.36	0.84	0.48	0.34	0.30

location of plastic hinge formation and the panel zones are considered as rigid links by multiplying a factor of 10 to the stiffness and strength of the initial material of the models (Shaw 2013). Finite joint sizes are modeled through rigid offsets. A bilinear kinematic hardening relationship is utilized to model the cyclic response of steel in the fiber sections, with Young's modulus (E_{modulus}) equal to 2.0×10^5 MPa, a hardening slope equal to 5% of the initial elastic modulus, and yield strength F_y equals to 380 MPa. These values were calibrated to match an extensive empirical dataset of plastic hinge responses obtained by Lignos et al. (2011) and are consistent with the previous modeling by Galasso et al. (2015), Shaw et al. (2015), and Stillmaker et al. (2017).

The selected constitutive model does not represent effective softening or deterioration due to effects such as local or lateral-torsional buckling. Although representation of such softening is important for simulating global instabilities such as collapse, it is (as the results, discussed later, indicate) of relatively modest significance here. In fact, fracture risk of WCSs is dominated by low- to medium-intensity ground shaking at which building deformations (< ~3% MIDR) are not large enough to trigger these types of softening. This effect, noted previously by Galasso et al. (2015), is attributed to the saturation of stresses in WCSs at relatively low levels of hazard, owing to yielding in other elements of the structure (e.g., beams). Geometric nonlinearities, at both member- (i.e., P-δ) and story- (i.e., P-Δ) levels, are explicitly simulated using geometric transformations. A leaning column is also added in each model to capture the destabilizing effects of vertical forces on the gravity frames.

It is worth noting that fracture propagation is not simulated in this dissertation, whose primary focus is to characterize WCS stress demands from the perspective of informing the need for retrofit at a component level, considering the failure of the first splice as the critical event controlling retrofit decisions. Nonetheless, propagation of fracture and its effect on building response is critical for a more holistic development of retrofit strategies. This has been addressed by Stillmaker et al. (2017), which required development of a special material in OpenSees to represent flange fracture.

4.3.2 Selection of GM sets

Different sets of unscaled earthquake records are properly selected. The adopted selection procedures are described and discussed in this subsection.

4.3.2.1 GM sets for selecting optimal IMs

Unscaled GM records selected from the SIMBAD (*Selected Input Motions for displacement-Based Assessment and Design*) database (Smerzini et al. 2014) are used to perform cloud-based NLTHA. The considered database consists of 467 three-component accelerograms, including two horizontal (X- and Y-) and one vertical (Z-) components, obtained from 130 worldwide seismic events (covering mainshocks and aftershocks) included in various strong GM databases assembled for different high-seismic regions. Specifically, all the records in SIMBAD come from shallow crustal earthquakes with moment magnitude (M_w) ranging from 5 to 7.3 and epicentral distance (R_{epi}) less than 35 km; a wide range of local site conditions is also represented in SIMBAD. This results in a GM database capable of providing strong GMs of relevance for most of the design/assessment conditions of interest, avoiding the need for large scaling. From the full SIMBAD database, a subset of 100 GM records is considered to provide a statistically significant number of strong-motion records of engineering relevance for the applications in this chapter. These records are arbitrarily selected for each building characterized by its T_1 (given in Table 4.1) by first ranking the 467 records in terms of their $S_a(T_1)$ values (by using the geometric mean of the two horizontal components) and then keeping the component with the larger $S_a(T_1)$ value [for the 100 stations with the highest mean $S_a(T_1)$]. It is worth noting that different GMs are selected for the 4- and 20-story steel frames due to the different T_1 values for each frame. Also, site-specific record selection is outside the scope of this dissertation. In fact, this choice is compatible with the cloud approach used here and the use of generic archetype structures.

Figures 4.3(a) and (c) show the 5%-damped pseudo-acceleration response spectra of the selected 100 GM records for the 4- and 20-story case-study frames, respectively. The vertical dashed lines in these two figures indicate the fundamental horizontal periods of the 4- (T_1 = 0.94 s) and 20-story (T_1 = 2.37 s) frames.

4.3.2.2 GM sets for evaluating the effect of vertical GM components on WCS stress demands

The GM records used for investigating the effect of the GM vertical component on the seismic demand estimates of WCSs are obtained from the same database described

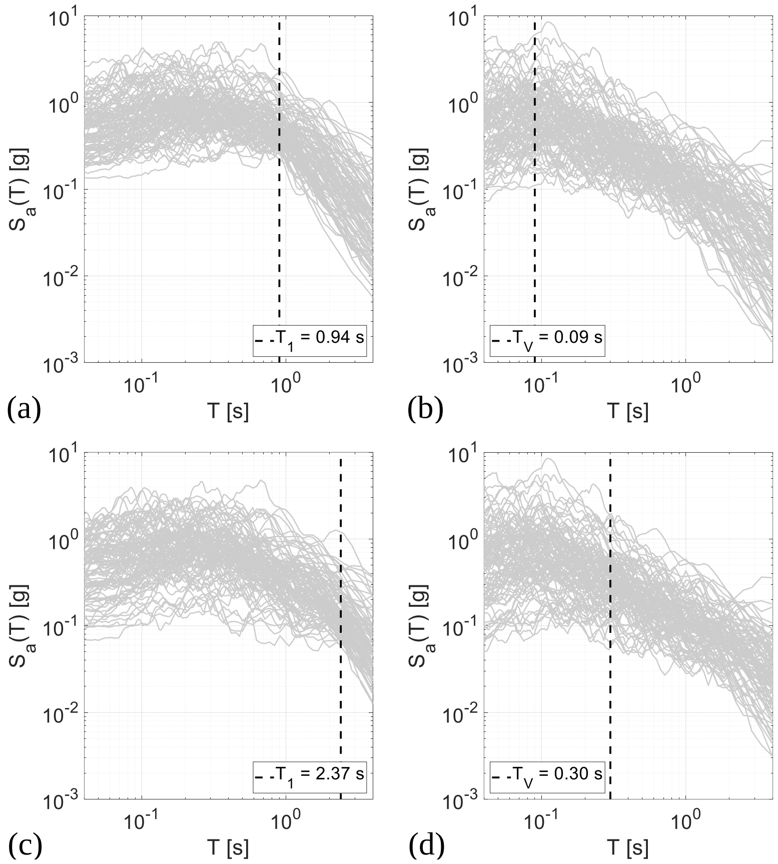

Figure 4.3: 5%-damped pseudo-acceleration response spectra of the 100 selected GMs for Scenario #1 and 4-story frame (top panel), corresponding to (a) horizontal, and (b)vertical components; and 20-story frame (bottom panel), corresponding to (c) horizontal and (d) vertical components.

above (i.e., SIMBAD). To investigate the effect of the vertical GM component on the WCS stress demands (σ_D) and quantify its increase induced by the vertical ground shaking, two strategies are employed:

1. Selection of 100 GM records with ‘maximum’ horizontal components (X- or Y-, ‘maximum’ to indicate the same selection criteria discussed in Section 4.3.2.1) and the corresponding vertical components (Z-); and
2. Selection of 100 earthquake records with ‘maximum’ vertical components (Z-) and their corresponding stronger horizontal components (between X- and Y-).

For the first scenario (Scenario #1), the two sets of 100 GMs selected in Section 4.3.2.1 for the 4- and 20-story case-study frames [i.e., Figures 4.3(a) and (c)] are employed. Then, their associated Z- components are selected as vertical counterparts from the same 100 recording stations. Pseudo-acceleration response spectra of these selected vertical GMs are shown in Figures 4.3(b) and (d), respectively; the fundamental vertical periods of 4- (T_V = 0.09 s) and 20-story (T_V = 0.30 s) frames are displayed as vertical dashed lines in these two figures.

For the second scenario (Scenario #2), a subset of 100 GM records is selected for each considered frame characterized by its fundamental vertical period (T_V) from SIMBAD. The values of spectral acceleration at T_V for a damping ratio of 5%, $S_a(T_V)$, for the 467 records (Z- components) are first calculated for the 4- and 20-story frames: the 100 records characterized by the largest $S_a(T_V)$ values (for each building) are then selected to form the GM sets. Figures 4.4(b) and (d) show the pseudo-acceleration response spectra (for a damping ratio of 5%) of these selected vertical GMs for the 4- and 20-story frames, respectively. Following this, the stronger horizontal components (X- or Y-), i.e., those with the larger values of $S_a(T_1)$ corresponding to the same

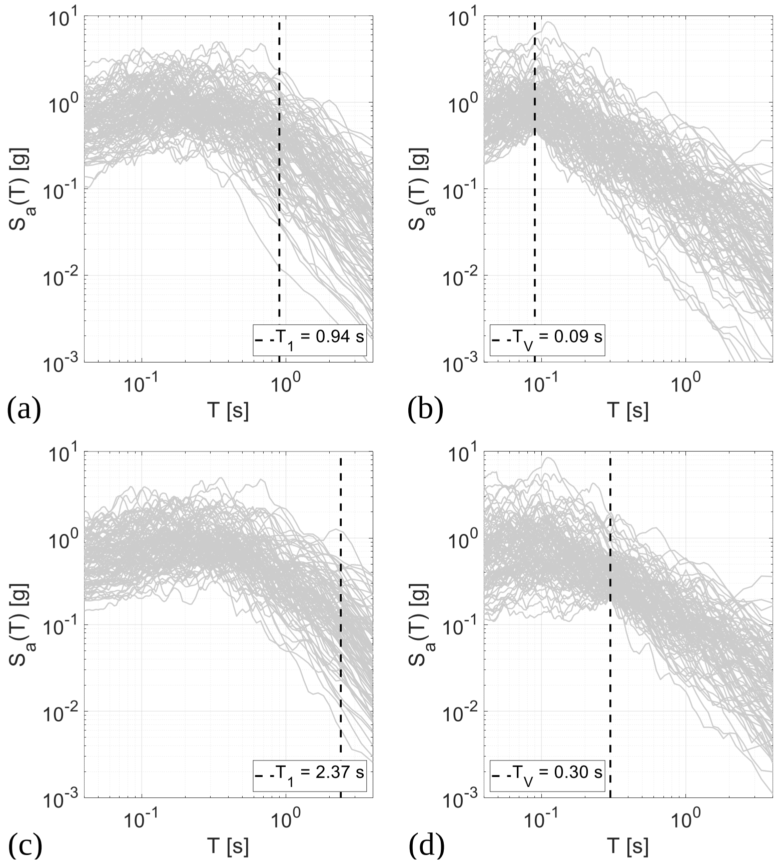

Figure 4.4: 5%-damped pseudo-acceleration response spectra of the 100 selected GMs for Scenario #2 and 4-story frame (top panel), corresponding to (a) horizontal, and (b)vertical components; and 20-story frame (bottom panel), corresponding to (c) horizontal and (d) vertical components.

stations with the highest $S_a(T_V)$ values, are then employed [as presented in Figures 4.4(a) and (c)].

4.3.3 Cloud analysis

The cloud analysis (Jalayer 2003) is a widely-used NLTHA procedure in which a structural model is subjected to a set of unscaled GMs (each characterized by different IM values). This results in a "cloud" of IM-EDP pairs and the linear least squares is applied on those pairs to estimate the conditional mean and standard deviation of EDP given IM. In this chapter, cloud analysis of both 4- and 20-story frame models is carried out considering the GM sets described above to obtain seismic demand estimates.

The simple power-law model in Eq. (4.5) is used in the cloud analysis:

$$\mathrm{EDP} = a\mathrm{IM}^{b} \tag{4.5}$$

This power-law model can be simply re-written as in Eq. (4.6), as a linear expression of the natural logarithm of the EDP and the natural logarithm of the IM (Jalayer 2003):

$$\ln\left(\mathrm{EDP}\right) = \ln(a) + b\ln(\mathrm{IM}) + o \tag{4.6}$$

In both equations above, a and b are the parameters of the regression; and o in Eq. (4.6) is a zero-mean random variable representing the variability of ln(EDP) given the IM. The use of logarithmic transformation indicates that the EDPs are assumed to be conditionally lognormally distributed (conditional on the values of the IMs); this is a common assumption that has been confirmed as reasonable in many past studies.

The standard deviation of this linear regression-based probabilistic model (s) is assumed to be constant with respect to IM over the range of IMs in the cloud and equal to:

$$s = \sqrt{\frac{\sum_{i=1}^{N_{\mathrm{rec}}}\left[\ln\left(edp_i\right) - \ln\left(a \cdot im_i^{b}\right)\right]^2}{N_{\mathrm{rec}} - 2}} \tag{4.7}$$

where, edp_i and N_{rec} have the same meaning as those in Eq. (4.4), and im_i is the IM value corresponding to the i-th GM. It is noteworthy to mention that significant heteroskedasticity may occur within some IM-EDP combinations and this feature should be modeled explicitly when generating fragility functions, for example performing linear regressions locally in a region of IM values of interest (e.g., Freddi et al. 2017). However, the use of a less complex approach is chosen here as it adequately serves the purposes of this chapter.

4.4 Uncertainty characterization of WCS stress capacity

In this chapter, a fracture mechanics-based approach recently developed by Stillmaker et al. (2016) is adopted to capture the uncertainty in the stress capacity of WCSs (i.e., σ_C). This method primarily consists of four components: (1) advanced FEFM simulations based on the test data collected by Shaw et al. (2015); (2) functional forms development (to determine WCS stress capacity as a function of several parameters describing the splice geometry and material toughness property) based on the FEFM simulations; (3) uncertainties characterization for each input parameters, including modeling uncertainties; and (4) determination of WCS strength distribution through Monte Carlo simulation of these uncertainties.

The functional forms selected to estimate the WCS flange stress capacity are shown in Eqs. (4.8)–(4.13), including various parameters: (1) initial crack length, a_c; (2) top flange thickness, t_{upper}; (3) lower flange thickness, t_{lower}; (4) flange thickness ratio, $\xi = t_{\text{upper}}/t_{\text{lower}}$; (5) crack penetration ratio, $\eta = a_c/t_{\text{lower}}$; and (6) Charpy V-Notch (CVN) value:

$$\sigma_{C,\text{estimate}} = \frac{K_{IC}}{\sqrt{\pi \times (\eta/2\xi) \times t_{\text{upper}}}} \times \frac{1}{\xi\sqrt{\tau} \times f_1(\eta) \times f_2(\xi) \times g_1(\eta) \times g_2(\xi)} \tag{4.8}$$

The first term at the right side of Eq. (4.8) denotes a linear elastic fracture mechanics-based estimation of the allowable stress in an infinite plate with a center crack (Anderson 2005; Saxena 1998). The critical stress intensity factor K_{IC} could be determined from CVN by the expression in Eq. (4.9), which is the best fit rather than the lower-bound correlation derived by (Barsom 1975):

$$K_{IC} = \sqrt{0.001 \times (0.979 \times \mathrm{CVN}) \times E_{\mathrm{modulus}}} \tag{4.9}$$

The second term at the right side of Eq. (4.8) represents modifications to the stress capacity solution; the factor τ in the denominator is equal to 1 for a center-cracked (CC) configuration while it is equal to 2 for an edge-cracked (EC) case [refer to Stillmaker et al. (2016) for details]. The rest four functions in the denominator could be expressed as:

$$f_1(\eta) = A_{\mathrm{I}}\eta^2 + A_{\mathrm{II}}\eta + A_{\mathrm{III}} \tag{4.10}$$

$$f_2(\xi) = B_{\mathrm{I}}(\xi - 1)^2 + B_{\mathrm{II}}(\xi - 1) + 1 \tag{4.11}$$

$$g_1(\eta) = \left(C_{\mathrm{I}}K_{IC}^3 + C_{\mathrm{II}}K_{IC}^2 + C_{\mathrm{III}}K_{IC}\right)\eta + C_{\mathrm{IV}}K_{IC}^3 + C_{\mathrm{V}}K_{IC}^2 + C_{\mathrm{VI}}K_{IC} + 1 \tag{4.12}$$

$$g_2(\xi) = \left(D_{\mathrm{I}}K_{IC}^2 + D_{\mathrm{II}}K_{IC} + D_{\mathrm{III}}\right)(\xi - 1)^2 + 1 \tag{4.13}$$

The coefficients contained in Eqs, (4.10)–(4.13) (i.e., A_{I}, A_{II}, …, D_{II}, D_{III}) have been calibrated by Stillmaker et al. (2016). Note that only two representative splices (i.e., labeled as Splice #1 and Splice #2 for the 4- and 20-story frames in Figure 4.2, respectively) are selected, using a similar approach to that of Galasso et al. (2015), i.e., the selected splice flanges are characterized by the maximum stress level (among all splice flanges in the given frames) at the 10/50 stress-hazard level. In this case, only one set of calibrated coefficients corresponding to both representative splices (out of four in total) is summarized in Table 4.2, which is the edge-cracked and unequal flange (EC-UF) class. The reported mean and standard deviation of the ratio between the stress capacity values obtained via the FEMF simulations ($\sigma_{C,\mathrm{FEM}}$) and their estimated counterparts [$\sigma_{C,\mathrm{estimate}}$ of Eq. (4.8)] are 1.024 and 0.125, respectively. These indicate that the fitted parameters (see Table 4.2) are generally good.

According to Stillmaker et al. (2016), all the parameters in Eq. (4.8), including three geometric parameters (i.e., thickness of upper flange, t_{upper}; thickness of lower flange, t_{lower}; and crack length, a_c) and a material parameter (i.e., CVN), are potential sources of uncertainty in the WCS fracture capacity model. Moreover, the estimation of $\sigma_{C,\mathrm{estimate}}$ [through Eq. (4.8)] also depends on the data obtained from FEFM simulation (i.e., $\sigma_{C,\text{FEM}}$), which may not be an accurate representation of the true flange stress capacity (assumed to be represented by the data from the experimental testing, $\sigma_{C,\text{test}}$). To capture this modeling uncertainty arising from the capacity estimation equation, the true flange stress capacity $\sigma_{C,\text{true}}$ can be decomposed as:

$$\sigma_{C,\text{true}} = \left(\frac{\sigma_{C,\text{test}}}{\sigma_{C,\text{FEM}}} \right) \times \left(\frac{\sigma_{C,\text{FEM}}}{\sigma_{C,\text{estimate}}} \right) \times \sigma_{C,\text{estimate}} \tag{4.14}$$

The first two terms in the decomposition above could be simulated as random variables (RVs). In summary, the uncertainty in $\sigma_{C,\text{true}}$ may be due to the following three sources: (1) geometry; (2) material characteristics; and (3) modeling. All these sources of uncertainty are considered as RVs in the analysis and their statistical distributions, in terms of distribution type, bias factor (i.e., the ratio of the mean value of each RV to its nominal value), and coefficient of variation (CoV, i.e., the ratio between the standard deviation to the mean of each RV) are listed in Table 4.3. These statistics represent the input for Monte Carlo simulation. Further details on the uncertainty characterization for flange stress capacity estimation can be found in Stillmaker et al. (2016). Another source of uncertainty is that of the construction practice due to welding. Currently, there is a lack of data to simulate this effect in a meaningful way. Nonetheless, if such data becomes available, this type of variability may be easily

Table 4.2: Calibrated coefficients and fitting metrics for Eqs. (4.10)–(4.13) (adapted from Stillmaker et al. 2016)

Term	Coefficient	Splice #1 and Splice #2 (EC-UF type)
$f_1(\eta)$	A_{I}	4.31
	A_{II}	0.247
	A_{III}	1.12
$f_2(\xi)$	B_{I}	4.25
	B_{II}	0.390
$g_1(\eta)$	C_{I}	1.34×10^{-6}
	C_{II}	-4.13×10^{-4}
	C_{III}	0.0161
	C_{IV}	-6.91×10^{-7}
	C_{V}	2.25×10^{-4}
	C_{VI}	-6.00×10^{-3}
$g_2(\xi)$	D_{I}	2.48×10^{-4}
	D_{II}	-0.0697
	D_{III}	3.46

incorporated into the analysis, for example, by further increasing the standard deviation in the fracture toughness, or the initial crack length.

Additionally, the nominal values of upper flange and lower flange thicknesses are adopted from Shaw (2013) – for Splice #1, t_{upper} is 48.01 mm (W14×257 section, 1.89 in) and t_{lower} is 62.74 mm (W14×342 section, 2.47 in); while for Splice #2, t_{upper} is 48.01 mm (W24×250 section, 1.89 in) and t_{lower} is 57.91 mm (W24×306 section, 2.28 in). In general, a weld penetration of 50% of the smaller connected flange thickness was often specified in the seismic regions for the pre-Northridge era (Bruneau and Mahin 1990); as a result, the nominal initial crack length (a_c) is assigned as half of t_{upper}. The typical value of CVN toughness is selected as 13.6 J for pre-Northridge WCSs (Chi et al. 2000).

According to the specified nominal/typical values and the defined statistical distributions of all the RVs, the uncertainties in the stress capacity of these two WCS flanges can be characterized through (plain) Monte Carlo simulation. As an example, Figure 4.5 shows the generated 1,000 random samples of the flange stress capacities (σ_C) of Splice #1 (for the 4-story frame) and Splice #2 (for the 20-story frame), in the form of corresponding histograms fitted with lognormal distribution.

A sensitivity analysis (not reported here for brevity) was performed to identify the number of samples required to estimate the distribution of the WCS fracture capacity through Monte Carlo simulation. In particular, the analysis was repeated by varying the number of samples for the Monte Carlo simulation from 100 to 10,000, with a step of 100. Results of the analysis confirmed that 1,000 samples allow one to

Table 4.3: Statistical distribution of RVs in the uncertainty analysis (adapted from Stillmaker et al. 2016)

Category	Variable	Bias	CoV (%)	Distribution
Geometry	Upper flange thickness (t_{upper})	1.01	1.0	Normal
	Lower flange thickness (t_{lower})	1.01	1.0	Normal
	Initial crack length (a_c)	1.01	3.0	Normal
Material	Steel Charpy V-Notch toughness (CVN)	1.00	7.0	Lognormal
Model	Error in correlation of Eq. (4.9)	1.00	11	Normal
	$\sigma_{C,\mathrm{FEM}}/\sigma_{C,\mathrm{estimate}}$ of EC-UF-type WCS	1.02	12.3	Normal
	$\sigma_{C,\mathrm{test}}/\sigma_{C,\mathrm{FEM}}$	1.1475	6.5	Normal

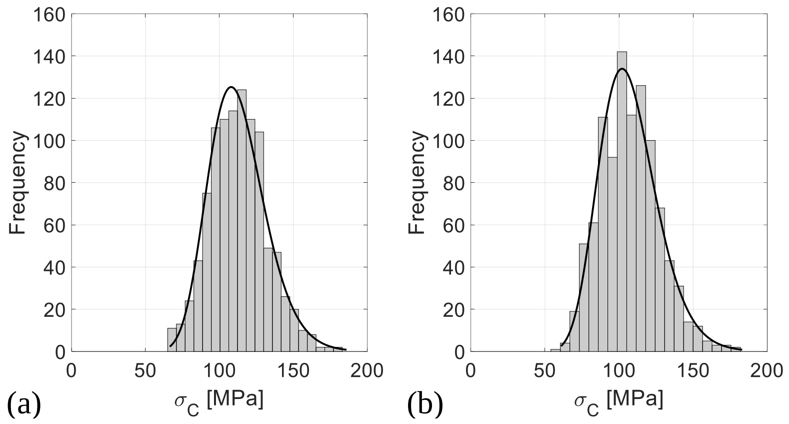

Figure 4.5: Examples of Monte Carlo simulation results in terms of flange stress capacities (σ_C) of representative WCSs: (a) Splice #1 for the 4-story frame; and (b) Splice #2 for the 20-story frame.

obtain ‘stable’ estimates of the WCS fracture capacity distributions and their parameters (and consequently, of fracture fragility) for the considered splices. Indeed, this result was expected, given the assumed values of the CoV for each RV involved in Eqs. (4.8)–(4.14) (and Table 4.3).

4.5 Results and discussion

Results of the investigation on the seismic demand and capacity uncertainties of the 4- and 20-story case-study frames and for the two selected WCSs (i.e., Splice #1 and Splice #2) are presented in this section. Results for the other WCSs in the case-study frames are not reported here for the sake of brevity. However, findings from the analysis are consistent across the full set of WCSs. In particular, according to Section 4.2, two main issues (i.e., optimal IM selection and inclusion of GM vertical component) on the seismic demand (σ_D) of WCS are investigated and discussed first. The fracture fragility assessment is performed for each considered issue, to quantify their effects on the fracture fragility parameters. Finally, the effect of the uncertainty characterizing fracture capacity (σ_C) on the resulting fracture fragility is investigated using the proposed FEFM-based approach (described in Section 4.4).

4.5.1 Optimal IM selection

In this subsection, all the 41 considered IMs, including $S_a(T_1)$ (i.e., I_{Np} with α = 0), $S_{a,avg}(T_i)$ (i.e., I_{Np} with α = 1) and I_{Np} (with a range of α-values between 0.1 and 0.9) with the four ‘periods groups’ [i.e., $(T_i)_j$, j = 1, 2, 3, 4] defined in Section 4.2.1.1, are assessed based on the selection criteria introduced in Section 4.2.1. In particular, the overall performance of each considered IM, for each considered EDP (i.e., MIDR or σ_D, obtained through cloud analysis), is assessed by computing and comparing the quantitative parameters related to each tested criterion. Once the optimal IMs are determined for Splice #1 and Splice #2, results of the fragility analysis conditional to $S_a(T_1)$ (state-of-practice) and the optimal IM for each considered WCS are compared and results are also critically discussed.

4.5.1.1 Results of IM efficiency tests

For the sake of brevity, Figures 4.6(a)–(b), and Figures 4.7(a)–(b) only illustrate the scatter (cloud) plots of seismic demands in terms of MIDR and σ_D versus $S_a(T_1)$ and the obtained optimal IMs (from the 41 IM candidates considered in this dissertation, Section 4.2.1.1), for each case-study frame and each selected WCS. The standard deviation (s) of each logarithm regression is also given in the figures. To some extent, the visual inspection and the values of s confirm that the IMs such as I_{Np} and $S_{a,avg}(T_i)$, which are able to account for the spectral shape in a range of periods of interest, are more efficient than $S_a(T_1)$.

To further expand on this, Figures 4.6(c)–(d), and Figures 4.7(c)–(d) display the standard deviation of residuals for MIDR and σ_D, for all the considered IMs and each case-study frame/splice. All these figures confirm that, when the α-value of I_{Np} approaches zero, I_{Np} tends to approximate $S_a(T_1)$, resulting in almost identical values of s between EDP given I_{Np} ($\alpha = 0.1$) and EDP given $S_a(T_1)$, even if up to five periods of interest [i.e., $(T_i)_4$] are considered. Similarly, when the value of α-parameter approaches one, I_{Np} approximates the geometric mean of spectral acceleration values at considered periods, i.e., $S_{a,avg}(T_i)$. Therefore, the α-parameter used in the I_{Np} definition is a proxy for the weight of the contributions of the spectral accelerations corresponding to higher modes and the assumed elongated period to each considered EDP. These four figures also show that accounting for higher-mode periods (T_2, T_3, and T_4) and the assumed elongated period ($1.5T_1$) has an impact on the efficiency of the considered IMs, but not always in a positive way. In most cases, especially when looking at Figures 4.6(d) and 4.7(c), the use of more periods significantly reduces the standard deviation of EDP residuals, particularly in the case of σ_D and the 20-story

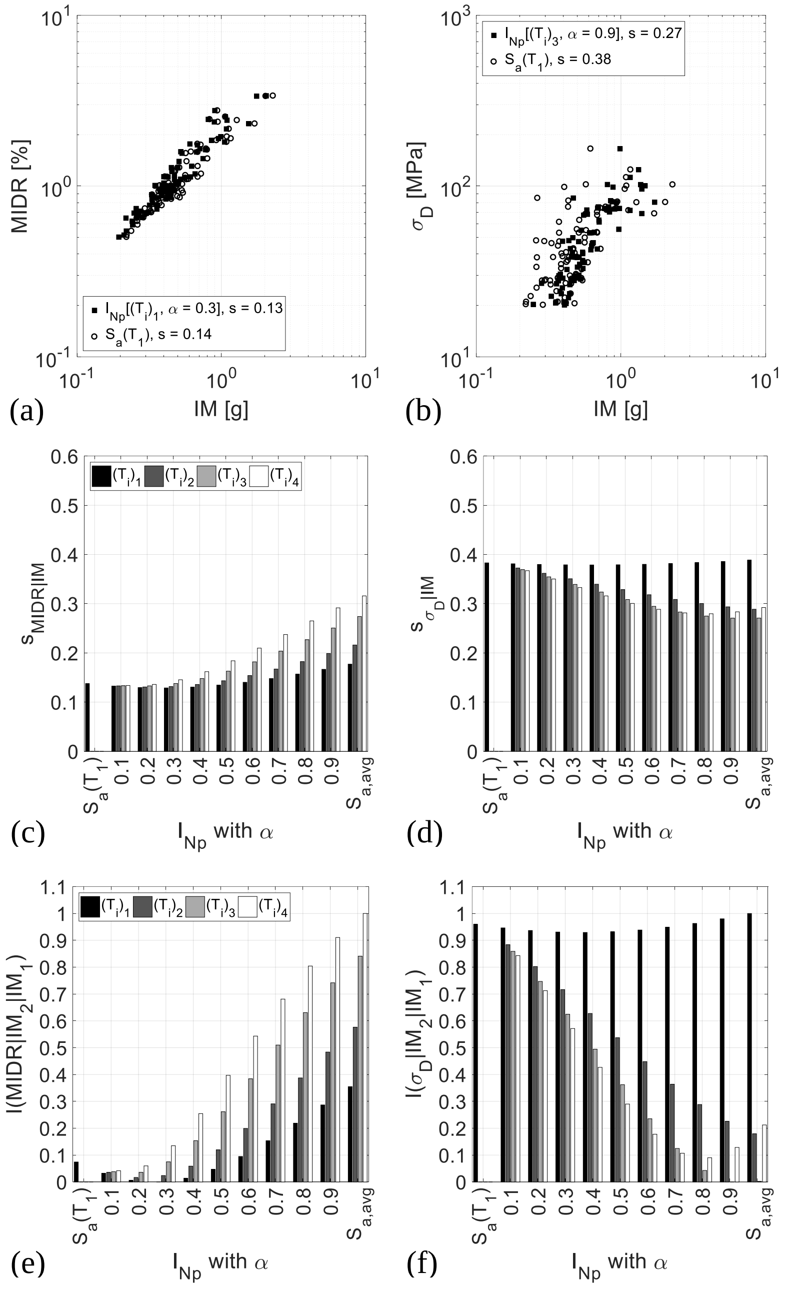

Figure 4.6: Results of optimal IM selection for the 4-story case-study frame: scatter plots of (a) MIDR, and (b) σ_D versus optimal IM and $S_a(T_1)$; standard deviation (efficiency) of (c) MIDR, and (d) σ_D for the considered IMs; and relative sufficiency measure for alternative IMs with respect to the IM characterized by the lowest standard deviation, for (e) MIDR, and (f) σ_D.

frame. This is also observed in Figure 4.7(d), where the most efficient IM, in this case, accounts for all five periods [i.e., $(T_i)_4$] considered in this dissertation. However, a reverse effect is observed in Figure 4.6(c) (i.e., MIDR for the 4-story model), in which, considering more periods in I_{Np} result in higher values of s and this increase in the s-value is more obvious with increasing values of α.

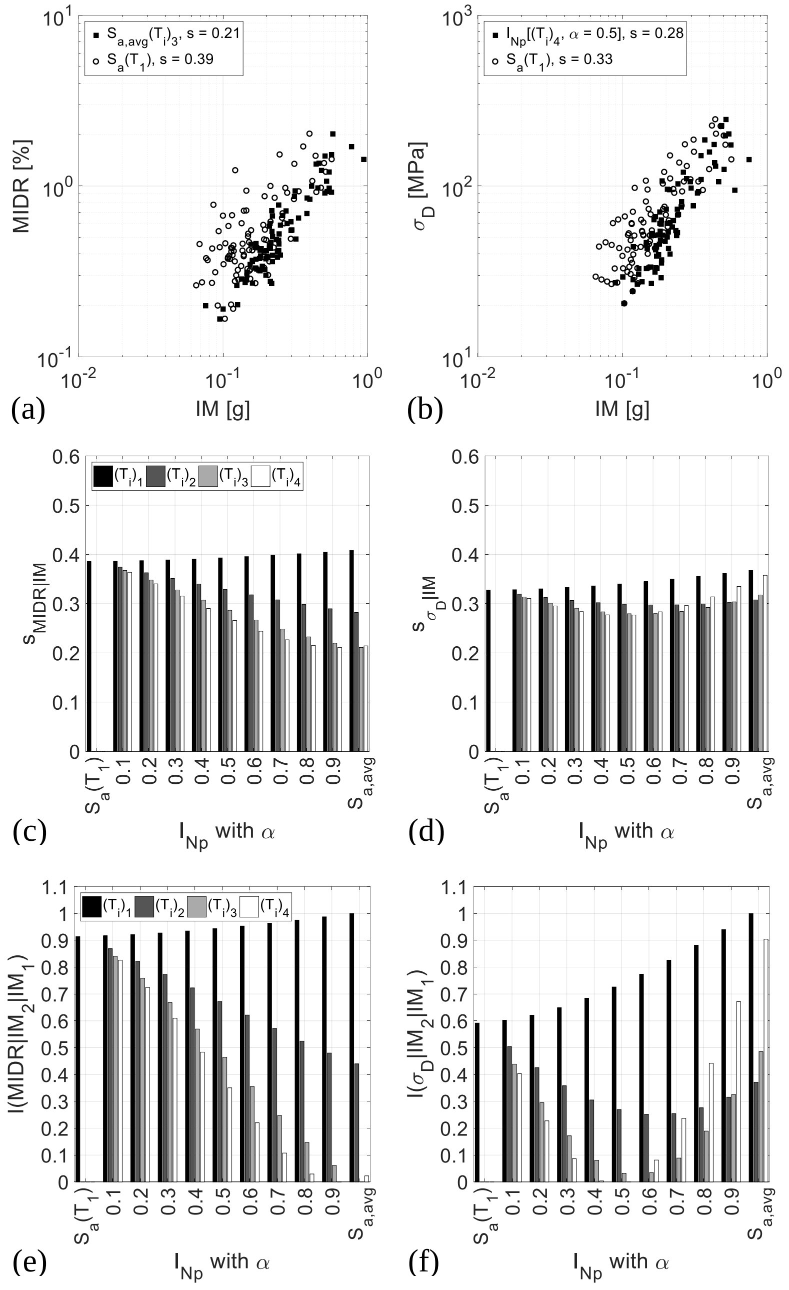

Figure 4.7: Results of optimal IM selection for the 20-story case-study frame: scatter plots of (a) MIDR, and (b) σ_D versus optimal IM and $S_a(T_1)$; standard deviation (efficiency) of (c) MIDR, and (d) σ_D for the considered IMs; and relative sufficiency measure for alternative IMs with respect to the IM characterized by the lowest standard deviation, for (e) MIDR, and (f) σ_D.

Based on the observations from the efficiency tests discussed above, general trends may be highlighted between the considered IMs [i.e., both the state-of-practice IM, $S_a(T_1)$, and spectral shape-based IMs] and the two considered EDPs. For high-rise SMRFs (e.g., 20-story frame model assessed in this dissertation), higher dynamic modes (and elongated period) are important to properly capture structural response and seismic demands. This aspect, coupled with the force-controlled nature of WCS connections, results in high efficiency of the selected optimal IMs. In fact, seismic demands in these connections tend to saturate with increasing ground-motion intensity, because other elements in the structure (i.e. beams) yield, thereby limiting the force in the splices. As a result, adding up to four modes into I_{Np} is beneficial for enhancing its efficiency, considering both EDPs. The α-values of efficient IMs (I_{Np}) for MIDR and σ_D are 1.0 and 0.5, respectively; this also indicates that the contribution of these higher modes (and elongated period in the case of MIDR) is crucial for both EDPs. In fact, if α-value approaches one (and is greater than 0.5), it means that the effects of higher dynamic modes and elongated period [represented by $S_a(T_i)$ and $S_a(1.5T_1)$, respectively] on I_{Np} are equally important to $S_a(T_1)$. In the case of mid-rise SMRFs (e.g., the 4-story frame model assessed in this dissertation), the prediction of MIDR is obviously not influenced by higher modes (or elongated period) and $S_a(T_1)$ may be considered as an efficient IM. However, the most efficient IM for σ_D includes three dynamic modes and has an α-value of 0.9, which is quite consistent with the findings for the 20-story frame model. Findings from this dissertation may have general implications for other force-controlled elements as well.

In general, these findings are consistent with those of Eads et al. (2015, 2016), Kazantzi and Vamvatsikos (2015), Kohrangi et al. (2016a), among others, although all those studies just investigated global performance indicators (e.g., MIDR) rather than local ones (e.g., column splice demand) and collapse fragility.

4.5.1.2 Results of IM relative sufficiency tests

As discussed above, cloud analysis (Section 4.3.3) is used throughout the chapter, facilitating the computation of the relative sufficiency metric for the considered IMs. In fact, the PDF, $p[\mathrm{EDP} = edp|\mathrm{IM}]$ in Eq. (4.4) can be calculated as follows, using a lognormal distribution with the parameters (i.e., a, b, s) defined through the cloud analysis:

$$p\left[\mathrm{EDP} = edp \middle| \mathrm{IM}\right] = \frac{1}{edp \cdot s}\varphi\left(\frac{\ln\left(edp\right) - \ln\left(a \cdot im^{b}\right)}{s}\right) \tag{4.15}$$

where, $\varphi(\cdot)$ is the standardized Gaussian PDF. Therefore, the relative sufficiency measure of Eq. (4.4) can finally be rewritten as:

$$I\left(\mathrm{EDP}\middle|\mathrm{IM}_2\middle|\mathrm{IM}_1\right) \cong \frac{1}{N_{\mathrm{rec}}}\sum_{i=1}^{N_{\mathrm{rec}}} \log_2 \frac{s_1}{s_2}\frac{\varphi\left[\left(\ln\left(edp_i\right)-\ln\left(a_2\cdot im_{2,i}^{b_2}\right)\right)\big/s_2\right]}{\varphi\left[\left(\ln\left(edp_i\right)-\ln\left(a_1\cdot im_{1,i}^{b_1}\right)\right)\big/s_1\right]} \quad (4.16)$$

where, a_1, b_1, s_1 are the cloud parameters corresponding to IM_1, while a_2, b_2, s_2 are the cloud parameters for IM_2, and the other parameters are those of Eq. (4.4).

Figures 4.6(e)–(f), and Figures 4.7(e)–(f) present the absolute value of the relative sufficiency metric for all the 41 considered IMs (in terms of MIDR and σ_D) and both case-study frames – note that the actual sign of $I(\mathrm{EDP}|\mathrm{IM}_2|\mathrm{IM}_1)$ is negative, i.e., any IM_2 would provide less information compares to IM_1; also, $I(\mathrm{EDP}|\mathrm{IM}_2|\mathrm{IM}_1)$ values are normalized with respect to the maximum value for facilitating the plotting. In each figure, the reference IM_1 is chosen as the one corresponding to the lowest s value from the regression study [as also indicated in Figures 4.6(a)–(b), and Figures 4.7(a)–(b)]. According to all the figures, the IMs associated with the highest efficiency are also those characterized by the highest (relative) sufficiency.

4.5.1.3 Discussion on hazard computability of selected optimal IMs

As described in Section 4.2.1.4, the last criterion for the selection of optimal IMs is hazard computability. For this criterion, the conventional IM employed in this dissertation, $S_a(T_1)$, has obvious advantages over the other advanced IMs considered as numerous attenuation laws (or GMMs) and hazard maps have been developed for $S_a(T_1)$, for various periods of engineering interest. In practice, the derivation of GMMs is still possible for I_{Np} and $S_{a,avg}(T_i)$ (i.e., the particular case of I_{Np} with $\alpha = 1$), through either direct or indirect methods. For instance, Bojórquez and Iervolino (2011) showed that GMMs for advanced, spectral-shape-based IMs can be easily derived through probabilistic combinations of the available GMMs for $S_a(T_i)$ (i.e., indirect method) based on the assumption of jointly (log-) normality of spectral ordinates; on the other side, the direct method consists of deriving new specific GMMs for spectral-shape-based IMs. For instance, Kohrangi et al. (2018) recently developed empirical attenuation laws for $S_{a,avg}(T_i)$, and the results of this study also indicate that the indirect method determines median estimates of $S_{a,avg}(T_i)$ that are identical to those obtained from the direct method. It is worth noting that the variance estimates of $S_{a,avg}(T_i)$ from two methods may not be identical, if the attenuation law for $S_a(T_1)$ and the empirical correlation coefficients among different spectral acceleration ordinates are determined from different GM record sets. To sum up, the advanced IMs accounting for the spectral shape effect are still computable, but this process (using either direct or indirect approach mentioned above) can be slightly more time-consuming, when compared with $S_a(T_1)$.

4.5.1.4 Effect of optimal IMs on WCS fracture fragility

Finally, two sets of fracture fragility functions, considering the selected optimal IMs and the mean fracture capacity (σ_C, calculated based on the equations and deterministic/nominal values of RVs discussed in Section 4.4) are presented in Figure 4.8, for the 4- and 20-story frames, respectively. The corresponding sets of fracture fragility curves for the conventional, state-of-practice IM, $S_a(T_1)$, are also plotted for comparison. Table 4.4 lists the corresponding median (μ_{IM}) and dispersion (β_{IM}) values for each fragility curve shown in Figure 4.8.

According to both Figure 4.8 and Table 4.4, the dispersions of fracture fragility functions for optimal IMs are considerably smaller than their counterparts for $S_a(T_1)$, as expected. It is obvious that the use of optimal spectral-shape-based IMs reduces the variability in the fracture fragility analysis, and therefore, can better capture the actual fracture fragility of WCS.

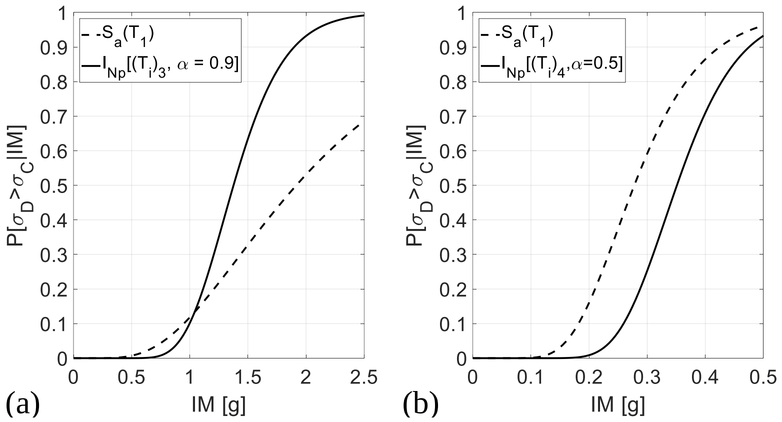

Figure 4.8: Comparison of fracture fragility curves derived based on the selected optimal IMs (solid lines) and $S_a(T_1)$ (dashed lines), for (a) Splice #1 (4-story frame) and (b) Splice #2 (20-story frame).

Table 4.4: Median (μ_{IM}) [g] and dispersion (β_{IM}) values of fracture fragility curves obtained based on the selected optimal IMs and $S_a(T_1)$ (as per Figure 4.8)

Selected IM	Splice #1 (4-story frame)		Splice #2 (20-story frame)	
	μ_{IM}	β_{IM}	μ_{IM}	β_{IM}
Optimal IM[a]	1.38	0.25	0.35	0.24
$S_a(T_1)$	1.92	0.55	0.28	0.33

[a] Selected optimal IMs for Splices #1 and #2 are $I_{Np}[(T_i)_3, \alpha = 0.9]$, and $I_{Np}[(T_i)_4, \alpha = 0.5]$, respectively.

4.5.2 Effect of GM vertical component on WCS fracture fragility

As described in Section 4.3.2.2, two sets of GMs (i.e., Scenario #1 and Scenario #2, selected from SIMBAD), each containing the 100 stronger horizontal components (between X- and Y-) and their corresponding vertical components (Z-), are used as input to perform cloud-based NLTHA. To investigate the effect of the vertical GM components on the fracture fragility of WCSs and quantify its potential increase, two sets of NLTHAs for each GM scenario are performed to assess the case-study frame models in terms of WCS stress demands (σ_D), as follow:

- Application of the selected horizontal GM components only; and
- Application of both selected horizontal and vertical GM components simultaneously.

Based on the two sets of runs, the fracture fragility curves (considering mean fracture capacity) developed for both case-study frames are shown in Figures 4.9 and 4.10, for Scenario #1 and Scenario #2 GMs, respectively. The corresponding median (μ_{IM}) and dispersion (β_{IM}) values for each fragility curve shown in these figures are summarized in Table 4.5. In order to reduce the sensitivity of the probability of fracture given IM, the optimal IMs selected in the previous subsection, i.e., $I_{Np}[(T_i)_3, \alpha = 0.9]$ for Splice #1 and $I_{Np}[(T_i)_4, \alpha = 0.5]$ for Splice #2, are used here to derive fracture fragility curves for Scenario #1. Also, these two IMs are adopted to develop fracture fragility curves for Scenario #2. Following this, a fair comparison between the two scenarios can be performed.

In general, the increase of fracture fragility can be observed in all the four cases, when the vertical component of each GM is combined with its horizontal component.

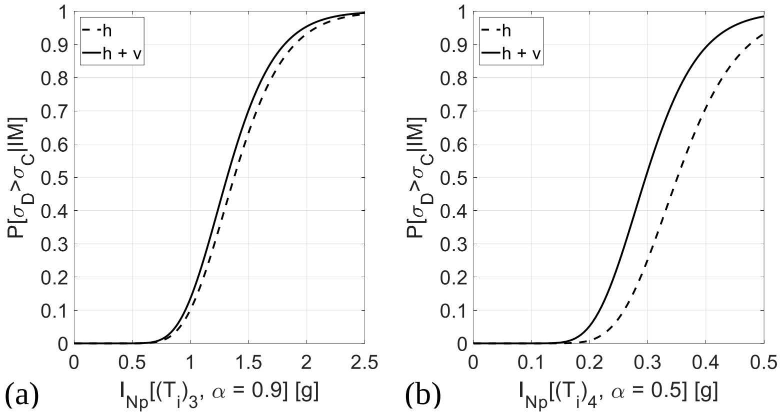

Figure 4.9: Comparison of fracture fragility curves derived in the case of horizontal components only (dashed lines) and horizontal components combined with vertical ones (solid lines) for Scenario #1 GM set, and (a) Splice #1 (4-story frame); and (b) Splice #2 (20-story frame).

However, as confirmed by inspecting all the figures, the vertical component of each GM can be considered as a 'complementary' factor further increasing σ_D, but not the main contributor to σ_D. This increase in fracture fragility of WCSs is more significant in the case of the 20-story frame compared to the 4-story frame, as expected. This reveals that the inclusion of GM vertical components may be more critical in high-rise structures (decreasing in μ_{IM} up to about 20%), as larger portion of seismic stress demands would be induced by vertical GMs.

When comparing the results between the two scenarios, the higher fracture fragility of the 4-story frame (representing mid-rise SMRF) is observed in the case of

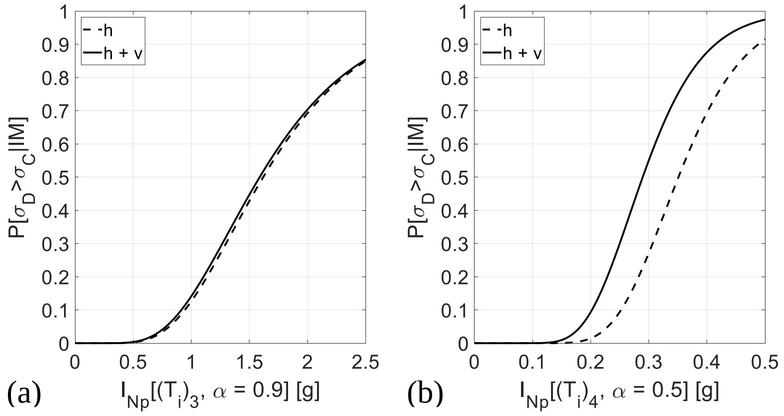

Figure 4.10: Comparison of fracture fragility curves derived in the case of horizontal components only (dashed lines) and horizontal components combined with vertical ones (solid lines) for Scenario #2 GM set, and (a) Splice #1 (4-story frame); and (b) Splice #2 (20-story frame).

Table 4.5: Median (μ_{IM}) [g] and dispersion (β_{IM}) values of fracture fragility curves obtained in the case of horizontal components only and horizontal components combined with vertical ones for Scenario #1 and Scenario #2 GM sets (as per Figures 4.9 and 4.10)

Cases		Scenario #1		Scenario #2	
		μ_{IM}	β_{IM}	μ_{IM}	β_{IM}
Splice #1 (4-story frame)	horizontal	1.38	0.25	1.62	0.42
	horizontal + vertical	1.32	0.25	1.59	0.43
Splice #2 (20-story frame)	horizontal	0.35	0.24	0.35	0.26
	horizontal + vertical	0.30	0.24	0.29	0.28

Note: optimal IMs used for Splices #1 and #2 (both scenarios) are $I_{Np}[(T_i)_3, \alpha = 0.9]$, and $I_{Np}[(T_i)_4, \alpha = 0.5]$, respectively.

Scenario #1. This is mainly due to the GM selection strategies described in Section 4.3.2.2 as Scenario #1 consists of all the strongest GM horizontal components in the SIMBAD database, which always cause the higher seismic demand in WCSs compared to Scenario #2. However, the fracture fragilities of the 20-story frame (representing high-rise SMRF) between these two scenarios are almost identical (with slight differences in dispersion). This indicates that high-rise SMRF is much more susceptible to fracture, and the fracture may occur even when it is subjected to GMs with relatively lower intensities (i.e., Scenario #2). Moreover, the largest separation between the fracture fragility for the two sets of runs is observed in Figure 4.10(b) (i.e., 20-story frame model subjected to Scenario #2 GM set). This may be explained by the fact that the strongest GM vertical components are selected for Scenario #2, and they may have comparable magnitudes to their horizontal components. Hence, a larger increase in σ_D can be attributed to the vertical motions; this is in consistency with the findings of previous studies (e.g., Papaleontiou and Roesset 1993).

4.5.3 Effect of fracture capacity uncertainty on WCS fracture fragility

To investigate the effect of fracture capacity uncertainty on WCS fracture fragility, the seismic stress demand distribution corresponding to the set of 100 strongest horizontal components of GMs (described in Section 4.3.2.1) is considered. Following Section 4.4, the uncertainty of σ_C (e.g., Figure 4.5) is assessed through (plain) Monte Carlo simulation, taking into account all the considered RVs (characterized by their nominal values and statistical distributions) specified in the FEFM-based approach proposed by Stillmaker et al. (2016).

Figure 4.11 shows the individual fracture fragility curves (with a range of median optimal-IM capacities, represented as grey lines) according to 1,000 realizations of the fracture capacity through Monte Carlo simulation, for the 4- (Splice #1) and 20-story (Splice #2) case-study frames, respectively. The same figures also illustrate the mean, the 5th and 95th percentile fracture fragility curves derived from the uncertainty simulation. In addition, a fracture fragility curve considering the mean of all the simulated σ_C values is also plotted for comparison. As expected, the difference between the mean fracture fragility curve derived from the uncertainty analysis and the one accounting for the mean value of σ_C are negligible. However, slightly higher dispersion (i.e., about 10% increase in β_{IM}) is found in the mean fracture fragility curve (solid line), which provides a smeared representation (Bakalis and Vamvatsikos 2018) of dispersion containing information on both the record-to-record variability (i.e., fracture stress demand) and the fracture capacity variability (e.g., in Figure 4.5, CoV of σ_C is about 17% for both splices). On the other hand, the (smaller) dispersion of the fracture fragility curve corresponding to the mean value of σ_C can only represent the uncertainty caused by various GM records used, since a discrete fracture capacity value (rather than an amount of equiprobable σ_C data) is considered.

Moreover, both cases show significant scatter in the fracture fragility of WCSs when stress capacity uncertainty is considered. Given this large variability of the fracture fragility, all the RVs considered in the employed FEFM-based approach

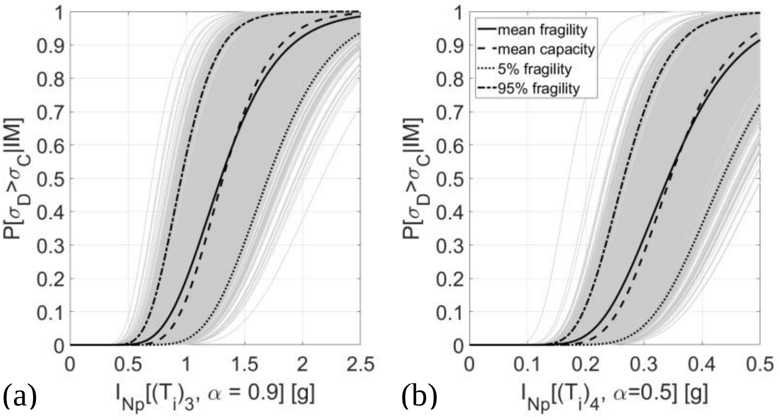

(a) (b)

Figure 4.11: Fracture fragility curves considering uncertainty in fracture capacity of WCSs for (a) Splice #1 (4-story frame); and (b) Splice #2 (20-story frame).

should be carefully examined to identify their contribution to the total uncertainty in fracture capacity. Due to this significant uncertainty in the determination of σ_C, a more conservative value (rather than the mean value) of fracture capacity of WCS may be recommended, especially in the design practice. As an example, in the original paper of Stillmaker et al. (2016), detailed reliability analysis has been conducted to calibrate the resistance factors added in design equations that can provide an adequate margin of safety for new construction of mid- to high-rise SMRFs with WCSs.

4.6 Summary

This chapter investigated some issues affecting seismic demand and capacity uncertainties in the assessment of fracture fragility of WCSs. This led to refined (simulation-based) fracture fragility assessment for WCS connections, utilizing state-of-the-art research tools and putting them into a coherent and harmonized overall approach that is practical to implement.

Based on 4- and 20-story case-study SMRF models and various sets of GMs, several conclusions can be drawn as follow:

- The spectral shape-based scalar IMs [i.e., I_{Np} and its special case, $S_{a,avg}(T_i)$, investigated in this chapter] are generally recognized as better proxies for probabilistic seismic demand analysis in terms of MIDR and σ_D, because they are usually characterized by higher efficiency and relative sufficiency, compared to $S_a(T_1)$. In terms of hazard computability criterion, these advanced IMs are computable although the process can be more time-consuming. Moreover, the performance of I_{Np} is sensitive to the values of α-parameter, and the effect of higher structural modes and elongated period. In the context of WCS connections, accounting for higher-mode effects on WCS seismic demands, through ad-hoc IMs, is particularly useful, since the stresses in these components saturate (at low intensity levels) as the ductile elements (beams in the case of SMRFs) deform inelastically. According to this chapter, optimal α-values and number of structural modes are usually structure-specific, although general trends can be observed depending on the type of EDP investigated.

- Accounting for the vertical components simultaneously with the corresponding horizontal components of GMs increases the fracture fragility of WCSs, through an increase of the peak tensile stress in WCSs (σ_D). This increase is moderate in the 4-story case-study frame but more considerable in the 20-story case-study frame. If the amplitudes of the GM vertical components are comparable to their horizontal components, a significant increase in fracture fragility can be observed, and vice versa.
- Through the use of an advanced FEFM-based approach (Stillmaker et al. 2016) combined with a detailed uncertainty characterization, the variability in WCS fracture capacity is first assessed; the corresponding fracture fragility is then derived for the selected case-study frames/splices. Fracture fragility is significantly affected by the resulting capacity uncertainty, showing a considerable scatter around the mean fracture fragility. This suggests that a more conservative value (rather than the mean value) of fracture capacity of WCS may be considered in practical fracture risk assessment applications. In addition, a roughly 10% increase in the dispersion of mean fracture fragility curves is found when the uncertainty of WCS fracture capacity is properly considered in the fracture fragility assessment.

The main limitations of this chapter are in the simulation methodology used for both demand and capacity analysis. Due to the use of fiber sections (with a bilinear kinematic hardening law) for steel beams and columns, collapse is not directly simulated in the models. However, it is assumed that the non-simulation of collapse has limited effects on the demand assessment of WCSs (as discussed in Section 4.3.1). Although the fracture simulation of WCS may be considered as an energy-based issue, the primary assumptions made in the dissertation are that (1) WCS fracture is solely controlled by longitudinal stress (uniaxial tension) in the flange; and (2) the history effects (e.g., cyclic degradation on the material toughness that associated with fatigue) are modest, because the inelastic deformations/cyclic plastic strain in the WCS region are limited.

Chapter 5

Fracture Risk Assessment of Pre-Northridge Welded Column Splices in Near-Fault Regions

Adapted from **Song, B.**, and Galasso, C. (2020). “Directivity-Induced Pulse-Like Ground Motions and Fracture Risk of Pre-Northridge Welded Column Splices.” *Journal of Earthquake Engineering* (in press).

5.1 Introduction

In near-fault regions, earthquake-induced ground motions (GMs) are often characterized by a large-amplitude and long-duration pulse in the first portion of the ground velocity time history; such a pulse is more commonly observed in the fault-normal orientation than the fault-parallel one. These pulse-like GMs are caused primarily by forward directivity (e.g., Shahi and Baker 2011; Singh 1985), as sketched in Figure 5.1 for a simple case of a unilateral strike-slip fault: when the fault rupture propagates towards the site and the rupture velocity is close to the shear-wave velocity, a high-amplitude pulse can be generated due to the constructive interference between the arrival of the seismic energy from the rupture and the seismic wavefront (Somerville et al. 1997). Such a pulse has an occurrence probability that depends upon the site-to-source geometry (e.g., Iervolino and Cornell 2008), and a peculiar pulse period that may be modeled as a function of the earthquake magnitude (e.g., Chioccarelli and Iervolino 2010). These directivity-induced pulse-like GMs recorded close to a fault rupture are distinct from the ordinary (i.e., non-pulse-like) GMs.

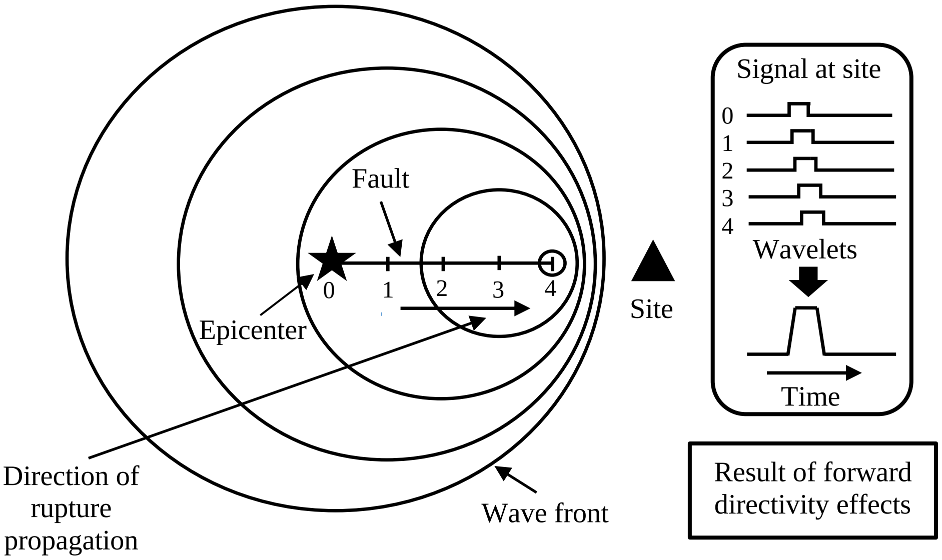

Figure 5.1: Schematic illustration of directivity effects on a site towards the direction of rupture propagation (adapted from Singh 1985).

Moreover, they are unlikely to be observed at sites that are more than 10–15 km away from a fault rupture (i.e., they generally occur in the so-called near-fault or near-source regions), because the effect of forward directivity dramatically decreases with the distance from the fault as seismic waves scatter (Iervolino and Cornell 2008).

In several near-fault regions, particularly in the west coast of the US, steel moment-resisting frames (SMRFs) are a common lateral-load resisting system for earthquake resistance. Within mid- to high-rise SMRF structures, welded column splices (WCSs) are commonly used to address length/transportation constraints and/or downsizing of the column sections due to the changes in loading at higher stories of a structure (Shaw et al. 2015). Recent studies (e.g., Galasso et al. 2015) and Chapter 4 above have shown that the fracture risk of pre-Northridge WCSs subjected to ordinary GMs is relatively high due to three main issues: (1) they utilized low-toughness welds [i.e., characterized by Charpy V-Notch (CVN) values between 6.8 and 13.6 J (Chi et al. 2000)], which are much lower than the code-specified value of 27 J at −18°C [AISC (American Institute of Steel Construction) 341-16 (AISC 2016b)], resulting in significantly low fracture capacity; (2) they featured partial joint penetrations (PJP) welds with weld penetrations of around 50% of the thinner flange thickness of WCSs (Bruneau and Mahin 1990), producing a cracklike flaw in the region of low material toughness (i.e., unfused weld root); (3) they are force-controlled connections and their fracture is dominated by the tensile stress (rather than the inelastic deformation) – the expected fracture stresses, roughly in the range of 60–180 MPa [e.g., Figures 4.6(b) and 4.7(b)], are much lower than the flange yielding strength of 400 MPa mandated by AISC 341-16 (AISC 2016b). Given these issues, a refined probabilistic assessment of fracture demands and capacities of WCS connections in pre-Northridge SMRFs is of primary importance in several earthquake-prone areas, particularly for the prioritization, planning, and design of retrofitting strategies for those vulnerable connections; see Chapter 4 for a detailed discussion on these aspects.

The increased structural risk (particularly, collapse risk) due to near-fault, pulse-like GMs has been highlighted by several recent earthquakes around the world, including the 1994 M6.7 Northridge, California, the 1995 M6.9 Kobe, Japan, the 1999 M7.6 Chi-Chi, Taiwan, the 2009 M6.3 L’Aquila, Italy, and the 2016–17 Central Italy sequence (featuring events in the magnitude range between 5.5 and 6.5), among others. These earthquakes have emphasized the higher damage potential of pulse-like GMs, for instance in terms of larger elastic and inelastic displacement demands (e.g., maximum inter-story drift ratio, MIDR) compared to far-field, ordinary GMs (e.g., Chioccarelli and Iervolino 2010). In the available literature published so far, most studies comparing structural demands to pulse-like and ordinary GM records have focused on global deformations at (or near) the collapse limit state (e.g., Champion and Liel 2012; Tzimas et al. 2016). To the author’s knowledge, local engineering demand parameters (EDPs), such as stress demands, controlling the fracture of pre-Northridge WCSs, have not been properly investigated and quantified in the case of pulse-like GM records. Reliable estimation of WCS fracture fragility and risk, particularly in near-fault regions, is critical and urgent, since: (1) given their structural function, the fracture risk of WCSs has major implications for occupant safety and thus, on decisions regarding retrofit; and (2) given their location, repair/retrofit of WCSs is costly and extremely disruptive to building operations. More in general, accurate evaluation of seismic fracture risk in the near-fault region is critical for the continued improvement of building code provisions.

Therefore, this dissertation further investigates the fracture fragility and fracture risk of pre-Northridge WCSs in near-fault regions, particularly addressing the effect of pulse-like GMs due to forward directivity on the distribution/increase of WCS stress demands (denoted as σ_D). To this aim, highly detailed nonlinear fiber-section models are developed in OpenSees (Mazzoni et al. 2009) for two case-study index buildings, i.e., 4- and 20-story SMRFs featuring WCSs (Section 4.3.1 has discussed them in detail, therefore, they are not repeated in this chapter). A first record set, consisting of 91 near-fault, pulse-like GMs with varying pulse periods (denoted as T_p), is used as input for incremental dynamic analysis (IDA; Vamvatsikos and Cornell 2002). The fracture capacity (denoted as σ_C) of the considered WCSs is computed through a simplified fracture mechanics-based approach derived by Stillmaker et al. (2016), also accounting for both aleatory and epistemic uncertainty affecting WCS fracture capacity (as discussed in Section 4.4). Fracture fragility curves (for ordinary records) and the GM intensity values leading to fracture as a function of T_p (for pulse-like records) are derived from the IDA results. These are then combined with state-of-the-art near-source probabilistic seismic hazard analysis (NS-PSHA) models accounting for forward directivity for a case-study scenario rupture. Six near-fault sites are considered to represent variations in site-to-source geometry and investigate the sensitivity of fracture risk to source-to-site distance. Following this, earthquake-induced fracture risk of pre-Northridge WCSs in the near-fault region is assessed and the results are critically discussed. Finally, findings from this chapter are summarized.

5.2 Datasets of pulse-like and ordinary GMs

The fracture risk of WCSs depends on the fracture probabilities (i.e., fracture fragility) quantified from pulse-like and ordinary GMs and their probabilities of occurrence (i.e., the seismic hazard at a given site); a detailed description of the probabilistic framework employed in this chapter is provided in Section 5.4. Furthermore, this dissertation also aims to compare the earthquake-induced fracture fragility/risk at near-fault sites featuring pulse-like GMs with that at far-field sites that are not affected by forward directivity effects. Therefore, two sets of GMs, made by pulse-like and ordinary records, respectively, are utilized here.

Specifically, a first set consisting of 91 pulse-like GMs is employed as input for nonlinear time history analysis (NLTHA). This GM set was compiled by Baker (2007) by using records from the Next Generation Attenuation database developed by the Pacific Earthquake Engineering Research (PEER) Center. All the records in the considered set have been rotated to the fault-normal direction. The pulse periods of these records, ranging from 0.4 s to 12.9 s, were detected and quantified through wavelet analysis, and the associated peak ground velocities (PGV) are greater than 30 cm/s. The full list of this set can be found in Baker (2007). The moment magnitudes (M_w) of these records vary between 5.0 and 7.6. It is worth noting that the source-to-site distance (R_s) was not considered as a selection criterion, and therefore, it ranges from 0.10 to 102 km. However, all the records show velocity pulses early in the time histories; some of the identified pulses may be generated by other seismic site effects, such as the sedimentary basin effect, rather than near-fault directivity. However, due to the limited number of available pulse-record in empirical databases, all the 91 records in the set are considered in this chapter to make the pulse-like GM set, with the assumption that the large velocity pulses due to different geological mechanisms will induce similar structural demands/effects. It should be acknowledged that, although some other researchers have assembled datasets of pulse-like records (e.g., Mavroeidis 2003; Somerville 2003), also considering pulses at arbitrary orientations (not just the fault-normal one) in multicomponent GMs (Shahi and Baker 2014), this GM set is employed here as (1) the wavelet-analysis approach is quantitative, systematic and therefore easily reproducible for pulse identification (Champion and Liel 2012); (2) the same datasets have been used by similar studies investigating different structural types and limit states [e.g., Champion and Liel (2012), for assessing the effect of near-fault directivity on reinforced concrete building seismic collapse risk; Tzimas et al. (2016), for assessing collapse risk and residual drift performance of steel buildings using post-tensioned SMRFs and viscous dampers in near-fault regions].

A second set of records is used in this chapter to represent ordinary GMs. They are parts of the Federal Emergency Management Agency (FEMA) P695 far-field record set [ATC (Applied Technology Council) 2009], which contains 22 record pairs, each with two horizontal components (i.e., 44 records in total). Initially, nine of these records were removed from the considered set, because they exhibit pulses in velocity time history based on the wavelet classification algorithm results (Champion and Liel 2012). Moreover, for each pair of GMs, only the component characterized by the larger peak ground acceleration (PGA) value is arbitrarily selected to reduce the computational burden (yet maintaining a statistically significant number of records for the analysis). A set of 21 records is finally used to represent generic far-field, ordinary GMs in this chapter. These GMs were recorded at sites no less than 10 km away from the fault rupture and their moment magnitudes (M_w) range from 6.5 to 7.6. The selected far-field GM set used here is structure-type (i.e., period) and site-hazard independent as no specific spectral shape (and corresponding period range) was considered in the record selection. However, similar to the findings from Baker and Cornell (2008a) and Champion and Liel (2012) for collapse risk assessment, a significant impact caused by spectral shape on the fracture risk assessment (e.g., with respect to relevant fracture fragility curves) has been observed. Therefore, the spectral-shape adjustment recommendations by Haselton et al. (2011) are applied here to account for the specific spectral shape of the far-field GMs. This aspect is further discussed in Section 5.3.1.

5.3 Fracture evaluation approach

As discussed above, fracture risk of each case-study SMRF/WCS is evaluated through IDA (Vamvatsikos and Cornell 2002), which is suitable for performing probability-based seismic demand assessment for a wide range of seismic hazard intensities. In IDA, the numerical building model is subjected to a selected earthquake record while tracking the response of the structure (e.g., story displacements, floor accelerations, etc.). Each input GM (in each GM set described in Section 5.2) is scaled in amplitude to increasing levels of intensity until fracture occurs (in the selected WCSs, see Figure 4.2). This process is repeated for all earthquake records and each frame/WCS connection. In this chapter, the considered GM intensity measure (IM) for the scaling is the 5%-damped spectral acceleration at the fundamental period of each case-study SMRF, denoted as $S_a(T_1)$ (simply S_a hereinafter). As discussed in Chapter 4, more advanced, spectral-shape-based IMs are generally recognized as better proxies for probabilistic seismic demand analysis of WCSs in terms of MIDR and σ_D, as they are usually characterized by higher efficiency and relative sufficiency compared with S_a. However, the use of such advanced IMs, particularly when performing site-specific PSHA, would require cross-IM correlation models that are explicitly developed for pulse-like GMs. To the author’s knowledge, there are no such models explicitly accounting for pulse-like GMs. From a more general perspective, as discussed in detail in Kazantzi and Vamvatsikos (2015), within a risk assessment framework, the reduction in response dispersion gained by a more efficient IM, does not reduce the overall risk variability: part of the variability is simply shifted to a different level within the risk assessment, and in particular to the seismic hazard curve definition. Thus, given the final aim of this chapter (e.g., quantifying WCS fracture risk in near-fault conditions), the use of S_a, for which various PSHA models/approaches – also including near-source effects – have been developed, seems appropriate.

The monitored demand parameter (i.e., the selected EDP) is the peak tensile stress (σ_D) in the flange of the selected WCSs. Fracture occurs when σ_D exceeds the stress capacity (σ_C) for the WCSs of interest (i.e., Splice #1 and Splice #2 in this dissertation, see Figure 4.2). To determine σ_C, analytical equations based on a fracture mechanics-based approach proposed by Stillmaker et al. (2016) are adopted. The details of the approach and the selected WCSs have been discussed in Section 4.4. The mean (deterministic) values of the fracture capacity for Splices #1 (4-story) and #2 (20-story) are calculated as 113.6 MPa and 108.2 MPa, respectively. It should be noted that the uncertainty in the computation of σ_C can be quite significant [See Chapter 4 and Stillmaker et al. (2016) for details]; therefore, a more conservative value (instead of the mean value) should be considered as nominal WCS stress capacity, particularly at the design stage.

Additionally, a global EDP (i.e., MIDR, to inform global collapse of SMRF models) is also monitored for each model and each GM record. All the observed results show that the fracture criterion (i.e., $\sigma_D > \sigma_C$) is always violated at low S_a levels, before the observed MIDR values reach a conventional 10%-threshold for global collapse (or any numerical dynamic instability is noted). Consequently, it is assumed that there is no need to account for global collapse cases in estimating seismic fracture.

Statistics from the IDA results are used to derive fracture fragility relationships, defining the probability of fracture as a function of the hazard intensity. Such fracture fragility curves are defined by the median (denoted as μ_{IM}) and dispersion (denoted as β_{IM}) of the GM spectral intensities at which fracture occurs in the IDA [named as fracture $S_a(T_1)$ in the following sections], assuming a lognormal distribution. The computed β_{IM}-values provide a direct measure of the dispersion in the analysis results;

such a dispersion is the result of the variability in GM characteristics. Capacity uncertainty, as discussed above (and in greater details in Chapter 4), is especially important for predicting WCS fracture. For the analysis results provided herein, the record-to-record (aleatory) variability and the capacity (aleatory and epistemic) variability are assumed to be lognormally distributed and independent, such that the total variability is given by the square root of the sum of the squares (SRSS). In particular, as demonstrated in Section 4.5.3, uncertainty in σ_C leads to a 10% increase in the computed β_{IM} values due to record-to-record variability; this increase is, therefore, assumed in this chapter for developing fracture fragility curves. A number of researchers are also working to improve predictions of modeling uncertainties for different types of structures, including SMRFs. These estimates of modeling variability would change the absolute value of the fracture risk assessments but would not significantly affect the relative comparison among different buildings and sites.

5.3.1 Fracture evaluation under ordinary records

As mentioned in Section 5.2, the records from the far-field GM set (i.e., the ordinary records) were selected without any consideration of spectral shape (for a target site). Therefore, a scaled record may not have similar spectral-shape features as a large, rare GM (Luco and Bazzurro 2007), and scaling of records in this set may introduce a bias in the fracture assessment results. To measure the distinct spectral shape of a given GM, the parameter epsilon (denoted as ε), has been proposed by Baker and Cornell (2005). Specifically, ε is defined as the number of logarithmic standard deviations between the observed spectral acceleration value (of a given record) and the median value estimated from a ground motion model (GMM) for a specified structural period, earthquake magnitude, source-to-site distance, fault type, etc. Given the fact that the ordinary GM set used in this chapter is approximately epsilon-neutral (Haselton et al. 2011), and the large and rare records (i.e., at low mean annual frequency of exceedance) are all positive-epsilon (Baker and Cornell 2005), the practice of scaling up those records to represent severe GMs for which there is a limited number of empirical data may result in an over-estimation of the WCS stress demands on the assessed frames (Baker and Cornell 2005). This kind of bias may finally lead to an over-estimation of fracture fragility/risk of pre-Northridge WCSs.

To eliminate such biases from the GM scaling, both GM intensity (i.e., S_a) and ε should be accounted for properly. In this dissertation, the simplified method proposed by Haselton et al. (2011) is employed. Following this approach, the resulting fracture fragility curves for ordinary GMs can be adjusted to consider the spectral shape effects that are not reflected in the considered record selection. In particular, the GMM developed by Boore and Atkinson (2008) is adopted here to predict the median values of S_a for an assumed rupture/site scenario. Examples of such an ε adjustment for the fracture fragility curves of the 4-story frame (T_1 = 0.94 s) and the 20-story frame (T_1 = 2.36 s) are shown in Figure 5.2, assuming a far-field strike-slip (SS) earthquake with moment magnitude of M_w = 7, Joyner-Boore distance of R_{JB} = 50 km, and a value of averaged shear wave velocity over top 30 m (denoted as $V_{s,30}$) as 800 m/s. This scenario has been chosen to provide a fair comparison with the pulse-like case/scenarios, as discussed in the following sections.

5.3.2 Effect of velocity pulse on fracture analysis

For the near-fault, pulse-like GMs, the fracture fragility/risk assessment procedure is modified, as described below, such that the probability of fracture depends both on S_a and the pulse period of the record, T_p. As in Champion and Liel (2012), it is observed in this dissertation that, in contrast with the far-field GMs, the scaling of pulse-like records does not introduce significant biases on the fracture fragility assessment if both pulse period and spectral acceleration are considered to represent the spectral shape of the considered records. In fact, the detected T_p value for each near-fault GM shows a significant effect on the seismic fracture of pre-Northridge WCSs. Therefore,

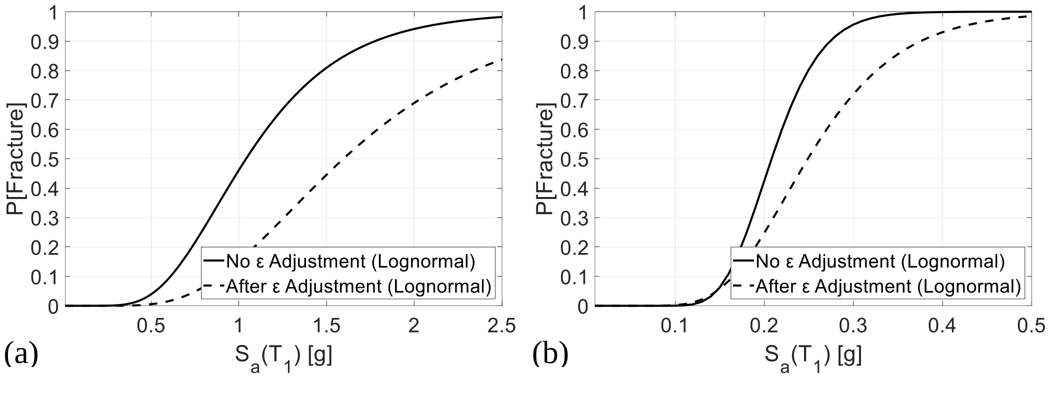

Figure 5.2: Examples of ε adjustment for the fracture fragility in the case of far-field GMs for (a) 4-story (Splice #1); and (b) 20-story (Splice #2) SMRF models.

various groups of pulse-like GMs with different T_p values can be considered to investigate the influence of T_p and to reduce the effect of ε on the fracture fragility estimates.

In particular, it has been shown by various authors (e.g., Alavi and Krawinkler 2004; Baker and Cornell 2008a; Champion and Liel 2012; Tzimas et al. 2016) that the ratio of T_p to T_1 (i.e., the fundamental period of a structure) has a critical effect on the seismic performance of buildings subjected to pulse-like records. Figure 5.3 plots this ratio (i.e., T_p/T_1 for each pulse-like record in the considered dataset) versus the associated fracture $S_a(T_1)$ (as defined above) for the 4-story and 20-story case-study SMRFs, respectively. The fracture $S_a(T_1)$ of each pulse-like record is obtained from the corresponding IDA results by interpolating between the S_a levels within which the estimated σ_D exceeds σ_C. A larger value of fracture $S_a(T_1)$ implies that the GM has to be scaled to a higher S_a level before fracture occurs (note that Figure 5.3 shows scaled records already). Moreover, following the approach of Champion and Liel (2012), the moving average of the empirical data is also plotted in Figure 5.3. This is computed by averaging the point of interest with five previous and subsequent data points (i.e., 11 data points in total). Based on the shape of moving average curve, the dependence of fracture $S_a(T_1)$ values resulting from varying T_p values can be observed.

According to the moving average curves in Figure 5.3, the highest values of fracture $S_a(T_1)$ (for both SMRF models) are obtained in the region where the pulse period (T_p) is approximately equal to (or slightly higher than) the fundamental period of structure (T_1). This observation indicates that the frame is least susceptible to

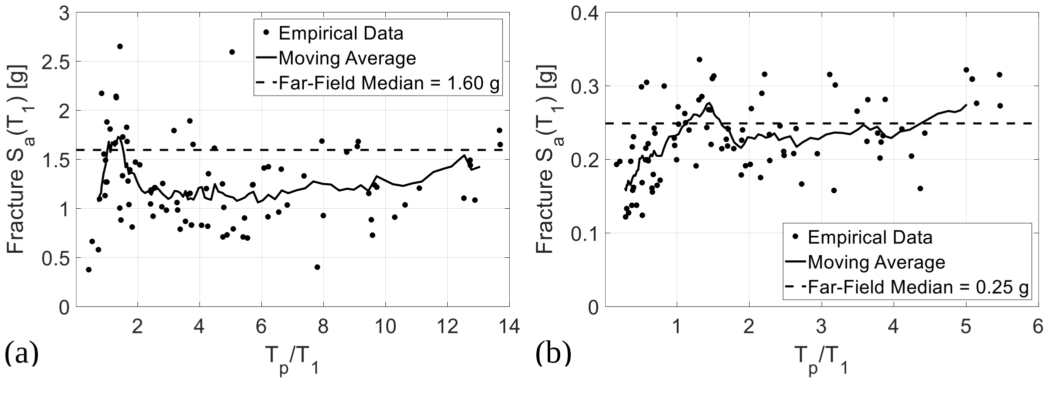

(a) (b)

Figure 5.3: Relationship between fracture $S_a(T_1)$ and T_p/T_1 for the 91 pulse-like records for (a) 4-story (Splice #1); and (b) 20-story (Splice #2) SMRF models.

seismic fracture when T_p is around T_1, which is inconsistent with the response of linear-elastic system. However, this may be explained as follows: (1) when $T_p < T_1$, the pulse period may coincide with higher modes (particularly for taller buildings) and cause a traveling wave effect over the height of the building (Iwan 1997), resulting in large displacement and axial force/stress demands in the upper stories; (2) when $T_p > T_1$, the building's effective fundamental period will elongate as damage accumulates, particularly in the case of ductile structures. The first effect is especially evident in the case of the 20-story model [where the smallest fracture $S_a(T_1)$ values are found in Figure 5.3(b)], causing an increase of the WCS stress demands for pulse-like records characterized by $T_p < T_1$. In addition, GM pulses with $T_p > T_1$ may be the most damaging in the case of the 4-story model, where the (overall) smaller fracture $S_a(T_1)$ values are indicated by the moving average curve in Figure 5.3(a). Moreover, records with $T_p >> T_1$ behave in a similar way to ordinary records as the pulse period is far away from the building's most relevant frequencies. Similarly, this effect is again especially evident in the case of the 20-story model, where the fracture $S_a(T_1)$ value tends to the far-field median fracture when $T_p >> T_1$ (in addition, for this case-study frame, very limited period elongation is observed in general).

These findings [in terms of the observed trend of fracture $S_a(T_1)$ versus T_p/T_1, as well as the shape of the moving average curves] are consistent with those by Champion and Liel (2012) for the collapse capacity [and associated collapse $S_a(T_1)$ values] of case-study reinforced concrete structures with various elastic/inelastic characteristics. However, larger differences (in terms of S_a values) between the peak and valley of the moving average curves are generally found in the seismic collapse assessment with respect to the fracture evaluation carried out in this dissertation. This may be attributed to the fact that the inelastic responses and elongation of the effective building period are more severe for a structure near collapse, while the fracture limit state in a given WCS connection is well below the intensity values corresponding to collapse.

For comparison, the median values of fracture fragilities for both SMRF models subjected to the far-field ordinary GM set (see Figure 5.2, they have been adjusted for ε) are depicted as horizontal-dashed lines in Figure 5.3. More considerable deviation between the far-field fracture $S_a(T_1)$ and the moving average curve is observed in Figure 5.3(a) (for Splice #1 in 4-story frame), compared to Figure 5.3(b) (for Splice

#2 in 20-story frame). This may be due to the significant increase in the stress demands in Splice #1 (far below its fracture capacity when subjected to the far-field GM set) because of pulse-like GMs. These may cause seismic fracture at relatively lower S_a levels (far below the far-field median level, 1.6 g). On the contrary, the high-stress demands in Splice #2 (when subjected to only far-field GMs) are already comparable to its fracture capacity at low S_a level (i.e., 0.25 g), making the decrease in fracture $S_a(T_1)$ resulting from the forward directivity effects less significant.

5.4 Fracture risk assessment including near-fault directivity

5.4.1 Fracture fragility functions and NS-PSHA

As discussed in Section 5.3, fracture fragility of pre-Northridge WCSs at a near-fault site depends on both S_a and the occurrence of a velocity pulse (with its associated T_p). By using the total probability theorem, the probability of fracture (recall the fracture criterion, i.e., $\sigma_D > \sigma_C$) incorporating the effects of near-fault directivity, for a given S_a value of x, P[Fracture|$S_a = x$], can be expressed as:

$$\begin{aligned} P\left[\text{Fracture}\middle|S_a = x\right] = {} & P\left[\text{Fracture}\middle|S_a = x, \text{Pulse}\right]\cdot P\left[\text{Pulse}\middle|S_a = x\right] \\ & + P\left[\text{Fracture}\middle|S_a = x, \text{NoPulse}\right]\cdot P\left[\text{NoPulse}\middle|S_a = x\right] \end{aligned} \tag{5.1}$$

The expression P[Fracture|$S_a = x$, NoPulse] is the probability of fracture for ordinary records (when no pulse occurs), and can be determined directly from the fracture fragility curves derived for far-field ordinary GMs (after the adjustment for ε, Section 5.3.1). The probability of fracture for pulse-like GMs, P[Fracture|$S_a = x$, Pulse], depends on the pulse period and the corresponding distribution of pulse periods at a specific S_a level of x:

$$\begin{aligned} P\left[\text{Fracture}\middle|S_a = x, \text{Pulse}\right] = \sum\nolimits_{i=1}^{\text{All } T_p} & P\left[\text{Fracture}\middle|T_p = t_i, S_a = x, \text{Pulse}\right] \\ & \cdot P\left[T_p = t_i\middle|S_a = x, \text{Pulse}\right] \end{aligned} \tag{5.2}$$

The probability of fracture for each given T_p value, P[Fracture|$T_p = t_i$, $S_a = x$, Pulse], is obtained from the relevant moving average curve plotted for each case-study frame (i.e., Figure 5.3, Section 5.3.2). The values determined from the curve are assumed to represent the median (lognormal mean) of the fracture $S_a(T_1)$ as a function of T_p. Then, a lognormal distribution can be defined to compute the probability of fracture for the given T_p and S_a. The lognormal standard deviation is assumed to be equal to the corresponding β_{IM} estimated from IDA results for $P[\text{Fracture}|S_a = x, \text{NoPulse}]$ (after the adjustment of ε and an additional 10% increase due to the fracture capacity uncertainty, as discussed in Section 5.3), i.e., $\beta_{\text{IM}} = 0.46$ for Splice #1 (4-story frame); and $\beta_{\text{IM}} = 0.32$ for Splice #2 (20-story frame).

In order to determine the other terms in Eqs. (5.1) and (5.2), near-source probabilistic seismic hazard analysis (NS-PSHA, e.g., Iervolino and Cornell 2008; Shahi and Baker 2011; Tothong et al. 2007) should be performed. NS-PSHA can be used to compute the mean annual frequency (MAF) of exceeding a spectral intensity value (denoted as $\lambda_{S_a > x}$), accounting for the potential near-fault directivity. For a single seismic fault, $\lambda_{Sa > x}$ is generally defined as:

$$\lambda_{Sa>x} = v\int_m \int_r \int_z P\left[S_a > x \middle| m,r,z\right] \cdot f_{M_w,R_s,Z}\left(m,r,z\right) dmdrdz \tag{5.3}$$

where, v is the mean annual rate of earthquake occurrence on the fault, M_w is the earthquake (moment) magnitude, R_s is the source-to-site distance, Z defines the site-to-source geometry, and $f_{Mw,Rs,Z}$ is the joint probability density function of M_w, R_s and Z. The term $P[S_a > x\,|m, r, z]$ is the probability that a specific S_a value (= x) is exceeded, given an earthquake of magnitude m at distance r and site-to-source geometry z. It depends on the probability of pulse occurrence, the distribution of possible pulse periods, and the peculiar spectral shape caused by the pulse.

In this chapter, the empirical model of Iervolino and Cornell (2008) is selected to compute the probability of a pulse occurring, $P[\text{Pulse}]$. In the case of a SS fault rupture, it depends only on three geometrical parameters as (1) the source-to-site distance, R_s; (2) the distance from the epicenter to the site measured along the rupture direction, L_s; and (3) the angle between the fault strike and the path from epicenter to the site, θ:

$$P\left[\text{Pulse}\right] = \frac{e^{0.859-0.111R_S+0.019L_S-0.044\theta}}{1+e^{0.859-0.111R_S+0.019L_S-0.044\theta}} \tag{5.4}$$

The pulse period distribution model employed here is that proposed by Chioccarelli and Iervolino (2010), and is given in Eq. (5.5) below:

$$\ln T_p = -6.19 + 1.07 M_w \tag{5.5}$$

Eq. (5.5) expresses the natural logarithm of T_p as a function of the earthquake moment magnitude (M_w) with a standard deviation of the residuals of 0.59, which is relatively large, possibly due to the impact of other perturbations (e.g., site or propagation) on the prediction of the pulse period (Chioccarelli and Iervolino 2013).

To capture the spectral shape induced by the pulse, a modifying factor suggested in Baker (2008), which has been proved as generally useful to simulate pulse-like effects (e.g., Chioccarelli and Iervolino 2013), is applied to the original GMM used in this chapter (i.e., Boore and Atkinson 2008), such that:

$$\overline{\ln\left(S_a\left(T\right)\right)} = \ln\left(S_a\left(T\right)\right) + e^{-\left(\ln\left(T/T_p\right)\right)^2} \tag{5.6}$$

where, $\ln\left(S_a\left(T\right)\right)$ is the original GMM of Boore and Atkinson (2008) and $\overline{\ln\left(S_a\left(T\right)\right)}$ is the modified GMM to account for the pulse-like features in GM. The factor of $e^{-\left(\ln\left(T/T_p\right)\right)^2}$ models a bump in the elastic spectral shape with a maximum at $T = T_p$; this semi-empirically calibrated factor represents the systematic deviation of spectral ordinates of pulse-like signals to their ordinary counterparts, around the pulse period.

To allow the combination with the fracture fragility functions described in Eq. (5.1), the NS-PSHA should be represented as $\lambda_{S_a = x}$, rather than $\lambda_{S_a > x}$, because the MAF of a given S_a (= x) is of interest. Once $\lambda_{S_a = x}$ has been calculated, hazard disaggregation can be performed to compute the probability of pulse occurrence at the S_a level:

$$P\left[\text{Pulse}\middle|S_a = x\right] = \frac{\lambda_{S_a = x,\text{Pulse}}}{\lambda_{S_a = x}} \tag{5.7}$$

According to Eq. (5.7), $P[\text{Pulse}|S_a = x]$ is defined as the ratio of the MAF of $S_a = x$ when only pulse-like records are considered to the total MAF of $S_a = x$. Note that this hazard disaggregation is required for all the considered S_a levels. Following this, the term P[NoPulse|$S_a = x$] is given as:

$$P\left[\text{NoPulse}\middle|S_a = x\right] = 1 - P\left[\text{Pulse}\middle|S_a = x\right] \tag{5.8}$$

Similarly, the term $P[T_p = t_i | S_a = x, \text{Pulse}]$ (i.e., the marginal disaggregation distribution of pulse period at each given S_a level of interest) can also be computed by considering only the case of pulse occurrence (Chioccarelli and Iervolino 2013).

5.4.2 Description of near-fault sites

In this chapter, a single characteristic M7 SS fault is considered to compare the seismic fracture risk of WCSs in SMRFs located at near-fault sites and far-field sites. Based on the median value of the Wells and Coppersmith magnitude-scaling relation (Wells and Coppersmith 1994), the length of this fault is assumed as 42 km. The mean annual rate of earthquake occurrence on the fault (denoted as v) is assumed as 0.05 and the location of earthquake epicenters is uniformly distributed along the fault. As shown in Figure 5.4, six sites with source-to-site distances of 5, 10, and 15 km at the end (i.e., "end-of-fault" sites) and midpoint (i.e., "midfault" sites) of the fault line are considered. In principle, the earthquake rupture length and its position are random variables. However, similar to the applications discussed in Chioccarelli and Iervolino (2014), the simplifying hypothesis of using fixed rupture and position (i.e., equal to the assumed fault length) is applied in this chapter. Following these assumptions, deterministic relationships among parameters for P[Pulse] estimation [i.e., R_s, L_s, and θ, as per Eq. (5.4)], rupture/fault length and position, as well as the location of

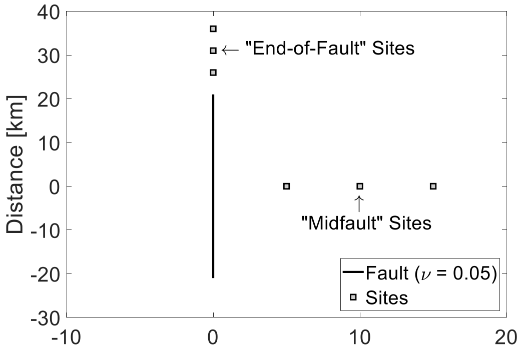

Figure 5.4: Locations of the six representative near-fault sites.

earthquake epicenter can be determined. It is worth noting that the main focus of this chapter is on comparing the fracture fragility/risk of pre-Northridge WCSs (in SMRFs) located in the near-fault sites and far-field sites, rather than investigating NS-PSHA itself. These simplifying hypotheses made above are generally acceptable if a single magnitude seismic event is considered on the assumed fault. Following this, the uncertainties involved in the hazard computations could be simulated easily (Tzimas et al. 2016).

Results of NS-PSHA for the 4-story frame (T_1 = 0.94 s) and the 20-story frame (T_1 = 2.36 s) are shown in Figures 5.5(a)–(b), respectively. The hazard disaggregation results in terms of the probability of pulse occurrence at each S_a level ($P[\text{Pulse}|S_a = x]$) for all the six considered sites are illustrated in Figures 5.5(c)–(d), for the 4-story and the 20-story frames, respectively. It can be observed that (1) the probabilities of pulse occurring at end-of-fault sites are significantly higher than those at midfault sites; and (2) the effects of varying source-to-site distance on $P[\text{Pulse}|S_a = x]$ values are significant at midfault sites, showing large separations among dashed lines (for midfault sites at 5, 10, and 15 km away from fault), while the differences of the pulse occurrence likelihood at three end-of-fault sites are limited, particularly at higher S_a levels. Figures 5.5(e)–(f) show typical distributions of pulse periods referring to specific S_a levels ($P[T_p = t_i|S_a = x, \text{Pulse}]$) for both case-study SMRFs at the 5 km midfault site. The selected S_a levels for 4- and 20-story frames are 1 g and 0.2 g, as indicated in the corresponding figures.

The NS-PSHA results, such as those shown in Figure 5.5, for the six case-study sites (Figure 5.4) offer the possibility to investigate the influence of both site-to-source geometry and structural properties on fracture risk of pre-Northridge WCSs in near-fault regions.

5.4.3 Results and discussion

The IDA results (Section 5.3) for the case-study SMRFs are used to assess the potential increase in seismic fracture fragility/risk of WCSs due to near-fault directivity and pulse effects. Applying the probabilistic methodology described in Section 5.4.1 above (to include the effects of pulse-like GMs), the fracture fragility curves for both frames at all six near-fault sites (Section 5.4.2) are developed, i.e., Figure 5.6 for Splice

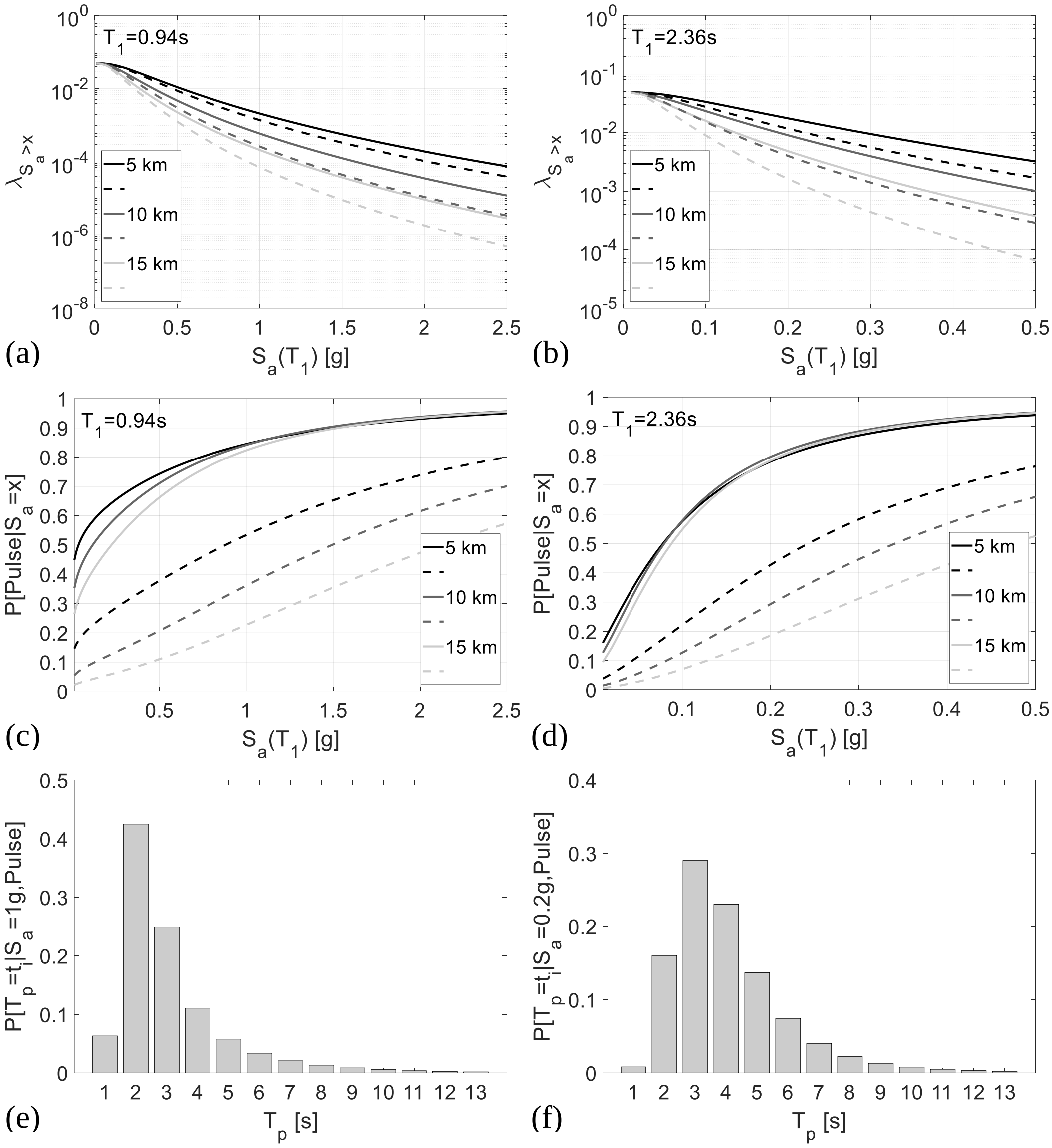

Figure 5.5: Results of NS-PSHA for the 4-story (T_1 = 0.94 s) and the 20-story frame (T_1 = 2.36 s), showing seismic hazard curves for (a) 4-story frame and (b) 20-story frame; probabilities of pulse occurrence, at midfault (dashed lines) and end-of-fault (solid lines) sites for (c) 4-story frame and (d) 20-story frame; and hazard disaggregation results in terms of pulse period distribution for (e) one hazard level of S_a = 1 g, for 4-story frame and (f) one hazard level of S_a = 0.2 g for 20-story frame, at the 5 km midfault site.

#1 in the 4-story frame and Figure 5.7 for Splice #2 in the 20-story frame, respectively. The corresponding median fracture fragility results are listed in Table 5.1. These results highlight the effect of site-to-source geometry and building parameters on the fractural fragility assessment of pre-Northridge WCSs in the near-fault region.

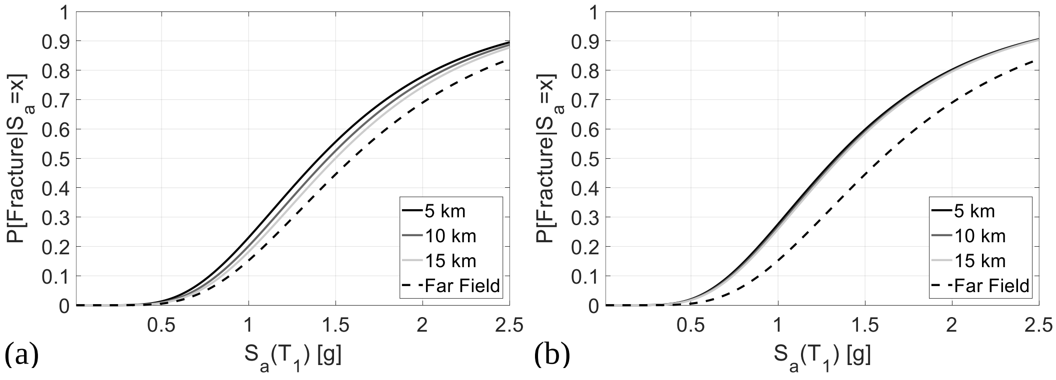

Figure 5.6: Fracture fragility functions for 4-story frame (Splice #1) at (a) three different midfault; and (b) three end-of-fault sites, and comparison with far-field fragility curves.

Looking at the 4-story frame (i.e., the mid-rise SMRF considered in this dissertation), the impact of source-to-site distance on the probability of fracture (i.e., fracture fragility for the selected WCS, Splice #1) is illustrated in Figure 5.6. As expected, higher probabilities of fracture are observed for sites closer to the fault due to the increase in pulse probability. The far-field fragility curves are also plotted in the same figures for comparison. For this particular frame located at the 5 km end-of-fault site, the near-fault directivity and pulse effects can reduce the median fragility by more than 16% from the median of the associated far-field fracture fragility curve. It is also observed that the near-fault fracture fragility curves tend to approach the far-field curve with the increase of distance from the fault rupture. As demonstrated by Champion and Liel (2012), this distance at which the near-fault curve reaches the far-field one mainly depends on the fundamental period and the nonlinear properties of the assessed building. The large separations between fracture fragility curves at the 15 km (midfault and end-of-fault) sites and the far-field ones indicate that, for this 4-story frame at 15 km sites, there are still relatively high pulse probabilities at the S_a levels large enough to cause fracture. In addition, according to Figure 5.6 and Table 5.1, the differences in terms of fracture fragility curves and their corresponding median fracture fragility values at three end-of-fault sites are moderate, because, referring to Figure 5.5(c), the pulse probabilities (for each S_a level) at these three sites are similar. Conversely, considerable separations can be found in the fracture fragility curves (and the corresponding median values) at midfault sites, due to the larger differences in pulse probabilities, such that shown in Figure 5.5(c). Moreover, because of the

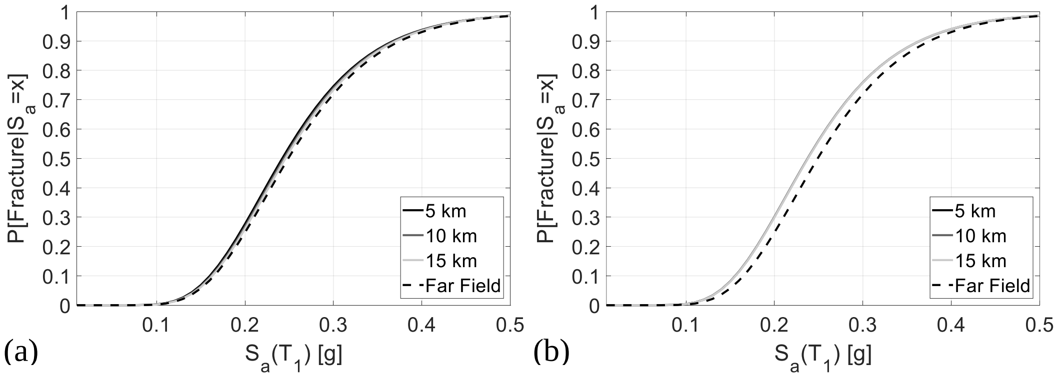

Figure 5.7: Fracture fragility functions for 20-story frame (Splice #2) at (a) three different midfault; and (b) three end-of-fault sites, and comparison with far-field fragility curves.

significantly higher pulse probabilities computed at the end-of-fault sites, their fracture fragility curves are plotted on the left-hand side to those for midfault sites. This is also confirmed in Table 5.1 that the predicted median fragility values for end-of-fault sites are smaller.

In general, similar trends are observed for the fracture fragility curves of the 20-story steel frame (i.e., the representative high-rise SMRF in this dissertation) at near-fault sites. However, only negligible differences between the various near-fault fragility curves are shown in Figure 5.7, for both midfault and end-of-fault sites. This finding is also clear when comparing the median fracture fragilities listed in Table 5.1. This may be attributable to two issues: (1) the significantly high-stress demands of 20-story frame model at low S_a level (due to overturning for instance) and relative low fracture capacity of splice #2, making it very susceptible to fracture, even at the farthest near-fault sites located 15 km away from the assumed scenario fault and the far-field site (comparing to the 5 km sites) considered in this chapter. This finding can be also confirmed when looking at Figure 5.3(b), in which the fracture $S_a(T_1)$ values obtained from the moving average curve are small (i.e., roughly between 0.16 g and

Table 5.1: Median fracture fragility results [g] for Splice #1 (4-story frame) and Splice #2 (20-story frame) at the six designated near-fault sites

Frame (WCS)	Midfault sites			End-of-fault sites		
	5 km	10 km	15 km	5 km	10 km	15 km
4-story (Splice #1)	1.405	1.457	1.499	1.331	1.346	1.356
20-story (Splice #2)	0.242	0.244	0.246	0.237	0.237	0.238

0.27 g) and close to the median of far-field fracture fragility curve (i.e., 0.25 g). It seems that the fracture fragility curves derived for Splice #2 (in 20-story frame) are largely controlled by the fracture criterion itself (i.e., the stress demands of WCS at 15 km sites/far-field site are large enough to cause the fracture failure), rather than the increase in σ_D due to the forward directivity effects and the decrease of source-to-site distance; (2) the magnitude of the near-fault pulse effects on fracture fragility depends on both the fundamental period of the structure (T_1) and the distinct pulse period distributions (Champion and Liel 2012). Given a single characteristic M7 earthquake (as assumed in this chapter), the typical range of T_p is between 2 and 6.6 s [calculated from the model of Eq. (5.5) with its uncertainty, also see Figure 5.5(f) as an example], with a modal value of about 3 s. In the case of the 20-story frame with T_1 = 2.36 s, the structural response may be dominated by pulses with T_p/T_1 ratio between 1 and 3, with little impact from the higher-mode region of response [where the smallest fracture $S_a(T_1)$ values exist]. Referring to Figure 5.3(b), the corresponding fracture $S_a(T_1)$ values in this T_p/T_1 ratio range vary around (and close to) the far-field median. These two issues result in the similar probabilities of fracture computed for the pulse-like and far-field GMs, and finally lead to almost the same results for near-fault fracture fragility curves at different sites [according to Eqs. (5.1)–(5.2)]. It is worth noting that the slight differences in median fracture fragility values (at six near-fault sites) are mainly due to the various pulse probabilities for these sites [Figure 5.5(d)].

Furthermore, two additional metrics, i.e., (1) the probability of fracture in 50 years (the typical design life of a generic building, P[Fracture in 50 years]) and (2) the return period for fracture (in years), for each selected WCS are also calculated to directly show the fracture risk of WCSs at near-fault sites. The former is determined by assuming a Poisson distribution of earthquake occurrences as follow:

$$P\left[\text{Fracture in 50 years}\right] = 1 - e^{-\lambda[\text{Fracture}]\cdot t} \tag{5.9}$$

where, t is the time in years and λ[Fracture] is the MAF of fracture. The calculation of λ[Fracture] is conducted by probabilistic seismic demand analysis (PSDA), as shown in Galasso et al. (2015). In this dissertation, PSDA combines a seismic hazard curve in terms of S_a for each designated site (computed through NS-PSHA) with the fragility results from IDA, i.e., $P[\text{Fracture}|S_a = x_i]$ of Eq. (5.1), the probability of fracture given a level of S_a. This PSDA approach is again an application of the total probability theorem. Adapted to the specific situation of WCSs, λ[Fracture] can be converted into a discrete summation (for numerical calculation), expressed as:

$$\lambda\left[\text{Fracture}\right] = \sum\nolimits_{\text{all } x_i} P\left[\text{Fracture}\middle|S_a = x_i\right] \cdot \left|\Delta\lambda_{S_a}\left(x_i\right)\right| \tag{5.10}$$

More specifically, $P[\text{Fracture}|S_a = x_i]$ can be obtained from the site-specific fracture fragility curves (i.e., Figures 5.6 and 5.7), and $|\Delta\lambda_{S_a}(x_i)|$ is the MAF of a given S_a value ($= x_i$). It can be approximately computed from the MAF of exceedance of each $S_a = x_i$ [i.e., $\lambda_{S_a > x}$ of Eq. (5.3)] and the corresponding site-specific GM hazard curve [i.e., Figures 5.5(a)–(b)], in the form that $|\Delta\lambda_{S_a}(x_i)| = |\lambda_{S_a > x}(x_i) - \lambda_{S_a > x}(x_{i+1})|$. Following this, the latter metric of fracture risk (i.e., the return period for fracture) can be easily computed as the reciprocal of λ[Fracture]. The results of such calculations for both Splices #1 and #2 at all the six (midfault/end-of-fault) sites are presented in Table 5.2.

As expected, a clear trend can be observed: the fracture risk of these two selected pre-Northridge WCSs in the 4- and 20-story SMRFs at near-fault sites increases when the source-to-site distance decrease, due to near-fault directivity and pulse effects. For Splice #1 (4-story frame), the computed P[Fracture in 50 years] values are 5.26% and 8.73% at the closest (i.e., 5 km) midfault and end-of-fault sites, respectively. They are roughly 15 and 7 times higher than their counterparts at the most distant near-fault sites (i.e., 15 km). Similar results are found for Splice #2 in the 20-story frame, with a six- and a three-time rise in terms of fracture probabilities in 50 years for the 5-km and 15-km sites located at the midpoint and the end of the fault line, respectively. Moreover, Table 5.2 also indicates the decreased return periods (in years) with sites

Table 5.2: Comparison of two metrics of fracture risk for Splice #1 (4-story frame) and Splice #2 (20-story frame) at six designated near-fault sites: probability of fracture in 50 years [%] and return period for fracture (in years)

Frame (WCS)	Metric	Midfault sites			End-of-fault sites		
		5 km	10 km	15 km	5 km	10 km	15 km
4-story (Splice #1)	P[Fracture in 50 years]	5.26	1.15	0.35	8.73	3.03	1.24
	Return period for fracture	926	4340	14417	548	1627	3991
20-story (Splice #2)	P[Fracture in 50 years]	30.49	12.54	5.49	41.87	26.21	15.67
	Return period for fracture	137	373	886	92	165	293

approaching the fault rupture. The return periods for fracture at 5-km sites vary by a factor of about 1/16 to 1/3 over those estimated for 15-km sites.

Comparing the fracture risk at each of the equidistant midfault and end-of-fault sites for the same frame, the larger values of the fracture probability in 50 years and the lower values of the return period for fracture are found at the end-of-fault sites. This is mainly because the probabilities of pulse-like GM occurrence, which depends on the site-to-source geometry, are higher at the end-of-fault sites [refer to Figures 5.5(c)–(d)]. The rupture directivity is towards these sites, in terms of the site-to-source geometry considered in this chapter (Shahi and Baker 2011). In addition, it is also observed that the fracture risk is largely affected by the effects caused by the source-to-site distance, compared with the relative position of the site with respect to the fault axis (i.e., midfault or end-of-fault). It seems that the distance to the fault rupture (for a single strike-slip fault) is more critical than the other parameters characterizing site-to-source geometry to assess the fracture risk of WCSs.

According to Table 5.2, it is also interesting to point out that the increase in the fracture risk (with the decrease of source-to-site distance) of Splice #2 (20-story frame) is also significant, although the fracture fragility of 20-story frame derived from three near-fault locations (at either midfault or end-of-fault sites) are very similar. This is mainly because the fracture risk, represented by MAF of fracture [Eq. (5.10)], is not only a function of fracture fragility but is also related to the MAF of exceeding for each S_a level [see site-specific seismic hazard curves for the 20-story SMRF, i.e., Figure 5.5(b)]. Moreover, the return periods for fracture of Splice #2 at all the near-fault sites (except for the 15-km midfault site) are unacceptably low, comparing to the return period of the design earthquake (i.e., 475 years). This inspection reveals that WCSs in the 20-story frame (or some other high-rise SMRFs) may be at an extremely high risk of fracture, due to a combination of large fracture probabilities and high MAF of exceedance at low S_a levels. As emphasized by Galasso et al. (2015), the fracture of a WCS does not necessarily lead to collapse or safety loss, since it also depends upon several other factors, such as building configuration (i.e., redundancy). However, based on the general presumption that WCS fracture is highly undesirable because it is likely to damage the crucial load-carrying element in a structure (i.e., column), these findings may warrant some consideration of retrofit strategies for pre-Northridge WCSs installed in mid- to high-rise SMRFs in any near-fault regions.

5.5 Summary

This chapter investigated the effects of near-fault directivity on the fracture risk of WCSs, through NLTHA of two case-study frames (i.e., 4-story and 20-story SMRFs featuring WCSs). A suite of 91 near-fault, pulse-like GMs (with varying T_p) and a set of 21 far-field, ordinary earthquake records were used to perform IDA. The results of the IDA were then combined with NS-PSHA to evaluate the fracture risk including pulse effects at six designated near-fault sites for a case-study scenario fault rupture.

Based on IDA results for the pulse-like records, the seismic fracture of WCSs in the near-fault region is mainly controlled by the ratio between the pulse period of a given GM and the fundamental period of the assessed structure (i.e., T_p/T_1). Certain pulse-like GMs, characterized by T_p values different than T_1 may cause a considerable decrease in terms of fracture $S_a(T_1)$ relative to the results obtained from the ordinary records, and therefore, are more critical for fracture risk assessment in near-fault regions.

The probabilistic fracture risk assessment results, in terms of the fragility curves, the probability of fracture in 50 years, and the return period for fracture (derived from MAF of fracture), indicate that the fracture risk experiences a considerable increase, when the near-fault directivity and pulse effects are properly considered in the NS-PSHA and the structural response simulation. More specifically, the fracture risk of WCS substantially increases as the source-to-site distance decreases. Moreover, considering any specific frame, the influence of the distance from fault rupture on the fracture risk is more significant to the effect caused by the relative site location to the fault axis. In particular, very high fracture susceptibility for Splice #2 in the 20-story SMRF is found in this chapter and indicated by a significantly low return period for fracture (< 475 years for the return period of design earthquake). This highlights that the design of retrofitting strategies for pre-Northridge WCSs in high-rise steel structures located in near-fault regions may be highly desirable.

In addition to the limitations discussed in the previous chapter (Section 4.6), the main limitations of this chapter are in the computation of the site-specific seismic hazard. Although the NS-PSHA models employed in this chapter explicitly considered the occurrence of velocity pulses, only a single scenario fault and one set of empirical models for NS-PSHA and GMM were used (rather than, for instance, the use of a logic-tree combination of different models/GMMs and multiple faults). As a result, while the main conceptual findings (e.g., the relative comparisons between the various metrics related to fracture risk and their observed trends with respect to the site-to-source geometry) would stand for different rupture scenarios, some variations in the absolute values of these results may be expected if other hazard characteristics would be explicitly modeled.

Chapter 6

Conclusions

6.1 Summary

This dissertation presented three separate research studies with the overall aim to advance performance-based design and assessment of two critical load-carrying connections that are commonly used in steel moment-resisting frames (SMRFs) – exposed column base plate (ECBP) and welded column splice (WCS) connections. This research work was motivated by relatively lower research attentions received for ECBPs and WCSs than the welded beam-to-column connections in the SMRFs, leaving several relevant aspects of their performance not well investigated. The main contributions provided by this dissertation are described in detail in this section, and can be initially summarized as:

- A rigorous reliability analysis was conducted for ECBPs designed as per the current code and construction/specification practice, and two new design alternatives were also proposed to overcome serious limitations of the current design approach.
- A refined performance-based fracture fragility assessment of pre-Northridge WCS was implemented to account for the seismic demand and capacity uncertainties in a coherent and harmonized overall approach.
- An expanded performance-based fracture risk assessment of pre-Northridge WCS was developed to account for the possible occurrence of pulse-like ground motions in near-fault regions and their effects on the fracture fragility and risk estimates.

This dissertation first examined the reliability that the current ECBP design code [i.e., American Institute of Steel Construction (AISC) Design Guide One (DG1, Fisher and Kloiber 2006)] is able to ensure in a rigorous manner. This reliability analysis considered 59 design scenarios corresponding to a range of loadings (gravity, wind, and earthquake) as well material grades for anchor rods. For each of the design scenarios, ECBP connections were designed as per the DG1 method and current construction/specification practice. Once designed, the reliability of each of these ECBP connections was investigated through Monte Carlo simulations that incorporate uncertainties in the geometry, materials, load, and demand/capacity models. The results indicate that the DG1 approach results in unacceptable and inconsistent probabilities of failure of the connection, with respect to (1) four limit states formulated (i.e., BF – bearing failure of the grout/concrete foundation; PC – plate failure on the compression side; PT – plate failure on the tension side; and AT – anchor rod failure on the tension side); and (2) the different loading types considered (i.e., the seismic load cases lead to lower reliability for all limit states as compared to the gravity and wind cases). A closer examination indicates that the ϕ_{bearing}-factor, which artificially reduces the flexural demands on the base plate, may cause these problems.

In response to these problems identified in the DG1 approach, two alternative design methods were suggested. Both eliminate the ϕ_{bearing}-factor in the bearing stress used for calculating flexural stresses (demand) in the base plate. One of these (termed the DG1* approach) is otherwise identical to the DG1 approach, whereas the other (termed CF – connection failure) approach, disregards the limit state of base plate failure on the compression side, since it is not likely to cause connection failure. For both these methods, ϕ_{plate}- and ϕ_{rod}-factors were calibrated to provide adequate levels of reliability across all limit states. These recommended ϕ-factors are much lower than those currently used in the DG1 approach ($\phi_{\text{plate}} = 0.6$ and $\phi_{\text{rod}} = 0.35$ for DG1* approach; $\phi_{\text{plate}} = 0.4$ and $\phi_{\text{rod}} = 0.35$ for CF approach). These lower ϕ-factors may be reasonable because the uncertainty in the *P*-*M* combinations applied at the connection level is greatly amplified at the component (i.e., the base plate or anchor rod) level. This effect is not considered in the DG1 approach, which adopts ϕ-factors used for similar components, albeit under less uncertain loads. The DG1* or CF approach may be selected (each providing adequate reliability) depending on whether compression side yielding of the base plate can be tolerated.

A refined simulation-based fracture fragility assessment for pre-Northridge WCS connections was then performed, within a performance-based earthquake engineering (PBEE) framework. Three issues that may affect the accuracy of fracture fragility assessment were rigorously investigated:

- Optimal spectral-shape-related intensity measures (IMs) were selected from 41 IM candidates to account for the higher-mode and elongated-period effects of structures on the seismic demand estimations. The results from the efficiency check indicate that the estimates of WCS stress demands have lower variability when conditional to these selected IMs. The (relative) sufficiency check also shows that these optimal IMs made the estimated WCS stress demands poorly correlated with the ground-motion parameters (e.g., magnitude and source-to-site distance). Consequently, the selected optimal IM can largely reduce the uncertainty in fracture fragility analysis (i.e., reducing the dispersion of the developed fracture fragility curves).
- When conducting cloud-based nonlinear time history analysis (NLTHA), the vertical components of ground motions (i.e., an additional uncertainty source of seismic demands) were simultaneously applied with their horizontal counterparts (i.e., conventionally considered records). The increase of peak tensile stress in WCSs (i.e., seismic demand) was clearly observed, especially when the amplitudes of vertical components are comparable to the horizontal ones. This reveals that a more accurate estimation of fracture fragility in the case of WCS requires considering the vertical ground motions.
- An advanced finite-element-fracture-mechanics (FEFM)-based model was employed to characterize the variability of fracture capacity of WCS. Two findings were reported – (1) about 10% increase in the dispersion of mean fracture fragility functions was observed when the capacity uncertainty was included; and (2) a considerable scatter around the mean fracture fragility was presented. These findings may suggest incorporating capacity uncertainty for a more accurate prediction of fracture fragility for WCS.

The probabilistic fracture fragility assessment for pre-Northridge WCSs was further combined with the state-of-the-art near-source probabilistic seismic hazard analysis (NS-PSHA). This combination allows one to estimate the effects of directivity-induced pulse-like ground motions on the fracture fragility and risk of WCSs in near-fault regions. In this assessment, two sets of ground motions (one represents far-field non-pulse-like earthquakes, whereas the other one contains pulse-like earthquake records) were employed to perform NLTHA. A case-study scenario rupture and six representative near-fault sites were used to assess the fracture fragility and risk of WCSs (with various source-to-site distances and relative positions to the fault axis). Several main findings should be recalled:

- It was found that the ratio between pulse period (T_p) of each pulse-like ground motion to the fundamental period of the assessed frame (T_1) is a good indicator to predict fracture fragility of pulse-like records. When T_p/T_1 is about the unit, the assessed WCSs in SMRFs are least susceptible to fracture. When T_p is away from T_1, fracture fragility of WCSs may be higher due to coincidence between pulse period and higher modes ($T_p < T_1$) or elongated/effective period ($T_p > T_1$). However, the fracture fragility approaches to far-field fracture results when $T_p >> T_1$, since the pulse period is far away from the building's most relevant dynamic periods.
- In general, fracture fragilities and risk of WCSs at near-fault sites are higher than their far-field counterparts due to the possible presence of pulse-like ground motions that increase the seismic demand of WCSs.
- When comparing the results for the six representative near-fault sites, several observations can be made: (1) the observed fracture fragility and risk of WCSs are higher when the sites are closer to the fault; (2) the observed fracture fragility and risk of WCSs are higher when the sites located at the end of the fault; (3) the effect of source-to-site distance on the fracture fragility and risk is more significant to the effect caused by the relative site location to the fault axis.

6.2 Future work

Although this dissertation advanced some uninvestigated aspects of the performance-based design and assessment of ECBPs and WCSs in SMRFs, it is acknowledged that several limitations of this dissertation may restrict the interpretation and application of the findings as summarized in Section 6.1. Therefore, the recommendations for future work are made in this subsection.

6.2.1 Next generation of ECBP design approach

Although Chapter 3 suggested alternative design approaches to overcome several limitations of the current method for ECBP design (i.e., the DG1 approach), the improvements still inherit the limitations of the DG1 approach. The characterization of internal force distributions in the DG1 method practically presumes a predetermined rectangular stress block (with a magnitude of the maximum bearing stress of the footing, $f_{\max}$; see Section 2.4.1), instead of an explicit solution of equilibrium, compatibility, and constitutive response. This may be inaccurate particularly for the high-eccentricity design cases with relatively low bending moment (Gomez et al. 2010; Kanvinde et al. 2013), because the true bearing stresses are well below $f_{\max}$ in such cases. This issue may greatly amplify the uncertainty in the demand calculation at component (i.e., the base plate or anchor rod) level, and result in very low ϕ-factors to ensure the designs meet the target reliability. Finally, the ECBPs designed according to Chapter 3 usually have thick base plates as well as multiple and large anchor rods, which are costly.

In response to the limitations of the DG1 method, a more rigorous design method may be developed and investigated to reduce the uncertainties in the determination of internal force distributions of the ECBP connections.

6.2.2 ECBPs subjected to axial force and biaxial bending

Chapter 3 in this dissertation exclusively focused on ECBPs loaded in uniaxial flexure combined with axial force. A practical assumption was made that the bending moments in the minor-axis direction of SMRFs may be relatively modest (compared to the major-axis counterparts). However, this practical assumption may be unconservative given the considerations of the following two aspects:

1. The presence of bending moment in the weak-axis direction of ECBPs may significantly lower their moment capacities in the major-axis direction. This has been observed from several finite element simulations (e.g., Choi and Ohi 2005; Fasaee et al. 2018; Kanvinde et al. 2013); and
2. The nature of earthquake always causes multiaxial loadings on SMRFs, resulting in biaxial bending at the ECBP connection level. When the SMRFs are subjected to orthogonal ground motion components, several previous simulation studies (e.g., Burton et al. 2018; Menun and Der Kiureghian 2000; Wang et al. 2019) have indicated the possibility that the minor-axis flexure may be significant at the base level.

As a result, ECBP connections subjected to biaxial bending in the presence of axial force should be further investigated, particularly in the case of seismic design and assessment. It is promising that this topic starts receiving research attention, a preliminary study to characterize internal force distributions in ECBPs loaded biaxially was proposed (Hassan et al. 2021) based on the DG1 method and finite element simulations that were validated against available experimental data (Gomez et al. 2010; Trautner and Hutchinson 2018). However, the mechanics of ECBPs subjected to biaxial bending, to date, is still not well understood. Intense scrutiny of this research topic is required, and more research efforts should be gathered to harmonize the research gap.

6.2.3 Post-fracture response of WCS and SMRFs

As indicated in Chapter 4 and Chapter 5, this dissertation simply assumes that the fracture of one WCS is the critical event that controls the retrofit decisions. Although the fracture risk of a single pre-Northridge WCS is unacceptably high, it is still questionable whether retrofit is urgent or not. This is mainly because the performance of SMRFs after the fracture of any splice and the subsequent fracture propagation is not well investigated. It is important to examine the effects of WCS fracture on the response of SMRFs; specifically, to find out whether the loss of one WCS triggers the fracture of other WCSs (in terms of location and timing) and a cascading effect that leads to loss of strength capacity and collapse of SMRFs.

Stillmaker et al. (2017) initially investigated this issue by simulating the post-fracture response of WCS through a new material model. This material model can reproduce some post-fracture phenomena of WCS (e.g., gapping and re-seating) once the fracture capacity of a WCS is reached. This study does have several limitations. Informed by Chapter 4 of this dissertation, the inclusion of vertical ground motion components and the relatively high variability of fracture capacity characterization may significantly alter the fracture results. These aspects were not considered in this study. Perhaps more importantly, the developed post-fracture material model can only simulate the axial behavior of the column and the loss of flexural strength after the fracture of WCSs, it cannot simulate the complete loss of shear strength at the splice level. Specifically, when the WCS is completely fractured, the simulation may be unconservative (i.e., the simulated performance of SMRF is better than the true performance), because the simulated WCS can still carry significant shear after fracture, which is not true in reality. These limitations may suggest conducting a more comprehensive simulation-based study in the future.

In addition, the NLTHA presented in this dissertation was conducted for intact frames. This may be not true for existing SMRFs with pre-Northridge WCS connections. Because many of SMRFs have experienced large earthquake (e.g., the 1994 Northridge earthquake) and may already have damaged WCSs that remains undetected or unrepaired. As a result, it is also critical to investigate the seismic performance of SMRFs with some fractured WCSs or WCSs have even lower fracture capacity (e.g., due to a larger flaw that was caused by a previous earthquake).

Bibliography

ACI (American Concrete Institute). (2019). "Building Code Requirements for Structural Concrete and Commentary." *ACI 318-19*, Farmington Hills, MI.

AISC (American Institute of Steel Construction). (1986). "Load and Resistance Factor Design Specification for Structural Steel Buildings." Chicago, IL.

AISC (American Institute of Steel Construction). (1989). "Manual of Steel Construction: Allowable Stress Design." Chicago, IL.

AISC (American Institute of Steel Construction). (2005). "Seismic Provisions for Structural Steel Buildings." *ANSI/AISC 341-05*, Chicago, IL.

AISC (American Institute of Steel Construction). (2010). "Seismic Provisions for Structural Steel Buildings." *ANSI/AISC 341-10*, Chicago, IL.

AISC (American Institute of Steel Construction). (2016a). "Specification for Structural Steel Buildings." *ANSI/AISC 360-16*, Chicago, IL.

AISC (American Institute of Steel Construction). (2016b). "Seismic Provisions for Structural Steel Buildings." *ANSI/AISC 341-16*, Chicago, IL.

AISC (American Institute of Steel Construction). (2016c). "Code of Standard Practice for Steel Buildings and Bridges." *ANSI/AISC 303-16*, Chicago, IL.

AISC (American Institute of Steel Construction). (2018). *Seismic Design Manual*, 3rd Edition, Chicago, IL.

Akbas, B., Doran, B., Sabol, T. A., Seker, O., Toru, P., and Shen, J. (2014). "Effect of various span lengths on seismic demand on column splices in steel moment frames." *Engineering Structures*, 70, 94–105.

Alali, A., Anderson, J., Beck., J., Benuska, K., Bonowitz, D., DiJulio, R., Dunlea, J., Eimani, T., Englehardt, M., Filippou, F., Hart, G., Ho, L., Huang, S., Husain, A., Jain, A., Kariotis, J., Kim, H., Kim, K., Krawinkler, H., Lee, C., Li, C., Lobo, R., May, B., Naeim, F., Paret, T., Polidori, D., Reinhorn, A., Sabol, T., Sadre, A., Sasaki, K., Stewart, J., Thiel, C., Uang, C., Uzarski, J., Vanik, M., VanWinkler, M., Youssef, N., and Yu, Q. (1995). “Analytical and Field Investigations of Buildings Affected by the Northridge Earthquake of January 17, 1994.” *Technical Report SAC 95-04*, SAC Joint Venture, Sacramento, CA.

Alavi, B., and Krawinkler, H. (2004). “Behavior of moment-resisting frame structures subjected to near-fault ground motions.” *Earthquake Engineering & Structural Dynamics*, 33(6), 687–706.

Ancheta, T. D., Darragh, R. B., Stewart, J. P., Seyhan, E., Silva, W. J., Chiou, B. S.-J., Wooddell, K. E., Graves, R. W., Kottke, A. R., Boore, D. M., Kishida, T., and Donahue, J. L. (2014). “NGA-West2 Database.” *Earthquake Spectra*, 30(3), 989–1005.

Anderson, J. C., Gourley, B. C., Green, M., Hajjar, J. F., Johnston, R., Leon, R. T., OSullivan, D. P., and Partridge, J. E. (1995). “Technical Report: Case Studies of Steel Moment Frame Building Performance in the Northridge Earthquake of January 17, 1994.” *Technical Report SAC 95-07*, SAC Joint Venture, Sacramento, CA.

Anderson, T. L. (2005). *Fracture Mechanics: Fundamentals and Applications*, 3rd Edition, CRC Press, Boca Raton, FL.

Ang, A. H.-S., and Cornell, C. A. (1974). “Reliability Bases of Structural Safety and Design.” *Journal of the Structural Division*, 100(9), 1755–1769.

Ang, A. H.-S., and Tang, W. H. (2006). *Probability Concepts in Engineering: Emphasis on Applications to Civil and Environmental Engineering*, 2nd Edition, Wiley, New York.

ASCE (American Society of Civil Engineers). (2000). “Prestandard and Commentary for the Seismic Rehabilitation of Buildings.” *FEMA-356*, Federal Emergency Management Agency, Washington, D.C.

ASCE (American Society of Civil Engineers). (2006). “Minimum Design Loads for Buildings and Other Structures.” *ASCE/SEI 7-05*, Reston, VA.

ASCE (American Society of Civil Engineers). (2016). “Minimum Design Loads for Buildings and Other Structures.” *ASCE/SEI 7-16*, Reston, VA.

Astaneh-Asl, A., Bergsma, G., and Shen, J. H. (1992). “Behavior and Design of Base Plates for Gravity, Wind and Seismic Loads.” *Proceeding, National Steel Construction Conference*, American Institute of Steel Construction, Chicago, IL.

ASTM (American Society for Testing and Materials). (2018a). “Standard Specification for High-Strength Low-Alloy Columbium-Vanadium Structural Steel.” *ASTM A572/A572M-18*, West Conshohocken, PA.

ASTM (American Society for Testing and Materials). (2018b). “Standard Specification for Anchor Bolts, Steel, 36, 55, and 105-ksi Yield Strength.” *ASTM F1554-18*, West Conshohocken, PA.

ASTM (American Society for Testing and Materials). (2019a). “Standard specification for carbon structural steel.” *ASTM A36/A36M-19,* West Conshohocken, PA.

ASTM (American Society for Testing and Materials). (2019b). “Standard Specification for General Requirements for Rolled Structural Steel Bars, Plates, Shapes, and Sheet Piling.” *ASTM A6/A6M-19*, West Conshohocken, PA.

ASTM (American Society for Testing and Materials). (2020). “Standard specification for structural steel shapes.” *ASTM A992/A992M-20*, West Conshohocken, PA.

ATC (Applied Technology Council). (1996a). “Improved Seismic Design Criteria for California Bridges: Provisional Recommendations.” *ATC-32*, Redwood City, CA.

ATC (Applied Technology Council). (1996b). “Seismic Evaluation and Retrofit of Concrete Buildings.” *ATC-40*, Redwood City, CA.

ATC (Applied Technology Council). (2009). “Quantification of Building Seismic Performance Factors.” *FEMA P695,* Federal Emergency Management Agency, Washington, D.C.

ATC (Applied Technology Council). (2012). “Seismic Performance Assessment of Buildings Volume 1 – Methodology.” *FEMA P-58-1*, Federal Emergency Management Agency, Washington, D.C.

Au, S.-K., and Beck, J. L. (2001). "Estimation of small failure probabilities in high dimensions by subset simulation." *Probabilistic Engineering Mechanics*, 16(4), 263–277.

Au, S.-K., and Wang, Y. (2014). *Engineering Risk Assessment with Subset Simulation*, John Wiley & Sons, Singapore.

Aviram, A., and Stojadinovic, B. (2006). "Evaluation of Design Methods for Column-Base Plate Connections in Gravity and Moment Resisting Frame." *Proceeding, 8th National Conference on Earthquake Engineering*, Earthquake Engineering Research Institute, San Francisco, CA.

Aviram, A., Stojadinovic, B., and Der Kiureghian, A. (2010). "Performance and Reliability of Exposed Column Base Plate Connections for Steel Moment-Resisting Frames." *PEER Report 2010/107*, Pacific Earthquake Engineering Research Center, University of California, Berkeley, CA.

AWC (American Wood Council). (2018). "National Design Specification for Wood Construction." Leesburg, VA.

Ayyub, B. M., and McCuen, R. H. (2003). *Probability, statistics, and reliability for engineers and scientists*, 2nd Edition, CRC Press, Boca Raton, FL.

Bakalis, K., and Vamvatsikos, D. (2018). "Seismic Fragility Functions via Nonlinear Response History Analysis." *Journal of Structural Engineering*, 144(10), 04018181.

Bakalis, K., Vamvatsikos, D., and Fragiadakis, M. (2017). "Seismic risk assessment of liquid storage tanks via a nonlinear surrogate model." *Earthquake Engineering & Structural Dynamics*, 46(15), 2851–2868.

Baker, J. W. (2007). "Quantitative Classification of Near-Fault Ground Motions Using Wavelet Analysis." *Bulletin of the Seismological Society of America*, 97(5), 1486–1501.

Baker, J. W. (2008). "Identification of near-fault velocity pulses and prediction of resulting response spectra." *Proceeding, Geotechnical Earthquake Engineering and Soil Dynamics IV*, Sacramento, CA.

Baker, J. W. (2015). "Efficient Analytical Fragility Function Fitting Using Dynamic Structural Analysis." *Earthquake Spectra,* 31(1), 579–599.

Baker, J. W., and Cornell, C. A. (2005). "A vector-valued ground motion intensity measure consisting of spectral acceleration and epsilon." *Earthquake Engineering & Structural Dynamics,* 34(10), 1193–1217.

Baker, J. W., and Cornell, C. A. (2006). "Spectral shape, epsilon and record selection." *Earthquake Engineering & Structural Dynamics,* 35(9), 1077–1095.

Baker, J. W., and Cornell, C. A. (2008a). "Vector-valued intensity measures for pulse-like near-fault ground motions." *Engineering Structures,* 30(4), 1048–1057.

Baker, J. W., and Cornell, C. A. (2008b). "Vector-valued Intensity Measures Incorporating Spectral Shape for Prediction of Structural Response." *Journal of Earthquake Engineering,* 12(4), 534–554.

Barsom, J. M. (1975). "Development of the AASHTO fracture-toughness requirements for bridge steels." *Engineering Fracture Mechanics,* 7(3), 605–618.

Bazzurro, P., Cornell, C. A., Shome, N., and Carballo, J. E. (1998). "Three Proposals for Characterizing MDOF Nonlinear Seismic Response." *Journal of Structural Engineering,* 124(11), 1281–1289.

Bjorhovde, R., Galambos, T. V., and Ravindra, M. K. (1978). "LRFD Criteria for Steel Beam-Columns." *Journal of the Structural Division,* 104(9), 1371–1387.

Bojórquez, E., and Iervolino, I. (2011). "Spectral shape proxies and nonlinear structural response." *Soil Dynamics and Earthquake Engineering,* 31(7), 996–1008.

Bommer, J. J., and Abrahamson, N. A. (2006). "Why Do Modern Probabilistic Seismic-Hazard Analyses Often Lead to Increased Hazard Estimates?" *Bulletin of the Seismological Society of America,* 96(6), 1967–1977.

Bommer, J. J., and Acevedo, A. B. (2004). "The Use of Real Earthquake Accelerograms as Input to Dynamic Analysis." *Journal of Earthquake Engineering,* 8(sup001), 43–91.

Boore, D. M., and Atkinson, G. M. (2008). “Ground-Motion Prediction Equations for the Average Horizontal Component of PGA, PGV, and 5%-Damped PSA at Spectral Periods between 0.01 s and 10.0 s.” *Earthquake Spectra,* 24(1), 99–138.

Bozorgnia, Y., Mahin, S. A., and Brady, A. G. (1998). “Vertical Response of Twelve Structures Recorded during the Northridge Earthquake.” *Earthquake Spectra*, 14(3), 411–432.

Bradley, B. A. (2013). “A critical examination of seismic response uncertainty analysis in earthquake engineering.” *Earthquake Engineering & Structural Dynamics*, 42(11), 1717–1729.

Bradley, B. A., Cubrinovski, M., Dhakal, R. P., and MacRae, G. A. (2009). “Intensity measures for the seismic response of pile foundations.” *Soil Dynamics and Earthquake Engineering*, 29(6), 1046–1058.

Bruneau, M., and Mahin, S. A. (1990). “Ultimate Behavior of Heavy Steel Section Welded Splices and Design Implications.” *Journal of Structural Engineering*, 116(8), 2214–2235.

Bruneau, M., and Mahin, S. A. (1991). “Full-Scale Tests of Butt-Welded Splices in Heavy-Rolled Steel Sections Subjected to Primary Tensile Stresses.” *Engineering Journal*, 28(1), 1–17.

BSSC (Building Seismic Safety Council). (1997). “NEHRP Guidelines for the Seismic Rehabilitation of Buildings.” *FEMA-273*, Federal Emergency Management Agency, Washington, D.C.

Bucher, C. G. (1988). “Adaptive sampling – an iterative fast Monte Carlo procedure.” *Structural Safety*, 5(2), 119–126.

Bucher, C. G., and Bourgund, U. (1990). “A fast and efficient response surface approach for structural reliability problems.” *Structural Safety*, 7(1), 57–66.

Bulleit, W. M. (2008). “Uncertainty in Structural Engineering.” *Practice Periodical on Structural Design and Construction*, 13(1), 24–30.

Burton, H. V., Doorandish, N., and Shokrabadi, M. (2018). “Probabilistic evaluation of combination rules for seismic force demands from orthogonal ground motion components.” *Engineering Structures,* 177, 234–243.

CEN (European Committee for Standardization). (2002). “Eurocode – Basis of structural design.” *EN 1990:2002,* Brussels.

Champion, C., and Liel, A. (2012). “The effect of near-fault directivity on building seismic collapse risk.” *Earthquake Engineering & Structural Dynamics*, 41(10), 1391–1409.

Chandramohan, R., Baker, J. W., and Deierlein, G. G. (2015). “Impact of computational choices on estimated structural collapse capacity under earthquake ground motions.” *Proceeding, Engineering Mechanics Institute Conference,* John A. Blume Earthquake Engineering Center, Stanford University, Stanford, CA.

Chi, W.-M., Deierlein, G. G., and Ingraffea, A. (2000). “Fracture Toughness Demands in Welded Beam-Column Moment Connections.” *Journal of Structural Engineering*, 126(1), 88–97.

Chioccarelli, E., and Iervolino, I. (2010). “Near-source seismic demand and pulse-like records: A discussion for L’Aquila earthquake.” *Earthquake Engineering & Structural Dynamics,* 13(9), 1039–1062.

Chioccarelli, E., and Iervolino, I. (2013). “Near-source seismic hazard and design scenarios.” *Earthquake Engineering & Structural Dynamics*, 42(4), 603–622.

Chioccarelli, E., and Iervolino, I. (2014). “Sensitivity analysis of directivity effects on PSHA.” *Bollettino di Geofisica Teorica e Applicata,* 55(1), 41–53.

Chiou, B., Darragh, R., Gregor, N., and Silva, W. (2008). “NGA Project Strong-Motion Database.” *Earthquake Spectra*, 24(1), 23–44.

Choi, J., and Ohi, K. (2005). “Evaluation on interaction surface of plastic resistance for exposed-type steel column bases under biaxial bending.” *Journal of Mechanical Science and Technology*, 19(3), 826–835.

Comerio, M. C., Ed. (2005). “PEER Testbed Study on a Laboratory Building: Exercising Seismic Performance Assessment.” *PEER Report 2005/12,* Pacific Earthquake Engineering Research Center, University of California, Berkeley, CA.

Cooper, P. B., Galambos, T. V., and Ravindra, M. K. (1978). “LRFD Criteria for Plate Girders.” *Journal of the Structural Division,* 104(9), 1389–1407.

Cornell, C. A. (1968). “Engineering seismic risk analysis.” *Bulletin of the Seismological Society of America,* 58(5), 1583–1606.

Cornell, C. A. (1969). “A Probability-Based Structural Code.” *ACI Journal Proceedings,* 66(12), 974–985.

Cornell, C. A., Jalayer, F., Hamburger, R. O., and Foutch, D. A. (2002). “Probabilistic Basis for 2000 SAC Federal Emergency Management Agency Steel Moment Frame Guidelines.” *Journal of Structural Engineering,* 128(4), 526–533.

Cornell, C. A., and Krawinkler, H. (2000). “Progress and challenges in seismic performance assessment.” *PEER Center News,* 3, 1–3.

Cosenza, E., and Manfredi, G. (2000). “Damage indices and damage measures.” *Progress in Structural Engineering and Materials,* 2(1), 50–59.

Cui, Y., Nagae, T., and Nakashima, M. (2009). “Hysteretic Behavior and Strength Capacity of Shallowly Embedded Steel Column Bases.” *Journal of Structural Engineering,* 135(10), 1231–1238.

Cui, Y., Wang, F., Li, H., and Yamada, S. (2019). “Rotational behavior of exposed column bases with different base plate thickness.” *Steel and Composite Structures,* 32(4), 497–507.

D’Ayala, D., Meslem, A., Vamvatsikos, D., Porter, K., Rossetto, T., Crowley, H., and Silva, V. (2014). *Guidelines for Analytical Vulnerability Assessment of low/mid-rise Buildings*. Vulnerability Global Component Project, Pavia.

Davenport, A. G. (1960). “Rationale for Determining Design Wind Velocities.” *Journal of the Structural Division,* 86(5), 39–68.

Deierlein, G. G., Krawinkler, H., and Cornell, C. A. (2003). “A framework for performance-based earthquake engineering.” *Proceeding, 2003 Pacific*

Conference on Earthquake Engineering, New Zealand Society for Earthquake Engineering, Christchurch.

Der Kiureghian, A., and Ditlevsen, O. (2009). “Aleatory or epistemic? Does it matter?” *Structural Safety,* 31(2), 105–112.

DeWolf, J. T. (1978). “Axially Loaded Column Base Plates.” *Journal of the Structural Division,* 104(5), 781–794.

DeWolf, J. T., and Bicker, D. T. (1990). *Steel Design Guide Series 1: Column Base Plates,* American Institute of Steel Construction, Chicago, IL.

DeWolf, J. T., and Sarisley, E. F. (1980). “Column Base Plates with Axial Loads and Moments.” *Journal of the Structural Division,* 106(11), 2167–2184.

Di Sarno, L. (2012). “Seismic response of steel columns in MRFs under multi-axial earthquake components.” *Proceeding, 7th International Conference on Behaviour of Steel Structures in Seismic Area (STESSA 2012),* London, 875–880.

Di Sarno, L., Elnashai, A. S., and Manfredi, G. (2011). “Assessment of RC columns subjected to horizontal and vertical ground motions recorded during the 2009 L’Aquila (Italy) earthquake.” *Engineering Structures,* 33(5), 1514–1535.

Dolsek, M. (2009). “Incremental dynamic analysis with consideration of modeling uncertainties.” *Earthquake Engineering & Structural Dynamics,* 38(6), 805–825.

Drake, R. M., and Elkin, S. J. (1999). “Beam-Column Base Plate Design – LRFD Method.” *Engineering Journal,* 36(1), 29–38.

Du, A., Padgett, J. E., and Shafieezadeh, A. (2019). “A posteriori optimal intensity measures for probabilistic seismic demand modeling.” *Bulletin of Earthquake Engineering,* 17(2), 681–706.

Dumas, M., Beaulieu, D., and Picard, A. (2006). “Characterization equations for steel column base connections.” *Canadian Journal of Civil Engineering,* 33(4), 409–420.

Eads, L., Miranda, E., and Lignos, D. (2016). “Spectral shape metrics and structural collapse potential.” *Earthquake Engineering & Structural Dynamics,* 45(10), 1643–1659.

Eads, L., Miranda, E., and Lignos, D. G. (2015). “Average spectral acceleration as an intensity measure for collapse risk assessment.” *Earthquake Engineering & Structural Dynamics*, 44(12), 2057–2073.

Ellingwood, B., and Galambos, T. V. (1982). “Probability-based criteria for structural design.” *Structural Safety*, 1(1), 15–26.

Ellingwood, B., MacGregor, J. G., Galambos, T. V., and Cornell, C. A. (1982). “Probability Based Load Criteria: Load Factors and Load Combinations.” *Journal of the Structural Division*, 108(5), 978–997.

Ellingwood, B. R. (1994). “Probability-based codified design: past accomplishments and future challenges.” *Structural Safety*, 13(3), 159–176.

Ellingwood, B. R. (2000). “LRFD: implementing structural reliability in professional practice.” *Engineering Structures*, 22(2), 106–115.

Ellingwood, B. R. (2008). “Structural reliability and performance-based engineering.” *Proceedings of the Institution of Civil Engineers – Structures and Buildings*, 161(4), 199–207.

Ellingwood, B. R., Galambos, T., MacGregor, J., and Cornell, C. (1980). “Development of a Probability Based Load Criterion for American National Standard A58 – Building Code Requirements for Minimum Design Loads in Buildings and Other Structures.” *National Bureau of Standards Special Publication 577*, US Government Printing Office, Washington, D.C.

Ellingwood, B. R., and Kinali, K. (2009). “Quantifying and communicating uncertainty in seismic risk assessment.” *Structural Safety*, 31(2), 179–187.

Ermopoulos, J. C., and Michaltsos, G. T. (1998). “Analytical modelling of stress distribution under column base plates.” *Journal of Constructional Steel Research*, 46(1–3), 246.

Ermopoulos, J. C., and Stamatopoulos, G. N. (1996a). “Mathematical modelling of column base plate connections.” *Journal of Constructional Steel Research*, 36(2), 79–100.

Ermopoulos, J. C., and Stamatopoulos, G. N. (1996b). "Analytical modelling of column-base plates under cyclic loading." *Journal of Constructional Steel Research*, 40(3), 225–238.

Fahmy, M. (2000). "Seismic Behavior of Moment-resisting Steel Column Bases." PhD thesis, University of Michigan, Ann Arbor.

Falborski, T., Torres-Rodas, P., Zareian, F., and Kanvinde, A. (2020). "Effect of Base-Connection Strength and Ductility on the Seismic Performance of Steel Moment-Resisting Frames." *Journal of Structural Engineering*, 146(5), 04020054.

Faravelli, L. (1989). "Response-Surface Approach for Reliability Analysis." *Journal of Engineering Mechanics*, 115(12), 2763–2781.

Fasaee, M. A. K., Banan, M. R., and Ghazizadeh, S. (2018). "Capacity of exposed column base connections subjected to uniaxial and biaxial bending moments." *Journal of Constructional Steel Research*, 148, 361–370.

Fayaz, J., and Zareian, F. (2019). "Reliability Analysis of Steel SMRF and SCBF Structures Considering the Vertical Component of Near-Fault Ground Motions." *Journal of Structural Engineering*, 145(7), 04019061.

Field, E. H., Jordan, T. H., and Cornell, C. A. (2003). "OpenSHA: A Developing Community-modeling Environment for Seismic Hazard Analysis." *Seismological Research Letters*, 74(4), 406–419.

Fiessler, B., Neumann, H.-J., and Rackwitz, R. (1979). "Quadratic Limit States in Structural Reliability." *Journal of the Engineering Mechanics Division*, 105(4), 661–676.

Fisher, J. M., and Kloiber, L. A. (2006). *Steel Design Guide 1: Base Plate and Anchor Rod Design*, 2nd Edition, American Institute of Steel Construction, Chicago, IL.

Fisher, J. W., Galambos, T. V., Kulak, G. L., and Ravindra, M. K. (1978). "Load and Resistance Factor Design Criteria for Connectors." *Journal of the Structural Division*, 104(9), 1427–1441.

Forrester, A. I. J., Sóbester, A., and Keane, A. J. (2008). *Engineering Design via Surrogate Modelling – A Practical Guide*, John Wiley & Sons, Chichester.

Fragiadakis, M., Vamvatsikos, D., and Aschheim, M. (2014). “Application of Nonlinear Static Procedures for the Seismic Assessment of Regular RC Moment Frame Buildings.” *Earthquake Spectra*, 30(2), 767–794.

Freddi, F., Padgett, J. E., and Dall’Asta, A. (2017). “Probabilistic seismic demand modeling of local level response parameters of an RC frame.” *Bulletin of Earthquake Engineering*, 15(1), 1–23.

Freudenthal, A. M., Garretts, J. M., and Shinozuka, M. (1966). “The Analysis of Structural Safety.” *Journal of the Structural Division*, 92(1), 267–326.

Gagnon, D. P., and Kennedy, D. J. L. (1989). “Behaviour and ultimate tensile strength of partial joint penetration groove welds.” *Canadian Journal of Civil Engineering*, 16(3), 384–399.

Galambos, J. (1978). *The Asymptotic Theory of Extreme Order Statistics*, Wiley, New York.

Galambos, T. V. (1960). “Influence of Partial Base Fixity on Frame Stability.” *Journal of the Structural Division*, 86(5), 85–108.

Galambos, T. V. (1981). “Load and Resistance Factor Design (T.R. Higgins Award).” *Engineering Journal*, 18(3), 74–82.

Galambos, T. V., Ellingwood, B., MacGregor, J. G., and Cornell, C. A. (1982). “Probability Based Load Criteria: Assessment of Current Design Practice.” *Journal of the Structural Division*, 108(5), 959–977.

Galambos, T. V., and Ravindra, M. K. (1978). “Properties of Steel for Use in LRFD.” *Journal of the Structural Division*, 104(9), 1459–1468.

Galasso, C., Stillmaker, K., Eltit, C., and Kanvinde, A. (2015). “Probabilistic demand and fragility assessment of welded column splices in steel moment frames.” *Earthquake Engineering & Structural Dynamics*, 44(11), 1823–1840.

Ghosn, M., Frangopol, D. M., McAllister, T. P., Shah, M., Diniz, S. M. C., Ellingwood, B. R., Manuel, L., Biondini, F., Catbas, N., Strauss, A., and Zhao, X. L. (2016). “Reliability-Based Performance Indicators for Structural Members.” *Journal of Structural Engineering*, 142(9), F4016002.

Ghosn, M., and Moses, F. (1986). “Reliability Calibration of Bridge Design Code.” *Journal of Structural Engineering*, 112(4), 745–763.

Giovenale, P., Cornell, C. A., and Esteva, L. (2004). “Comparing the adequacy of alternative ground motion intensity measures for the estimation of structural responses.” *Earthquake Engineering & Structural Dynamics*, 33(8), 951–979.

Gomez, I., Kanvinde, A., and Deierlein, G. (2010). *Exposed Column Base Connections Subjected to Axial Compression and Flexure*, American Institute of Steel Construction, Chicago, IL.

Gomez, I. R. (2010). “Behavior and Design of Column Base Connections.” PhD thesis, University of California, Davis.

Gomez, I. R., Kanvinde, A. M., and Deierlein, G. G. (2011). “Experimental Investigation of Shear Transfer in Exposed Column Base Connections.” *Engineering Journal*, 48(4), 245–264.

Goulet, C. A., Haselton, C. B., Mitrani-Reiser, J., Beck, J. L., Deierlein, G. G., Porter, K. A., and Stewart, J. P. (2007). “Evaluation of the seismic performance of a code-conforming reinforced-concrete frame building – from seismic hazard to collapse safety and economic losses.” *Earthquake Engineering & Structural Dynamics*, 36(13), 1973–1997.

Goulet, C. A., Kishida, T., Ancheta, T. D., Cramer, C. H., Darragh, R. B., Silva, W. J., Hashash, Y. M., Harmon, J., Parker, G. A., Stewart, J. P., and Youngs, R. R. (2021). “PEER NGA-East database.” *Earthquake Spectra*, 37(1_suppl), 1331–1353.

Grauvilardell, J. E., Lee, D., Ajar, J. F., and Dexter, R. J. (2005). “Synthesis of Design, Testing and Analysis Research on Steel Column Base Plate Connections in High Seismic Zones.” *Structural Engineering Report No. ST-04-02,* University of Minnesota, Minneapolis, MN.

Grilli, D., Jones, R., and Kanvinde, A. (2017). “Seismic Performance of Embedded Column Base Connections Subjected to Axial and Lateral Loads.” *Journal of Structural Engineering*, 143(5), 04017010.

Günay, S., and Mosalam, K. M. (2013). “PEER Performance-Based Earthquake Engineering Methodology, Revisited.” *Journal of Earthquake Engineering*, 17(6), 829–858.

Gupta, A., and Krawinkler, H. (1999). “Seismic Demands for Performance Evaluation of Steel Moment Resisting Frame Structures.” *Technical Report No. 132 (SAC Task 5.4.3),* John A. Blume Earthquake Engineering Center, Stanford University, Stanford, CA.

Hanks, K. N., and Richards, P. W. (2019). “Experimental Performance of Block-Out Connections at the Base of Steel Moment Frames.” *Journal of Structural Engineering*, 145(7), 04019057.

Hansell, W. C., Galambos, T. V., Ravindra, M. K., and Viest, I. M. (1978). “Composite Beam Criteria in LRFD.” *Journal of the Structural Division*, 104(9), 1409–1426.

Haselton, C. B., Baker, J. W., Liel, A. B., and Deierlein, G. G. (2011). “Accounting for Ground-Motion Spectral Shape Characteristics in Structural Collapse Assessment through an Adjustment for Epsilon.” *Journal of Structural Engineering*, 137(3), 332–344.

Hasofer, A. M., and Lind, N. C. (1974). “Exact and Invariant Second-Moment Code Format.” *Journal of the Engineering Mechanics Division*, 100(1), 111–121.

Hassan, A. S., Torres-Rodas, P., Giulietti, L., and Kanvinde, A. (2021). “Strength characterization of exposed column base plates subjected to axial force and biaxial bending.” *Engineering Structures*, 237, 112165.

Hawkins, N. M. (1968). “The bearing strength of concrete loaded through rigid plates.” *Magazine of Concrete Research*, 20(62), 31–40.

Hayes, J. M. (1957). “Effect of Initial Eccentricities on Column Performance and Capacity.” *Journal of the Structural Division*, 83(6), 1–40.

Hensman, J., and Nethercot, D. A. (2000). “Utilisation of Test Data for Column Bases When Assessing Overall Frame Response: A Review.” *Advances in Structural Engineering*, 3(1), 7–17.

Hohenbichler, M., and Rackwitz, R. (1981). “Non-Normal Dependent Vectors in Structural Safety.” *Journal of the Engineering Mechanics Division*, 107(6), 1227–1238.

Hon, K. K., and Melchers, R. E. (1988). “Experimental behaviour of steel column bases.” *Journal of Constructional Steel Research*, 9(1), 35–50.

Iervolino, I., and Cornell, C. A. (2008). “Probability of Occurrence of Velocity Pulses in Near-Source Ground Motions.” *Bulletin of the Seismological Society of America*, 98(5), 2262–2277.

Iervolino, I., and Galasso, C. (2012). “Comparative assessment of load–resistance factor design of FRP-reinforced cross sections.” *Construction and Building Materials*, 34, 151–161.

ISO (International Organization for Standardization). (2010). “Bases for design of structures – Assessment of existing structures.” *ISO 13822:2010*, Geneva.

Iwan, W. D. (1997). “Drift Spectrum: Measure of Demand for Earthquake Ground Motions.” *Journal of Structural Engineering*, 123(4), 397–404.

Jaiswal, K., Wald, D., and D’Ayala, D. (2011). “Developing Empirical Collapse Fragility Functions for Global Building Types.” *Earthquake Spectra*, 27(3), 775–795.

Jalayer, F. (2003). “Direct Probabilistic Seismic Anaysis: Implementing Non-linear Dynamic Assessments.” PhD thesis, Stanford University.

Jalayer, F., Beck, J. L., and Zareian, F. (2012). “Analyzing the Sufficiency of Alternative Scalar and Vector Intensity Measures of Ground Shaking Based on Information Theory.” *Journal of Engineering Mechanics*, 138(3), 307–316.

Jalayer, F., and Cornell, C. A. (2009). “Alternative non-linear demand estimation methods for probability-based seismic assessments.” *Earthquake Engineering & Structural Dynamics*, 38(8), 951–972.

Jalayer, F., Ebrahimian, H., Miano, A., Manfredi, G., and Sezen, H. (2017). “Analytical fragility assessment using unscaled ground motion records.” *Earthquake Engineering & Structural Dynamics*, 46(15), 2639–2663.

Jalayer, F., Franchin, P., and Pinto, P. E. (2007). “A scalar damage measure for seismic reliability analysis of RC frames.” *Earthquake Engineering & Structural Dynamics*, 36(13), 2059–2079.

Kanvinde, A. M., Grilli, D. A., and Zareian, F. (2012). “Rotational Stiffness of Exposed Column Base Connections: Experiments and Analytical Models.” *Journal of Structural Engineering*, 138(5), 549–560.

Kanvinde, A. M., Higgins, P., Cooke, R. J., Perez, J., and Higgins, J. (2015). “Column Base Connections for Hollow Steel Sections: Seismic Performance and Strength Models.” *Journal of Structural Engineering*, 141(7), 04014171.

Kanvinde, A. M., Jordan, S. J., and Cooke, R. J. (2013). “Exposed column base plate connections in moment frames – Simulations and behavioral insights.” *Journal of Constructional Steel Research*, 84, 82–93.

Kaufman, E. J., and Fisher, J. W. (1995). “A Study of the Effects of Material and Welding Factors on Moment Frame Weld Joint Performance Using Small-Scale Tension Specimen.” *Technical Report SAC 95-08*, SAC Joint Venture, Sacramento, CA.

Kazantzi, A. K., and Vamvatsikos, D. (2015). “Intensity measure selection for vulnerability studies of building classes.” *Earthquake Engineering & Structural Dynamics*, 44(15), 2677–2694.

Kiani, J., Camp, C., and Pezeshk, S. (2019). “The importance of non-spectral intensity measures on the risk-based structural responses.” *Soil Dynamics and Earthquake Engineering*, 120, 97–112.

Kohrangi, M., Bazzurro, P., and Vamvatsikos, D. (2016a). “Vector and Scalar IMs in Structural Response Estimation, Part II: Building Demand Assessment.” *Earthquake Spectra*, 32(3), 1525–1543.

Kohrangi, M., Bazzurro, P., and Vamvatsikos, D. (2016b). “Vector and Scalar IMs in Structural Response Estimation, Part I: Hazard Analysis.” *Earthquake Spectra*, 32(3), 1507–1524.

Kohrangi, M., Kotha, S. R., and Bazzurro, P. (2018). “Ground-motion models for average spectral acceleration in a period range: direct and indirect methods.” *Bulletin of Earthquake Engineering*, 16(1), 45–65.

Krawinkler, H. (1999). “Challenges and Progress in Performance-Based Earthquake Engineering.” *Proceeding, International Seminar on Seismic Engineering for Tomorrow – In Honor of Professor Hiroshi Akiyama*, Tokyo.

Krawinkler, H. (2002). “A general approach to seismic performance assessment.” *Proceeding, International Conference on Advances and New Challenges in Earthquake Engineering Research (ICANCEER)*, Hong Kong.

Krawinkler, H., Ed. (2005). “Van Nuys Hotel Building Testbed Report: Exercising Seismic Performance Assessment.” *PEER Report 2005/11*, Pacific Earthquake Engineering Research Center, University of California, Berkeley, CA.

Krawinkler, H., and Miranda, E. (2004). “Performance-Based Earthquake Engineering.” Chapter 9, *Earthquake Engineering: From Engineering Seismology to Performance-Based Engineering*, Y. Bozorgnia and V. V. Bertero, Eds., CRC Press, Boca Raton, FL.

Kunnath, S. K., Larson, L., and Miranda, E. (2006). “Modelling considerations in probabilistic performance-based seismic evaluation: case study of the I-880 viaduct.” *Earthquake Engineering & Structural Dynamics*, 35(1), 57–75.

Kurata, M., Nakashima, M., and Suita, K. (2005). “Effect of Column Base Behaviour on the Seismic Response of Steel Moment Frames.” *Journal of Earthquake Engineering*, 9(sup2), 415–438.

LaFraugh, R. W., and Magura, D. D. (1966). “Connections in Precast Concrete Structures- Column Base Plates.” *PCI Journal*, 11(6), 18–39.

Lallemant, D., Kiremidjian, A., and Burton, H. (2015). “Statistical procedures for developing earthquake damage fragility curves.” *Earthquake Engineering & Structural Dynamics*, 44(9), 1373–1389.

Latour, M., and Rizzano, G. (2019). “Mechanical modelling of exposed column base plate joints under cyclic loads.” *Journal of Constructional Steel Research*, 162, 105726.

Lee, D.-Y., Geol, S. C., and Stojadinovic, B. (2008a). “Exposed Column-Base Plate Connections Bending About Weak Axis: I. Numerical Parametric Study.” *International Journal of Steel Structures,* 8(1), 11–27.

Lee, D.-Y., Goel, S. C., and Stojadinovic, B. (2008b). “Exposed Column-Base Plate Connections Bending About Weak Axis: II. Experimental Study.” *International Journal of Steel Structures,* 8(1), 29–41.

Liel, A. B., Haselton, C. B., Deierlein, G. G., and Baker, J. W. (2009). “Incorporating modeling uncertainties in the assessment of seismic collapse risk of buildings.” *Structural Safety,* 31(2), 197–211.

Lignos, D. G., Hikino, T., Matsuoka, Y., and Nakashima, M. (2013). “Collapse Assessment of Steel Moment Frames Based on E-Defense Full-Scale Shake Table Collapse Tests.” *Journal of Structural Engineering,* 139(1), 120–132.

Lignos, D. G., Krawinkler, H., and Whittaker, A. S. (2011). “Prediction and validation of sidesway collapse of two scale models of a 4-story steel moment frame.” *Earthquake Engineering & Structural Dynamics*, 40(7), 807–825.

Liu, J., Sabelli, R., Brockenbrough, R. L., and Fraser, T. P. (2007). “Expected Yield Stress and Tensile Strength Ratios for Determination of Expected Member Capacity in the 2005 AISC Seismic Provisions.” *Engineering Journal,* 44(1), 15–26.

Luco, N., and Bazzurro, P. (2007). “Does amplitude scaling of ground motion records result in biased nonlinear structural drift responses?” *Earthquake Engineering & Structural Dynamics*, 36(13), 1813–1835.

Luco, N., and Cornell, C. A. (2007). “Structure-Specific Scalar Intensity Measures for Near-Source and Ordinary Earthquake Ground Motions.” *Earthquake Spectra,* 23(2), 357–392.

Macrae, G. A., Fields, D., and Mattheis, J. (2000). “Ground motion characteristic effects on multistorey steel frame response.” *Proceeding, 12th World Conference on Earthquake Engineering*, New Zealand Society for Earthquake Engineering, Auckland.

Madsen, H. O., Krenk, S., and Lind, N. C. (1986). *Methods of structural safety*, Prentice-Hall, Englewood Cliffs, NJ.

Maison, B. F., Kasai, K., Dexter, R., Ingraffea, A. R., and Deierlein., G. G. (1996). "Selected Results from the SAC Phase I Beam-Column Connection Pre-Test Analyses." *Report No. SAC/BD-96/01*, SAC Joint Venture, Sacramento, CA.

Martins, L., and Silva, V. (2021). "Development of a fragility and vulnerability model for global seismic risk analyses." *Bulletin of Earthquake Engineering*, 19(15), 6719–6745.

Mavroeidis, G. P. (2003). "A Mathematical Representation of Near-Fault Ground Motions." *Bulletin of the Seismological Society of America*, 93(3), 1099–1131.

Mazzoni, S., McKenna, F., Scott, M. H., and Fenves, G. L. (2009). *Open System for Earthquake Engineering Simulation User Command-Language Manual. OpenSees version 2.0*, Pacific Earthquake Engineering Research Center, University of California, Berkeley, CA.

McGuire, R. K. (2008). "Probabilistic seismic hazard analysis: Early history." *Earthquake Engineering & Structural Dynamics*, 37(3), 329–338.

Melcher, J., Kala, Z., Holický, M., Fajkus, M., and Rozlívka, L. (2004). "Design characteristics of structural steels based on statistical analysis of metallurgical products." *Journal of Constructional Steel Research*, 60(3–5), 795–808.

Melchers, R. E. (1992). "Column-base response under applied moment." *Journal of Constructional Steel Research*, 23(1–3), 127–143.

Melchers, R. E., and Beck, A. T. (2018). *Structural Reliability Analysis and Prediction*, 3rd Edition, John Wiley & Sons, Hoboken, NJ.

Menun, C., and Der Kiureghian, A. (2000). "Envelopes for Seismic Response Vectors. I: Theory." *Journal of Structural Engineering*, 126(4), 467–473.

Minas, S., and Galasso, C. (2019). "Accounting for spectral shape in simplified fragility analysis of case-study reinforced concrete frames." *Soil Dynamics and Earthquake Engineering*, 119, 91–103.

Miranda, E., and Aslani, H. (2003). "Probabilistic Response Assessment for Building-Specific Loss Estimation." *PEER Report 2003/03*, Pacific Earthquake Engineering Research Center, University of California, Berkeley, CA.

Moehle, J., and Deierlein, G. G. (2004). "A Framework Methodology for Performance-Based Earthquake Engineering." *Proceeding, 13th World Conference on Earthquake Engineering*, Canadian Association for Earthquake Engineering, Vancouver.

Moehle, J. P. (2003). "A framework for performance-based earthquake engineering." *Proceeding, ATC-15-9 Workshop on the Improvement of Building Structural Design and Construction Practices*, Maui, HI.

Myers, A. T., Kanvinde, A. M., Deierlein, G. G., and Fell, B. V. (2009). "Effect of weld details on the ductility of steel column baseplate connections." *Journal of Constructional Steel Research*, 65(6), 1366–1373.

NEHRP (National Earthquake Hazards Reduction Program). (2010). "Evaluation of the FEMA P-695 Methodology for Quantification of Building Seismic Performance Factors." *NIST GCR 10-917-8*, National Institute of Standards and Technology, US Department of Commerce, Gaithersburg, MD.

Noh, H. Y., Lallemant, D., and Kiremidjian, A. S. (2015). "Development of empirical and analytical fragility functions using kernel smoothing methods." *Earthquake Engineering & Structural Dynamics*, 44(8), 1163–1180.

Nowak, A. S., and Collins, K. R. (2012). *Reliability of Structures*, 2nd Edition, CRC Press, Boca Raton, FL.

Nowak, A. S., and Szerszen, M. M. (2003). "Calibration of Design Code for Buildings (ACI 318): Part 1 – Statistical Models for Resistance." *ACI Structural Journal*, 100(3), 377–382.

Nudel, A., Marusich, S., Dana, M., and Roufegarinejad, A. (2015). "Evaluation and Remediation of Pre-Northridge Steel Moment Frame Column Splices." *Proceeding, Second ATC & SEI Conference on Improving the Seismic Performance of Existing Buildings and Other Structures 2015*, American Society of Civil Engineers, Reston, VA, 287–302.

Nuttayasakul, N. (2000). “Finite Element Fracture Mechanics Study of Partial Penetration Welded Splices.” PhD thesis, Stanford University.

OSHA (Occupational Safety and Health Administration). (2001). “Safety Standards for Steel Erection.” *Subpart R of 29 CFR Part 1926,* Washington, D.C.

Padgett, J. E., Nielson, B. G., and DesRoches, R. (2008). “Selection of optimal intensity measures in probabilistic seismic demand models of highway bridge portfolios.” *Earthquake Engineering & Structural Dynamics,* 37(5), 711–725.

Pagani, M., Monelli, D., Weatherill, G., Danciu, L., Crowley, H., Silva, V., Henshaw, P., Butler, L., Nastasi, M., Panzeri, L., Simionato, M., and Vigano, D. (2014). “OpenQuake Engine: An Open Hazard (and Risk) Software for the Global Earthquake Model.” *Seismological Research Letters,* 85(3), 692–702.

Papaleontiou, C., and Roesset, J. M. (1993). “Effect of vertical accelerations on seismic response of frames.” *Proceeding, Second European Conference on Structural Dynamics (EURODYN ’93),* Trondheim, 19–26.

Papazoglou, A. J., and Elnashai, A. S. (1996). “Analytical and field evidence of the damaging effect of vertical earthquake ground motion.” *Earthquake Engineering & Structural Dynamics,* 25(10), 1109–1137.

Penserini, P., and Colson, A. (1989). “Ultimate limit strength of column-base connections.” *Journal of Constructional Steel Research*, 14(4), 301–320.

Petrone, F., Higgins, P. S., Bissonnette, N. P., and Kanvinde, A. M. (2016). “The cross-aisle seismic performance of storage rack base connections.” *Journal of Constructional Steel Research,* 122, 520–531.

Philpot, T. A., and Rosowsky, D. V. (1992). “Statistics for Light-Occupancy Live Load Modeling.” *Structural Engineering Report CE-STR-92-3,* Purdue University, West Lafayette, IN.

Picard, A., and Beaulieu, D. (1985). “Behaviour of a simple column base connection.” *Canadian Journal of Civil Engineering*, 12(1), 126–136.

Picard, A., Beaulieu, D., and Pérusse, B. (1987). “Rotational restraint of a simple column base connection.” *Canadian Journal of Civil Engineering*, 14(1), 49–57.

Popov, E. P., and Stephen, R. M. (1977). “Capacity of Columns with Splice Imperfections.” *Engineering Journal*, 14(1), 16–23.

Porter, K. A. (2003). “An Overview of PEER’s Performance-Based Earthquake Engineering Methodology.” *Proceeding, 9th International Conference on Applications of Statistics and Probability in Civil Engineering (ICASP9),* San Francisco, CA.

Porter, K., Mitrani-Reiser, J., and Beck, J. L. (2006). “Near-real-time loss estimation for instrumented buildings.” *The Structural Design of Tall and Special Buildings*, 15(1), 3–20.

Power, M., Chiou, B., Abrahamson, N., Bozorgnia, Y., Shantz, T., and Roblee, C. (2008). “An Overview of the NGA Project.” *Earthquake Spectra*, 24(1), 3–21.

Prakash, V., Powell, G., and Campbell, S. (1993). “DRAIN-2DX: Basic Program Description and User Guide.” *Report No. UCB/SEMM-93/17*, University of California, Berkeley, CA.

Ravindra, M. K., Cornell, C. A., and Galambos, T. V. (1978). “Wind and Snow Load Factors for Use in LRFD.” *Journal of the Structural Division*, 104(9), 1443–1457.

Ravindra, M. K., and Galambos, T. V. (1978). “Load and Resistance Factor Design for Steel.” *Journal of the Structural Division*, 104(9), 1337–1353.

Romão, X., Delgado, R., and Costa, A. (2011). “Assessment of the Statistical Distributions of Structural Demand Under Earthquake Loading.” *Journal of Earthquake Engineering*, 15(5), 724–753.

Rossetto, T., and Elnashai, A. (2005). “A new analytical procedure for the derivation of displacement-based vulnerability curves for populations of RC structures.” *Engineering Structures*, 27(3), 397–409.

Rossetto, T., Ioannou, I., Grant, D., and Maqsood, T. (2014). “Guidelines for empirical vulnerability assessment.” *GEM Technical Report 2014-08*, GEM Foundation, Pavia.

SAC Joint Venture. (2000). “A Policy Guide to Steel Moment Frame Construction.” *FEMA 354*, Federal Emergency Management Agency, Washington, D.C.

Salazar, A. R., and Haldar, A. (2000). "Structural responses considering the vertical component of earthquakes." *Computers & Structures*, 74(2), 131–145.

Saxena, A. (1998). *Nonlinear Fracture Mechanics for Engineers*, CRC Press, Boca Raton, FL.

Schmidt, B. J., and Bartlett, F. M. (2002). "Review of resistance factor for steel: data collection." *Canadian Journal of Civil Engineering*, 29(1), 98–108.

SEAOC (Structural Engineers Association of California). (1995). *Vision 2000: Performance-Based Seismic Engineering of Buildings*, Sacramento, CA.

SEAOC (Structural Engineers Association of California). (2015). *2015 IBC SEAOC Structural/Seismic Design Manual Volume 1: Code Application Examples*, Sacramento, CA.

Shafieezadeh, A., Ramanathan, K., Padgett, J. E., and DesRoches, R. (2012). "Fractional order intensity measures for probabilistic seismic demand modeling applied to highway bridges." *Earthquake Engineering & Structural Dynamics*, 41(3), 391–409.

Shahi, S. K., and Baker, J. W. (2011). "An Empirically Calibrated Framework for Including the Effects of Near-Fault Directivity in Probabilistic Seismic Hazard Analysis." *Bulletin of the Seismological Society of America*, 101(2), 742–755.

Shahi, S. K., and Baker, J. W. (2014). "An Efficient Algorithm to Identify Strong-Velocity Pulses in Multicomponent Ground Motions." *Bulletin of the Seismological Society of America*, 104(5), 2456–2466.

Shaw, S. M. (2013). "Seismic Performance of Partial Joint Penetration Welds in Special Moment Resisting Frames." PhD thesis, University of California, Davis.

Shaw, S. M., Stillmaker, K., and Kanvinde, A. M. (2015). "Seismic response of partial-joint-penetration welded column splices in moment-resisting frames." *Engineering Journal*, 52(2), 87–108.

Shen, J., Sabol, T. A., Akbas, B., and Sutchiewcharn, N. (2010). "Seismic Demand on Column Splices in Steel Moment Frames." *Engineering Journal*, 47(4), 223–240.

Shinozuka, M. (1983). “Basic Analysis of Structural Safety.” *Journal of Structural Engineering*, 109(3), 721–740.

Shinozuka, M., Feng, M. Q., Lee, J., and Naganuma, T. (2000). “Statistical Analysis of Fragility Curves.” *Journal of Engineering Mechanics,* 126(12), 1224–1231.

Shome, N. (1999). “Probabilistic seismic demand analysis of nonlinear structures.” PhD thesis, Stanford University.

Shome, N., Cornell, C. A., Bazzurro, P., and Carballo, J. E. (1998). “Earthquakes, Records, and Nonlinear Responses.” *Earthquake Spectra,* 14(3), 469–500.

Silva, V., Crowley, H., Pagani, M., Monelli, D., and Pinho, R. (2014a). “Development of the OpenQuake engine, the Global Earthquake Model’s open-source software for seismic risk assessment.” *Natural Hazards,* 72(3), 1409–1427.

Silva, V., Crowley, H., Varum, H., Pinho, R., and Sousa, R. (2014b). “Evaluation of analytical methodologies used to derive vulnerability functions.” *Earthquake Engineering & Structural Dynamics*, 43(2), 181–204.

Singh, J. P. (1985). “Earthquake Ground Motions: Implications for Designing Structures and Reconciling Structural Damage.” *Earthquake Spectra,* 1(2), 239–270.

Skoulidou, D., and Romão, X. (2019). “Uncertainty quantification of fragility and risk estimates due to seismic input variability and capacity model uncertainty.” *Engineering Structures*, 195, 425–437.

Smerzini, C., Galasso, C., Iervolino, I., and Paolucci, R. (2014). “Ground Motion Record Selection Based on Broadband Spectral Compatibility.” *Earthquake Spectra*, 30(4), 1427–1448.

Somerville, P. G. (2003). “Magnitude scaling of the near fault rupture directivity pulse.” *Physics of the Earth and Planetary Interiors*, 137(1–4), 201–212.

Somerville, P. G., Smith, N. F., Graves, R. W., and Abrahamson, N. A. (1997). “Modification of Empirical Strong Ground Motion Attenuation Relations to Include the Amplitude and Duration Effects of Rupture Directivity.” *Seismological Research Letters,* 68(1), 199–222.

Stamatopoulos, G. N., and Ermopoulos, J. C. (1997). “Interaction curves for column base-plate connections.” *Journal of Constructional Steel Research,* 44(1–2), 69–89.

Stillmaker, K., Kanvinde, A., and Galasso, C. (2016). “Fracture Mechanics-Based Design of Column Splices with Partial Joint Penetration Welds.” *Journal of Structural Engineering*, 142(2), 04015115.

Stillmaker, K., Lao, X., Galasso, C., and Kanvinde, A. (2017). “Column splice fracture effects on the seismic performance of steel moment frames.” *Journal of Constructional Steel Research,* 137(2017), 93–101.

Takamatsu, T., and Tamai, H. (2005). “Non-slip-type restoring force characteristics of an exposed-type column base.” *Journal of Constructional Steel Research*, 61(7), 942–961.

Targowski, R., Lamblin, D., and Guerlement, G. (1993). “Baseplate column connection under bending: Experimental and numerical study.” *Journal of Constructional Steel Research,* 27(1–3), 37–54.

Thambiratnam, D. P., and Krishnamurthy, N. (1989). “Computer analysis of column base plates.” *Computers & Structures,* 33(3), 839–850.

Thambiratnam, D. P., and Paramasivam, P. (1986). “Base Plates Under Axial Loads and Moments.” *Journal of Structural Engineering*, 112(5), 1166–1181.

Thoft-Christensen, P., and Baker, M. J. (1982). *Structural Reliability Theory and Its Applications*, Springer, Heidelberg.

Tichý, M. (1994). “First-order third-moment reliability method.” *Structural Safety,* 16(3), 189–200.

Torres-Rodas, P., Fayaz, J., and Zareian, F. (2020). “Strength resistance factors for seismic design of exposed based plate connections in special steel moment resisting frames.” *Earthquake Spectra,* 36(2), 537–553.

Torres-Rodas, P., Zareian, F., and Kanvinde, A. (2018). “Seismic Demands in Column Base Connections of Steel Moment Frames.” *Earthquake Spectra*, 34(3), 1383–1403.

Tothong, P., and Cornell, C. A. (2006). “An Empirical Ground-Motion Attenuation Relation for Inelastic Spectral Displacement.” *Bulletin of the Seismological Society of America*, 96(6), 2146–2164.

Tothong, P., Cornell, C. A., and Baker, J. W. (2007). “Explicit Directivity-Pulse Inclusion in Probabilistic Seismic Hazard Analysis.” *Earthquake Spectra*, 23(4), 867–891.

Tothong, P., and Luco, N. (2007). “Probabilistic seismic demand analysis using advanced ground motion intensity measures.” *Earthquake Engineering & Structural Dynamics*, 36(13), 1837–1860.

Trautner, C. A., and Hutchinson, T. C. (2018). “Parametric Finite-Element Modeling for Exposed Steel Moment Frame Column Baseplate Connections Subjected to Lateral Loads.” *Journal of Structural Engineering*, 144(6), 04018049.

Trautner, C. A., Hutchinson, T., Grosser, P. R., and Silva, J. F. (2016). “Effects of Detailing on the Cyclic Behavior of Steel Baseplate Connections Designed to Promote Anchor Yielding.” *Journal of Structural Engineering*, 142(2), 04015117.

Travasarou, T., Bray, J. D., and Abrahamson, N. A. (2003). “Empirical attenuation relationship for Arias Intensity.” *Earthquake Engineering & Structural Dynamics*, 32(7), 1133–1155.

Turkstra, C. J., and Madsen, H. O. (1980). “Load Combinations in Codified Structural Design.” *Journal of the Structural Division*, 106(12), 2527–2543.

Tzimas, A. S., Kamaris, G. S., Karavasilis, T. L., and Galasso, C. (2016). “Collapse risk and residual drift performance of steel buildings using post-tensioned MRFs and viscous dampers in near-fault regions.” *Bulletin of Earthquake Engineering*, 14(6), 1643–1662.

Uang, C.-M., and Bruneau, M. (2018). “State-of-the-Art Review on Seismic Design of Steel Structures.” *Journal of Structural Engineering*, 144(4), 03118002.

Vamvatsikos, D., and Cornell, C. A. (2002). “Incremental dynamic analysis.” *Earthquake Engineering & Structural Dynamics*, 31(3), 491–514.

Vamvatsikos, D., and Cornell, C. A. (2004). “Applied Incremental Dynamic Analysis.” *Earthquake Spectra*, 20(2), 523–553.

Vamvatsikos, D., and Cornell, C. A. (2005). “Developing efficient scalar and vector intensity measures for IDA capacity estimation by incorporating elastic spectral shape information.” *Earthquake Engineering & Structural Dynamics*, 34(13), 1573–1600.

Vamvatsikos, D., and Fragiadakis, M. (2010). “Incremental dynamic analysis for estimating seismic performance sensitivity and uncertainty.” *Earthquake Engineering & Structural Dynamics*, 39(2), 141–163.

Victorsson, V. K. (2011). “The reliability of capacity-designed components in seismic resistant systems.” PhD thesis, Stanford University.

Wald, F. (2000). “Column Base Modelling.” *Semi-Rigid Joints in Structural Steelwork*, Springer Vienna, Vienna, 227–288.

Wald, F., and Jaspart, J.-P. (1998). “Stiffness design of column bases.” *Journal of Constructional Steel Research*, 46(1–3), 245.

Wald, F., Sokol, Z., Steenhuis, M., and Jaspart, J.-P. (2008). “Component method for steel column bases.” *Heron*, 53(1/2), 3–20.

Wang, J., Burton, H. V., and Dai, K. (2019). “Combination Rules Used to Account for Orthogonal Seismic Effects: State-of-the-Art Review.” *Journal of Structural Engineering*, 145(11), 03119001.

Wells, D. L., and Coppersmith, K. J. (1994). “New empirical relationships among magnitude, rupture length, rupture width, rupture area, and surface displacement.” *Bulletin of the Seismological Society of America*, 84(4), 974–1002.

Wilkie, D. (2020). “Advancing probabilistic risk assessment of offshore wind turbines on monopiles.” PhD thesis, University College London.

Yura, J. A., Galambos, T. V., and Ravindra, M. K. (1978). “The Bending Resistance of Steel Beams.” *Journal of the Structural Division*, 104(9), 1355–1370.

Zareian, F., Ibarra, L., and Krawinkler, H. (2004). “Seismic Demands and Capacities of Single-Story and Low-Rise Multi-Story Woodframe Structures.” *Proceeding,* *13th World Conference on Earthquake Engineering*, Canadian Association for Earthquake Engineering, Vancouver.

Zareian, F., and Kanvinde, A. (2013). "Effect of Column-Base Flexibility on the Seismic Response and Safety of Steel Moment-Resisting Frames." *Earthquake Spectra*, 29(4), 1537–1559.

Zeris, C., Vamvatsikos, D., and Giannitsas, P. (2007). "Impact of FE modeling in the seismic performance prediction of existing RC buildings." *Proceeding, ECCOMAS Thematic Conference on Computational Methods in Structural Dynamics and Earthquake Engineering*, European Community on Computational Methods in Applied Sciences, Barcelona.